On Shock Wave Diffraction From Non-orthogonal Apertures

Randall Tyrone Paton

A thesis submitted to the Faculty of Engineering and the Built Environment, University of the Witwatersrand, Johannesburg, in fulfilment of the requirements for the degree of Doctor of Philosophy.

Johannesburg, January 2018

Declaration

I declare that this thesis is my own, unaided work, except where otherwise acknowledged. It is being submitted for the degree of Doctor of Philosophy in the University of the Witwatersrand, Johannesburg. It has not been submitted before for any degree or examination at any other university.

Signed this 17th day of January 2018



Randall Tyrone Paton

For my late parents, Roy and Ebba, and my late grandmother, Pat, who always supported my dreams and with whom I would have loved to have shared this.

Acknowledgements

It takes a village to raise a child and an entire city to get a PhD completed. There are so many people that have contributed to the completion of this thesis but I would specifically like to thank the following people:

First, Professor Beric Skews for a myriad of reasons but not least for being my supervisor, collaborator, and mentor. He has helped me to develop the confidence to pursue my curiosity and taught me that everything in moderation is a key to a long, happy life full of wonder.

This work is based on the research most recently supported in part by the National Research Foundation of South Africa (Unique Grant Number 105689). However, it has been additionally supported in previous years through Prof. Skews' funding of the activities of the Flow Research Unit via the NRF Competitive Programme for Rated Researchers and Incentive funding, as well as research incentive funding provided by the South African Department of Higher Education and Training.

Professor Robert Reid, Head of the School of Mechanical, Industrial, and Aeronautical Engineering, supported my application for the sabbatical leave without which this thesis could not have been completed. Further, the Research Committee of the School provided funding allowing aspects of this work to be presented at several conferences.

Numerous Honours students have been essential for the experimental data gathering for this study. The majority of the data presented for the reflection of conical shock waves were gathered by Sidney Rubidge and Joshua Snow in 2010. The later tests considering specifically the conical Kelvin-Helmholtz instability and jet anomaly were conducted by Russell Hall and Dean van Aswegen respectively in 2013. In 2011, Mohammed Dangor conducted the first experiments on inclined shock wave diffraction which led to the curved exit diffraction study undertaken by Alesha Saligram in 2013. Finally, a last-minute campaign of experiments necessitated by a disastrous hard drive failure was thankfully completed by Alessandro Filippi, Soshe Lewin, and Peter Stathoulis in 2017.

Russell Hall and Alessandro Filippi must also specifically be thanked for their service as acting Flow Research Unit Research Officers as this afforded me time to dedicate to the completion of my thesis.

As with any sufficiently complex research endeavour, a slew of suppliers were essential to the completion of my experiments. Eric Milburn of ECM Technologies and Russell Brown and Tim Nicholls as well as their teams at Photron UK generously kept our high-speed camera functioning and able to provide the needed experimental images to first see the new flow fields studied here. On the computational side, Danie de Kok and Stephan Schmitt of Qfinsoft must specifically be thanked for helping me with testing the limits of CFD to develop the models for various iterations of my study topic. Following them, the final models presented here would not have been possible without Renier Dreyer of CrunchYard or Charles Crosby and the incredible team at the South African Centre for High-Performance Computing (CHPC).

I must especially thank my partner, Neilen, for teaching me this late in my life that happiness is possible and for his firm support in finishing my writing.

I am dearly grateful to my broader family, and especially Christine, Marguerite, and Nicole, for the support and help in so many ways over the long years that it has taken to finish this work.

Finally my brothers, Dylan and Tristan, must be lauded for being the constant anchors of my life and the incredible people that they are. While we are separated by half a world, you are always close to my heart.

Randall T. Paton
17 January 2018

Abstract

The diffraction of shock waves has been explored in many contexts in which either the shock wave is plane and the confining volume has complex geometry or where the shock wave has some non-plane geometry, typically something like spherical since this is the approximate shape of the waves generated by blasts. However, these studies have not considered more complex initial wave shapes or exit geometries. This study therefore addresses this deficiency in two ways.

The dynamic conical shock wave was originally proposed as a mechanism for the initiation of fusion whereby the focusing of the shock wave near the axis of symmetry would produce the high temperatures and pressures required. This was explored numerically and theoretically, as no experimental method was considered viable, and it was found that the regular reflection of a shock wave defined by conical wave geometry is not stable and will revert to an irregular reflection pattern at the axis. Three primary geometries were identified distinguished by the number of irregular reflections formed and influenced by the induced vortical flow. The current study used a developed experimental apparatus to study conical shock waves and an additional, new reflection pattern, named the von Neumann type (vN-type) for the similarity to the von Neumann reflection of weak plane waves, was identified. In addition, instability of the conical shear layer present as a result of the irregular reflection at the axis of the shock wave was identified experimentally which resembles the Kelvin-Helmholtz instability previously only studied in two-dimensional configurations of compressible flow. Dynamic bending of the central jet from the reflection axis was also tested as a function of upstream occlusion in the shock tube and this suggests possible future work in compressible jet actuation.

The current study also considered the diffraction of plane shock waves at the inclined or curved exits of shock tubes, which are more general examples of duct interaction of the sort that might be found in engines or ventilation systems. This was done experimentally using novel, open test sections for a conventional shock tube and for a limited number of computational cases. These flows are characteristically different from the diffraction of shock waves from tubes of complex cross-section studied to date where the exit plane is still

normal to the direction of travel of the wave. This is because the shock wave still undergoes simultaneous diffraction at all points around the edge of the tube in such a case while in this study the wave diffracts at different times around the tube periphery. This affects the strength of both the emerging incident wave and the diffraction and thus an atypical formation of the jet and vortex takes place.

In the case of the inclined plane exit of the shock tube, two primary phenomena were noted: deflection of the jet and change of the jet cone angle; and variations in the vortex diffraction behaviour. For the former effect a large inclination of the exit from the normal increased the spread of the jet and the inclination away from the tube axis. Also, a system of secondary shock waves forms in the jet due to the expansion fans formed at the diffraction edge, typical of underexpanded jets but becomes weaker as exit surface inclination increases. The second effect noted is of the increased curvature as a function of time after diffraction for higher inclinations, due to the much stronger induced velocities for the portion of the vortex shed on the obtuse upstream edge. The vortex loop also loses coherence with increasing inclination because of the weak vortex shedding at the downstream edge of the tube.

The results for the curved exit are similar although the effects are not as extreme since the limiting diffraction angles are lower than for the extreme plane cases due to the characteristics of circular geometry. In the extreme case of part of the shock tube exit being tangent to the exit surface, the vortex again does not form a closed loop but rather terminates in the exit surface. This was particularly tested here with a plane section at the tangent point. However, the secondary reflection of the diffracted shock wave due to the curvature of the surface toward the diffracted wave, which tends to disrupt the vortex, means that an internal diffraction with a fully closed tube would result in a short-lived vortex loop.

In both of the latter cases the vortex loop, or arch if it cannot close into a loop, is part of the physical mechanism whereby a jet flow exiting a pipe adjusts to being a diffuse flow along the exit surface. This is accomplished by the spreading of the sheet of vorticity, which is the boundary layer in the pipe and the jet boundary outside of it, by the origination of turbulence in the breakdown of the vortex arch or loop.

The diffraction of shock waves from non-orthogonal apertures demonstrates features previously unidentified and suggests complex flow patterns which simplified two-dimensional analysis cannot describe.

Contribution

There are three fundamental contributions of this particular thesis. The first two pertain to the dynamics of reflecting conical shock waves and the latter, and more substantial, to diffraction of shock waves from non-orthogonal apertures.

The first contribution is the identification of a fourth reflection pattern, named the vN-type, of collapsing conical shock waves. This configuration is named for the similarity to von Neumann reflection of plane waves since the reflected wave cannot be clearly discerned and the Mach disc and incident wave form an apparently continuous surface.

The second contribution is the experimental identification of an instability of the conical shear layer, produced by the reflection at the axis of collapsing conical shock waves, which has been called the conical Kelvin-Helmholtz instability due to the resemblance to that canonical feature. While this will still require computational verification and exploration of the parameter space, this is the first evidence of the axisymmetric analogue of a phenomenon originally described and only tested to date as a two-dimensional instability of the shear layer in compressible flows.

The third contribution is the identification of the formation of a vortex arch when a shock wave emerges from an aperture for which some portion of the aperture is tangent or at a low angle to the inner surface of the shock tube. While the formation of vortex loops, even at low incident shock wave Mach numbers, is consistent for orthogonal exit apertures, the vortex line cannot close for shallow or tangent exit apertures and instead terminates in the exit surface, forming a vortex arch. As the vortex arch propagates it widens due to dilatation stress and loses coherence. The overall effect of this degradation of the vortex arch is a mechanism by which a free jet flow is transformed into a diffused surface flow when a jet emerges adjacent or at a low angle to a surface.

Published Work

Aspects of this thesis have been published in the following references:

Paton, R. T. and B. W. Skews (2015). 'Shock wave diffraction at the inclined exit of a shock tube'. In: *29th International Symposium on Shock Waves*. Ed. by R. Bonazza and D. Ranjan. Madison, WI, USA, pp. 1279–1284. ISBN: 978-3-319-16834-0.

Paton, R. T. and B. W. Skews (2017). 'Imaging of the Conical Kelvin-Helmholtz Instability'. In: *30th International Symposium on Shock Waves 1*. Ed. by G. Ben-Dor, O. Sadot and O. Igra. Tel Aviv, Israel: Springer International Publishing, pp. 269–273. ISBN: 978-3-319-46211-0. DOI: 10.1007/978-3-319-46213-4_44.

Paton, R. T., B. W. Skews and M. Dangor (2012). 'Vortex dynamics at an oblique shock tube exit'. In: *Proceedings of the 30th International Congress on High-Speed Imaging and Photonics (ICHSIP30)*. Ed. by R. T. Paton and B. W. Skews. Pretoria, South Africa, pp. 281–286. ISBN: 9780620562133.

Paton, R. T., B. W. Skews and A. Saligram (2014). 'The diffraction of a plane shock wave from the curved exit of a shock tube'. In: *16th International Symposium on Flow Visualization*. Ed. by S. Someya. Okinawa, Japan, pp. 1–6. ISBN: 978-4-906497-85-0.

Paton, R. T., B. W. Skews and A. Saligram (2015). 'Visualisation of plane shock wave diffraction from the curved exit of a shock tube'. In: *Journal of Visualization* 18.3, pp. 493–499. ISSN: 1343-8875. DOI: 10.1007/s12650-014-0265-7.

Paton, R. T. et al. (2012a). 'Imploding conical shock waves'. In: *Shock Waves* 23.4, pp. 317–324. ISSN: 0938-1287. DOI: 10.1007/s00193-012-0386-7.

Paton, R. T. et al. (2012b). 'Imploding conical shock waves'. In: *28th International Symposium on Shock Waves*. Ed. by K. Kontis. Vol. July. Manchester, United Kingdom, pp. 959–964. ISBN: 978-3-642-25687-5.

Rubidge, S. et al. (2015). 'Kelvin-Helmholtz instability on the Mach reflection shear layer'. In: *29th International Symposium on Shock Waves*. Ed. by R. Bonazza and D. Ranjan. Madison, WI, USA, pp. 1579–1584. ISBN: 978-3-319-16834-0.

Contents

Declaration i

Acknowledgements iii

Abstract v

Contribution vii

Published Work viii

Contents ix

List of Figures xiv

List of Tables xviii

List of Acronyms xix

List of Symbols xx

1 Introduction 1

2 Literature Survey 2

2.1 Vortex Terminology 2

2.1.1 Vortices and rotation . . . 2
2.1.2 Vorticity and circulation . . . 3
2.1.3 Vortex filaments . . . 4
2.1.4 Vortex rings . . . 5
2.2 Experimental Studies . . . 6
2.2.1 Incompressible vortex flows . . . 7
2.2.2 Compressible flow fields . . . 8
2.2.2.1 Fundamentals of shock wave diffraction and reflection . . . 8
2.2.2.1.1 Shock wave diffraction . . . 8
2.2.2.1.2 Shock wave reflection . . . 11
2.2.2.2 Shock wave-induced vortex flows . . . 13
2.3 Numerical Studies . . . 20
2.3.1 Analytical treatments . . . 20
2.3.2 Empirical treatments . . . 23
2.3.3 Computational Fluid Dynamics . . . 24
2.3.4 Conical shock wave interactions . . . 26
2.3.4.1 Steady conical flows . . . 26
2.3.4.2 Cylindrical shock wave dynamics . . . 28
2.3.4.3 Conical shock wave dynamics . . . 30
2.4 Conclusion . . . 34

3 Objectives **35**

4 Apparatus **36**

4.1 Overview . . . 36

4.2 Experimental Apparatus . . . 36

4.2.1 Flow at the oblique exit of a shock tube . . . 36

4.2.2 Flow produced by a conical shock wave . . . 39

4.3 Flow Visualisation . . . 42

5 Results **43**

5.1 Flow Produced by a Conical Shock Wave . . . 43

5.1.1 Estimation of apex Mach number . . . 43

5.1.2 Reflection behaviour . . . 43

5.1.3 Computational Fluid Dynamics . . . 47

5.1.3.1 Effect of driver pressure . . . 48

5.1.3.2 Effect of cone angle . . . 49

5.1.4 Other flow features . . . 53

5.1.4.1 Conical Kelvin-Helmholtz instability . . . 53

5.1.4.2 Curved jetting . . . 58

5.1.5 Summary . . . 59

5.2 Flow Produced by Diffraction of a Plane Shock Wave at the Inclined Exit of a Shock Tube . . . 61

5.2.1 Experimental results . . . 61

5.2.1.1 The general nature of the diffraction . . . 61

5.2.1.2 Flow field development . . . 63

5.2.1.3 Effect of exit plane angle . . . 66

5.2.1.4 Extreme exit plane angle . . . 70

5.2.1.4.1 Upstream flow field . . . 71
5.2.1.4.2 Downstream flow field . . . 72
5.2.2 Computational Fluid Dynamics . . . 75
5.2.2.1 Model parameters . . . 75
5.2.2.2 Results . . . 77
5.2.2.3 Model validation . . . 78
5.2.2.3.1 Upstream flow field . . . 78
5.2.2.3.2 Downstream flow field . . . 82
5.2.2.4 Further results . . . 84
5.2.3 Summary . . . 88
5.3 Flow Produced by Diffraction of a Plane Shock Wave at the Curved Exit of a Shock Tube . . . 90
5.3.1 Experimental results . . . 90
5.3.1.1 Tangent exit . . . 96
5.3.2 Computational Fluid Dynamics . . . 98
5.3.2.1 Model validation . . . 99
5.3.2.2 Further results . . . 103
5.3.3 Summary . . . 109
6 Conclusion **111**
Bibliography **113**
Glossary **118**

A Specification of equipment and instrumentation used in schlieren visualisation system **119**

B Videos **123**

B.1 Flow Produced by a Conical Shock Wave 124

B.2 Flow Produced by Diffraction of a Plane Shock Wave at the Inclined Exit of a Shock Tube 125

B.3 Flow Produced by Diffraction of a Plane Shock Wave at the Curved Exit of a Shock Tube 126

List of Figures

2.1 Schematic of a vortex ring indicating principal parameters 6

2.2 Side view and schematic of motion of vortex loop formed from a lenticular orifice 8

2.3 Schematic of the perturbed flow behind a diffracted shock wave 9

2.4 Vortex formed by the diffraction of a Mach 1.65 vortex from a v-shaped edge 10

2.5 Schematic of regular shock wave reflection and direct Mach reflection 12

2.6 Kelvin-Helmholtz instability of the shear layer of a direct Mach reflection . . 13

2.7 Schlieren images of vortex development at the end of an open shock tube . . 14

2.8 Development of the embedded, rearward-facing shock wave in a vortex ring . 15

2.9 Development of the induced secondary vortex ring 16

2.10 Laser sheet visualisation of multiple counter-rotating vortex rings 16

2.11 Shock wave-vortex interaction flow field for a sudden area change 17

2.12 Flow field at the exit of a 0.4 aspect ratio elliptical nozzle 18

2.13 General representations of the dynamics of elliptical and square vortex loops 19

2.14 Singular lenticular orifice and resulting flow field 20

2.15 Non-dimensionalised growth of the vortex streamline 21

2.16 Calculated deformation of trilobal vortex loop 22

2.17 Propagation of elliptical vortex loops 24

2.18 Isosurfaces of enstrophy for interacting swirling vortex rings 25

2.19 Diffraction of a plane shock wave at the inclined plane exit of a shock tube . 27

2.20 Experimental images showing convergence of a weak cylindrical shock wave and reflections forming on a stronger cylindrical shock wave 29

2.21 Apparatus and holographic interferograms of instabilities of converging cylindrical shock waves 30

2.22 Reflection of a conical shock wave generated by a toroidal ring wedge 31

2.23 Pseudoschlieren images of the types of conical shock wave reflection patterns 32

2.24 Comparison of numerical and experimental results showing DV-type reflection 33

4.1 General arrangement of conventional shock tube used for oblique exit study . 37

4.2 Plane exit test section inclined 75° to shock normal 37

4.3 Radius ratio 3 model with tangent exit 38

4.4 Radius ratio 5 model with shock tube centreline offset of D_{ST} 38

4.5 Radius ratio 3 model with shock tube centreline offset of 0.5 D_{ST} 39

4.6 General arrangement of conical shock tube 40

4.7 Detailed view of wave shaping and test sections of conical shock tube showing general change of wave shape 40

4.8 Schematic of the upper and lower occlusion plates 41

5.1 Evolution of the flow from a conical gap with M_{Apex} of 1.11 and a 60° cone half-angle 45

5.2 Evolution of the flow from a conical gap with M_{Apex} of 2.30 and a 60° cone half-angle 46

5.3 CFD geometry and mesh for conical shock tube model 47

5.4 Velocity magnitude contours for M_{Apex} of 1.11 and 60° cone half-angle 49

5.5 Velocity magnitude contours for M_{Apex} of 2.30 and 60° cone half-angle 50

5.6 Velocity magnitude contours for M_{Apex} of 2.30 and 20° cone half-angle 51

5.7 Velocity magnitude contours for M_{Apex} of 2.30 and 30° cone half-angle 52

5.8 Possible Kelvin-Helmholtz instability of the primary shear layer for 60° cone at M_{Apex} of 1.11 54

5.9 Shadowgraphs of the flow field for M_{Apex} of 1.11, 1.37, and 1.76 55

5.10 Detailed view of the development of the Kelvin-Helmholtz instability along the tangent edge of the shear layer and comparison of the developed instability to the plane wedge case 57

5.11 The deflection of the central jet for M_{Apex} of 1.76 with the 30° lower and 60° upper occlusion 59

5.12 The flow field development for the exit of a shock tube inclined 30° to the normal for Mach numbers of 1.26, 1.47, and 1.66 62

5.13 Annotated experimental images for the early and later flow field development 63

5.14 The flow field development for the exit of a shock tube inclined 45° to the normal for Mach numbers of 1.28, 1.49, and 1.66 68

5.15 The flow field development for the exit of a shock tube inclined 60° to the normal for Mach numbers of 1.28, 1.49, and 1.67 69

5.16 The flow field development for the exit of a shock tube inclined 75° to the normal for Mach numbers of 1.27, 1.48, and 1.67 72

5.17 The flow field development for the exit of a shock tube inclined 75° to the normal for Mach numbers of 1.27, 1.49, and 1.67 74

5.18 CFD geometry and mesh for inclined plane exit model 76

5.19 Comparison of experimental and numerical results at the upstream position for Mach 1.25 79

5.20 Comparison of experimental and numerical results at the upstream position for Mach 1.4 80

5.21 Comparison of experimental and numerical results at the upstream position for Mach 1.6 81

5.22 Comparison of experimental and numerical results at the downstream position for Mach 1.4 82

5.23 Comparison of experimental and numerical results at the downstream position for Mach 1.6 83

5.24 The computational vortex development for the exit of a shock tube with an exit surface angle of 75° for Mach numbers of 1.25 and 1.4 85

5.25 The computational vortex development for the exit of a shock tube with an exit surface angle of 75° for Mach numbers of 1.6 and 2.2 87

5.26 The flow field development for the exit of a shock tube with an exit radius ratio of 5 for Mach numbers of 1.26, 1.42, and 1.66 91

5.27 Annotated experimental images for the early and later flow field development 92

5.28 The flow field development for the exit of a shock tube with an exit radius ratio of 3 for Mach numbers of 1.25, 1.49, and 1.67 95

5.29 The flow field development for the exit of a shock tube with an exit radius ratio of 3 and tangent exit surface for Mach numbers of 1.21, 1.49, and 1.67 . 97

5.30 CFD geometry and mesh for curved exit surface model 99

5.31 Comparison of experimental and numerical results for Mach 1.25 100

5.32 Comparison of experimental and numerical results for Mach 1.4 101

5.33 Comparison of experimental and numerical results for Mach 1.6 103

5.34 The computational vortex development for the exit of a shock tube with an exit radius ratio of 3 and tangent exit surface for Mach numbers of 1.25 and 1.4 104

5.35 The computational vortex development for the exit of a shock tube with an exit radius ratio of 3 and tangent exit surface for Mach numbers of 1.6 and 2.2 107

5.36 The computational symmetry plane pressure development for the exit of a shock tube with an exit radius ratio of 3 and tangent exit surface for Mach 2.2 108

List of Tables

A.1 Specification of apparatus and instrumentation for shock diffraction from the oblique exit of a shock tube 119

A.2 Specification of apparatus and instrumentation for conical shock wave reflection 121

B.1 Videos of Conical Shock Wave Diffraction Experiments 124

B.2 Videos of Inclined Shock Tube Exit Shock Wave Diffraction Experiments for Exit Plane Angles of 30°, 45°, and 60° 125

B.3 Videos of Inclined Shock Tube Exit Shock Wave Diffraction Experiments and CFD for 45° Exit Plane Angle 125

B.4 Videos of Curved Shock Tube Exit Shock Wave Diffraction Experiments for Radius Ratios of 3 and 5 126

B.5 Videos of Curved Shock Tube Exit Shock Wave Diffraction Experiments and CFD for a Radius Ratio of 3 with a Tangent Exit Plane 126

List of Acronyms

CFD computational fluid dynamics.

CRVL counter-rotating vortex line.

CRVR counter-rotating vortex ring.

DDT Deflagration-to-detonation transition.

fps frames per second.

KHI Kelvin-Helmholtz instability.

LIA localised induction approximation.

PIV particle imaging velocimetry.

RANS Reynolds-averaged Navier-Stokes.

List of Symbols

The units of quantities defined by a symbol are indicated in square brackets following the description of the symbol. Quantities with no indicated units may be assumed to be dimensionless.

D Vortex ring diameter [m, mm].

u Vortex ring convection speed [ms^{-1}].

$*_{\mathbf{Apex}}$ Property related to the apex of a conical contraction, typically related to the incident ($*_{\mathrm{I}}$) plane shock wave Mach number.

$*_{\mathbf{E}}$ Property related to the exit region of a shock tube.

$*_{\mathbf{I}}$ Property related to an incident shock wave, used to calculate the apex ($*_{\mathrm{Apex}}$) shock wave Mach number for a conical contraction.

$*_{\mathbf{ST}}$ Property related to the shock tube.

$\mathbf{u}$ Velocity vector [ms^{-1}].

α Inclination of the exit surface normal to the plane shock wave normal [°].

α_ϕ Local inclination of the exit surface normal to the plane shock wave normal as a function of azimuth position [°].

δ Vortex core diameter [m, mm].

Γ Scalar vorticity of vortex filament [s^{-1}].

λ_2 Eigenvalue of the velocity gradient tensor.

$\boldsymbol{\omega}$ General vorticity [s^{-1}].

ϕ Angular position of point on cylindrical surface relative to horizontal symmetry plane [°].

r Radial distance from vortex filament [m, mm].

RR Ratio of the shock tube ($*_{ST}$) internal radius to the radius of the exit surface ($*_{E}$) for a curved shock tube exit surface.

v Induced velocity scalar [ms^{-1}].

Chapter 1 Introduction

The behaviour of compressible vortices and vortices produced by impulsive means in compressible flows have been the subject of study for some time. A major constraint of these studies is that they have, in general, considered only vortices in which the core plane is normal to the local flow direction as would be the case of vortices formed from a jet normally intersecting a plane. However, it is clear from observation of everyday installations such as air conditioning systems, or more specialised ones such as jet propulsion systems, that the case of ducts (which carry or produce jets) terminating in a plane normal to the duct axis are the exception rather than the rule. Stated otherwise, ducts will more commonly intersect each other in surfaces, curved or plane, that are inclined to the axis of one or both ducts. While air conditioning systems would not contain shock waves or supersonic flow under normal operating conditions, there is the unfortunate possibility of the introduction of these features by explosions, malicious or accidental, in buildings. Should the ducting system in question carry combustible gases, such as the case of gas pipelines, there is the risk of Deflagration-to-detonation transition (DDT) in these pipes. There is thus a need to explore the dynamics of these systems and to compare the behaviour of the vortices in these systems to the canonical case of the normal vortex ring.

Chapter 2 Literature Survey

Since this thesis deals with the flow fields produced by shock waves, familiarity with the basic definition and behaviour of shock waves is assumed. However, since the behaviour of the vortices produced by the diffraction of shock waves are fundamental drivers of the behaviour to be studied, particular attention is paid here to vortices produced by various methods and the analysis and modelling thereof. As such, some of the material presented is to ensure a complete basic understanding. Furthermore, much of the presented material represents the majority of studies made of the behaviour of these vortices and particularly the way in which vortices have either been studied with complex geometry in incompressible flow fields or simple geometry in compressible flow fields but rarely, if at all, with complex geometry in compressible flow fields. Therefore little direct analogy can be drawn between the results of the experiments undertaken for this study and the studies presented here, though this is done wherever possible.

2.1 Vortex Terminology

Before any study of vortex behaviour can be undertaken, a set of standard terms describing the geometry of the vortex must be defined.

2.1.1 Vortices and rotation

As stated in Green (1995), the term 'vortex' is one which has no single accepted definition other than that a vortex is that feature of a flow field which is readily identified by practitioners as being a vortex. This is because there are several considerations for systems which may be considered vortices and rotation of fluid elements is not an exclusive definition. As shown in Green, the flow inside of a boundary layer may be rotational but would not be considered a vortex while the fluid in a forced vortex may be irrotational. Logically, a rotational flow is one in which a fluid element rotates about its centre as a result of the body forces exerted on

it. For the purposes of this work, a vortex will be taken to mean a region in a flow field which exhibits rotation of the fluid around a point or line in space. Additionally, a boundary layer flow will be called a 'vortex sheet' as this concept is of use when considering the formation of a vortex at the outlet of a shock tube or other orifice where the boundary layer following the shock will emerge from the orifice.

2.1.2 Vorticity and circulation

Two important and related concepts when describing vortices in a flow field are vorticity and circulation. Vorticity is mathematically defined as the curl of the velocity field and represents the rate of rotation of a fluid element about its own axes (Green 1995). This result is generally stated as:

$$\boldsymbol{\omega} = \boldsymbol{\nabla} \times \mathbf{u} \tag{2.1}$$

Circulation is the integral of the vorticity in a direction orthogonal to the plane in which the integration is made. Effectively, circulation is a measure of the total amount of rotation in the fluid as a function both of the volume of fluid affected and the degree to which it is affected. The circulation can thus also be expressed as the integral of the velocity field within a closed contour.

$$\Gamma \equiv \oint_C \mathbf{u}.d\boldsymbol{\ell} \tag{2.2}$$

$$\Gamma \equiv \int_S \boldsymbol{\omega} \cdot \mathbf{n} dS \tag{2.3}$$

In the case of the solid body rotation of a fluid, also known as the forced vortex, the value of vorticity will describe the flow at all points in the flow field and can be used a measure of the strength of the rotation of the fluid mass. Specifically, it can be shown that the vorticity is twice the angular velocity of the rotating body of fluid about its axis of rotation. If the body of rotating fluid is infinite, then the circulation will itself be infinite and this represents the primary constraint on this sort of model for a vortex.

By contrast, in the case of the hypothetical flow of the sort seen near a drain in a large body of water (but in which the 'drain' is small compared to the body of fluid), also known as the free vortex, the vorticity will be zero everywhere in the field and infinite at the centre of rotation. The velocity of the fluid around the centre of rotation decreases to zero at an infinite distance from the centre. In this case, the fluid elements entrained in the vortex are said to be irrotational. Here the circulation is finite but the requirement of infinite fluid vorticity at the centre again makes this an invalid model for real vortex behaviour.

The first realistic representation of the real vortex was the Rankine vortex, which is essentially a combination of the forced and free vortices (Rankine 1872). The forced vortex properties

are used to model the core of the real vortex with the low velocity centre and increase in velocity to a certain radius from the centre of rotation, called the transition radius. From the transition radius outward the free vortex model is applied with the characteristic decrease in velocity toward infinity.

2.1.3 Vortex filaments

In considering a vortex in free space, a concept typically used to describe the shape of the vortex is the vortex line or filament. Mathematically, the vortex filament is the line that is tangent at all points to the vorticity vector at any cross-section of the vortex described. Use of the vortex filament allows for simple graphical representation of three-dimensional vortices and facilitates mathematical treatment of these.

One important consideration to arise from the definition of the vortex filament is that the circulation along a vortex filament is constant, although the vorticity of sections of the vortex may differ (Helmholtz 1867). These differences may result from curvature of the vortex, stretching or compression of the vortex along its axis, or dilatation of the vortex. Another implication of the observation of constant circulation along a vortex filament is that these cannot terminate in a fluid as the circulation, and hence momentum, would not be conserved. They must, therefore, terminate at a solid boundary or fluid-fluid interface (of significant change in viscosity), or form loops entirely within the fluid for real flows in which vortex filaments of infinite length are impossible.

Vortex filaments are often used to represent the slender vortex, one in which the diameter of the vortex core is small compared to the length or ring diameter of the vortex for vortex lines or vortex rings respectively. This concept is of use in the development of analytical tools for describing the behaviour of line vortices as the dynamics of the vortex and surrounding fluid can be calculated using the Biot-Savart law instead of calculating the dynamics of bulk volumes of fluid undergoing vortical motion.

$$v = \frac{\Gamma}{2\pi r} \tag{2.4}$$

where:

- v is the local velocity tangent to the radial vector (i.e. in the normal direction),
- Γ is the circulation of the vortex filament and,
- r is the radial distance form the vortex filament to the point under consideration

Originally developed for the analysis of magnetic fields as a result of electrical currents, the Biot-Savart law can be used to calculate the velocity induced by a vortex (represented by a vortex filament) through the following relationship. While the formulation in Equation 2.4 is specifically for two-dimensional flow fields, it can be used in conjunction with the notion of the

slender vortex to formulate the localised induction approximation (LIA) since the spanwise effects of of flow induction are assumed to be small compared to those in the plane normal to the vortex core.

The most significant implication of the Biot-Savart law when considering vortex propagation is that the velocity induced increases linearly with the circulation of the vortex filament. The induced velocity field causes the convection of a vortex line in space and so, the stronger the induced velocity, the faster the filament will convect. The implication of this statement for vortices where the strength varies along the length of the vortex line is that the vortex line will deform with time as some portion convect faster from some initial position than others.

2.1.4 Vortex rings

The final fundamental concept of importance in considering vortex dynamics as presented in this work is the vortex ring, or more generally the vortex loop. This is a phenomenon in which the vortex closes upon itself and does not terminate in a boundary such as a wall or dense fluid interface. The most common examples of the vortex ring are the smoke rings blown by some tobacco smokers, the plume of a large explosion (such as the iconic images of the results of the nuclear weapons deployed at Hiroshima and Nagasaki in WWII), or the outflows of the 'vortex cannons' popularised by viral YouTube videos.

There are three basic parameters used to define the behaviour of a vortex ring: the core diameter (δ), ring diameter (D) and the convection speed (u). As the name suggests, the core diameter of a vortex ring is the diameter of the cross section of the region of vorticity itself. The ring diameter is typically defined as the diameter of the vortex filament passing through the centre of the vortex core, although some works alternatively define this as the diameter of the central flow region 'outside' of the vortex core. The convection speed of the vortex is the speed at which the vortex ring moves along the axis orthogonal to the plane defined by the centreline of the core. As vortex loops are often formed by the sudden ejection of material from an orifice and they may not necessary be plane, the convection speed is sometimes defined relative to the direction of the fluid flow used to generate the vortex loop.

A geometric property of note when considering vortex loops is the profile of the vortex core. In detailed considerations of vortex dynamics this may be taken to mean the velocity profile across the section of the vortex. However, when describing general vortex loops, this is more commonly used to describe the shape that the curve of the axis of the vortex core (or possibly the vortex filament representing the vortex loop) most resembles. In the case of the classical vortex ring, this is a circle. However, in the decay of vortex rings to turbulence this shape often changes and the shape of the axis profile may be described as wavy i.e. a circular

line with superimposed waves along it. Another common axis profile is elliptical, as this is often produced by distortion of a circular vortex ring. In general, descriptions of vortex core profiles are used to more fully describe the changes in shape of vortex rings, although non-circular vortex loops may be generated initially as well. For the purposes of this work the term vortex ring will be applied exclusively to vortex loops with circular core profiles while the term vortex loop will be used to describe any vortex line which closes upon itself.

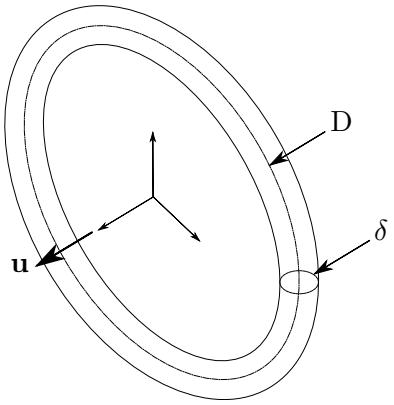


Figure 2.1: Schematic of a vortex ring indicating principal parameters

Related to the concepts of vortex ring diameter and core diameter is the definition of the slender vortex ring. This is one in which the ratio of the vortex core diameter to the ring diameter is low, typically significantly less than one. This definition is made to allow for the use of the simpler analytical models for describing the behaviour of these vortices. Although early analytical treatments of vortices using potential theory had been made, such as the classic Hill's spherical vortex (Hill 1894), these models became intractable for most practical situations and so the definition of the slender vortex is favoured in most analysis, as the simpler mathematics of the vortex filament allows general vortex loops to be modelled, though often the solution of these models require computational methods.

2.2 Experimental Studies

Although this study principally considers vortex loops in impulsively-induced flow fields, some consideration of other studies of incompressible vortex dynamics is relevant to develop understanding of the behaviour of vortices with non-uniform curvature, both in isolation and interacting with one another.

2.2.1 Incompressible vortex flows

Possibly the earliest experimental study of vortex ring behaviour was that by Reynolds (1883). His pioneering work in the nature of turbulence meant that the study undertaken could characterise the behaviour of these rings more rigidly in terms of experimental conditions though it would be some time before this would become the norm.

As visualisation was considerably easier and yielded finer detail in water many of these studies examined the low Reynolds number vortices produced by submerged water jets. The detailed analytical study by Didden (1979) used complementary dye flow and laser Doppler velocimetry experiments to map the parameters of vortices formed at the exit of a short tube when fluid is forced from it by a rapidly actuated piston. Didden's work explored the changes in vortex diameter, core size (considered as the vortex spiral diameter), and position from the outlet as functions of distance and time. In addition, consideration was given to the changes in vorticity and circulation with the development of the vortex and these parameters were characterised in a non-dimensional time frame, making this one of the most detailed studies of vortex behaviour to date.

While most studies had focused on the behaviour of circular vortex rings, the instabilities observed by Didden and others had prompted studies into the behaviour of non-circular vortex loops. The study by Kambe and Takao (1971) had observed the behaviour of non-circular vortex loops produced in air. Since few studies at the time had been aimed toward experimentally studying the factors causing the transition of vortex rings to turbulence, they took the approach of producing vortex loops with profiles which were modal perturbations of the circular vortex profile. Observations were then made of the development of these vortices to compare such behaviour with the wavy profiles previously observed.

It was found that unlike the wavy profiles previously observed, the non-circular vortex loops were prone to curving in the direction of travel as a result of local self-induced velocities and some periodicity of this behaviour was noted. An example of the behaviour of the vortex loop formed from a lenticular orifice in side profile can be seen in Figure 2.2.

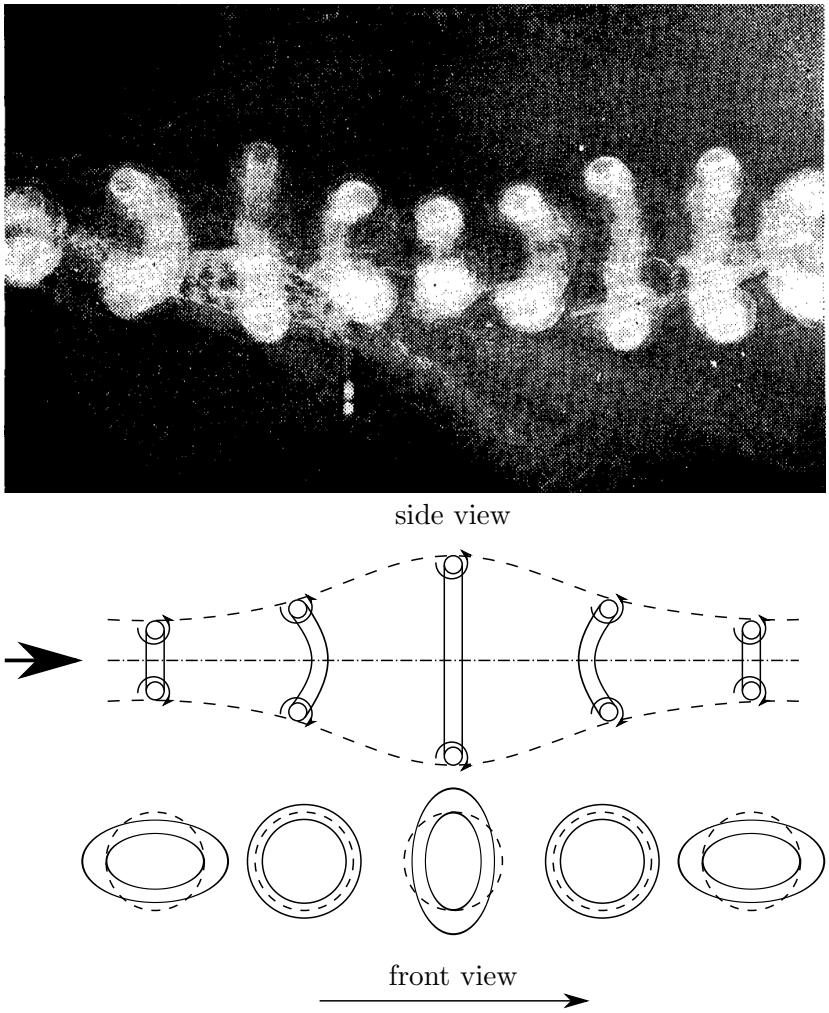


Figure 2.2: Side view (*top*) and schematic (*bottom*) of motion of vortex loop formed from a lenticular orifice (Kambe and Takao 1971)

2.2.2 Compressible flow fields

2.2.2.1 Fundamentals of shock wave diffraction and reflection

2.2.2.1.1 Shock wave diffraction

Much of the work done examining the behaviour of vortex rings was conducted using incompressible media such as water. However, it had been noted that these phenomena occurred in systems of compressible fluids as well and that the vortex loops themselves may be subject to compressibility. Thus, before considering the work done on the formation of shock wave-induced vortices, a discussion of some fundamentals of shock wave diffraction and reflection is pertinent to allow for proper interpretation of results.

The fundamental works on the two-dimensional diffraction of shock waves around corners were those of Skews (Skews (1967b) and Skews (1967a)). These two papers considered the shape of a diffracting two-dimensional shock wave and the perturbed region behind the diffracted wave respectively. The most important feature identified in the former for consideration here is the centred expansion fan which forms at a singular diffraction edge when a shock wave diffracts over it. This expansion fan is the mechanism by which the shape of the shock wave is changed to keep the shock wave perpendicular to the surface after the corner. The further effect of this expansion wave is to accelerate the flow around the corner to match the post-shock flow speed.

In consideration of the formation of shock-induced vortices it is the latter paper which is of greater importance. Referring to the schematic in Figure 2.3, several important features should be noted. First, the curved section of the shock wave wave delimited by the reflected sound wave and the downstream surface of the corner is the region affected by the expansion wave described in Skews (1967b). In the two-dimensional flow field considered here, this expansion wave affects the entire length of the shock wave in the spanwise direction of the edge evenly.

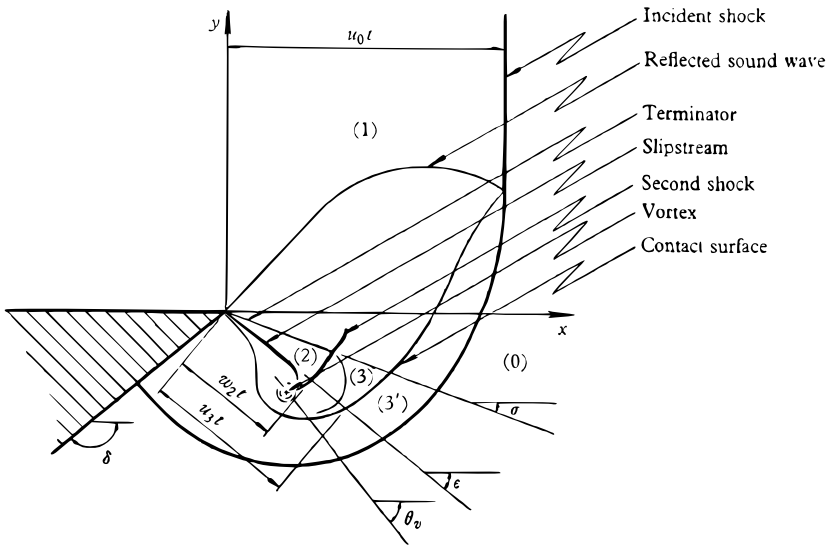


Figure 2.3: Schematic of the perturbed flow behind a diffracted shock wave (Skews 1967a)

However, in three-dimensional flow fields, the expansion wave will affect portions of the wave that are undiffracted through the propagation of the reflected sound wave along the shock surface. Thus, if a portion of a plane shock wave diffracts around a corner, a region along the surface of the shock wave away from the corner will grow with time that is affected by the corner and thus may no longer be plane. Stated differently, a plane shock wave that diffracts simultaneously around a corner of equal angle will display the same post-shock features at all positions along its length. But for a plane shock wave where the diffraction happens at

difference times around the corner or that the properties of the corner differs with position, the effect of different times or types of diffraction at some position will affect the shock wave shape and thus the diffraction behaviour at other positions.

The more significant feature here is the vortex shed from the diffracting edge. Skews defines both a vortex angle, θ_v, and a vortex velocity, q_v, for the propagation of the vortex away from the diffracting edge for a range of incident shock wave Mach numbers from 1.5 to 5.0 and for diffracting corner angles from 15° to 165°, measured from the upstream corner surface. The vortex velocity is weakly dependent on the corner angle until 90°, at which point it becomes independent. Since the vortex velocity is related to the vortex circulation by the Biot-Savart law as discussed in § 2.1.3, this means that the strength of the vortex generated for diffractions greater than 90° is fixed.

The second important point is that no vortex was shed for the diffraction angle of 15°. The reason for this is that the baroclinicity (i.e. the inclination of the vectors of the pressure and density gradients to one another) of the flow at the corner is too low at such angles for the boundary layer emanating from the diffracting edge to roll up into a vortex and the flow instead smoothly turns around the corner.

For cases where the diffraction angle varies along the diffraction edge, these two limits mean that vortices shed at high corner angles greater than 90° will all be of comparable strength at a given time in their development while vortices produced at positions with lower corner angles will be weaker. There is also the possibility that no vortex is shed locally if the diffracting angle at some position is too shallow (nominally 15° or less).

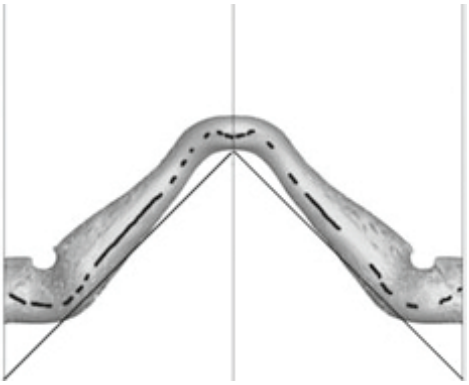


Figure 2.4: Vortex formed by the diffraction of a Mach 1.65 vortex from a v-shaped edge (Skews and Reeves 2012)

One such case in which the diffraction of a plane shock wave over a corner was not simultaneous is that by Skews and Reeves (2012). In this study, the shock wave diffracted over the edges of wedges of constant diffraction angle but for which the profile in the direction of travel

of the shock wave allowed that the shock wave diffracted over some sections of the wedge earlier than at others. This was particularly achieved by making parabolic and v-shaped profiles such that the points of each were the last position at which the shock wave would diffract.

An important feature to note in Figure 2.4, for example, is the thickening of the vortex tube near the apex of the v-shaped diffraction edge. This is a region in which the vortex core, shown as the dashed black line, has high curvature (initially infinite if it conformed to the diffracting edge profile). This effect was shown to occur for regions where the vortex core was highly curved for other geometries as well. One example of this is the study by Cooppan and Skews (2015) considering the diffraction of plane shock waves over discontinuous edges.

2.2.2.1.2 Shock wave reflection

The diffraction of a shock wave is the mechanism by which large-scale vortices are formed in compressible flow fields. However, the reflection of shock waves is an important consideration in the development of these flow fields as the interaction of reflection features with the initial post-shock flow can change the behaviour of the diffraction features significantly.

Shock wave reflection will occur when there is an inclination of a shock wave to a reflecting surface. This is because the shock wave will induce a flow either away from or toward the surface and this would violate the continuity of mass if not corrected there. Given the means by which shock waves typically arise (supersonic flow past a body or the supersonic motion of a body relative to the air), the simplest form of shock wave reflection will be regular reflection as shown in Figure 2.5.

This configuration can occur as either a stationary wave or represent the pseudo-steady flow field for an unsteady flow (i.e. moving shock wave). The incident wave (I) meets the solid surface at an angle and the incoming flow is deflected away from the surface. In order that mass continuity at the surface be maintained, the reflected wave (R) arises to deflect the flow back parallel to the surface.

If the angle of the incident shock wave to the surface is very shallow, it may exceed the limit for which no reflected wave can be formed to deflect the shocked flow back because it is too steeply inclined to the surface. This is a function of the strength of the incident shock wave and inclination to the surface. In such cases the reflection point shifts away from the surface and an irregular reflection, commonly referred to as Mach reflection, forms. The defining characteristic of Mach reflection is the normal shock wave connecting the surface and the incident and reflected waves, referred to as a Mach stem (M). The point at which these three waves meet is referred to as the triple point. The Mach stem means that there is no

deflection of the flow near the surface though there are still the typical changes in pressure, density, temperature, and velocity associated with shock waves.

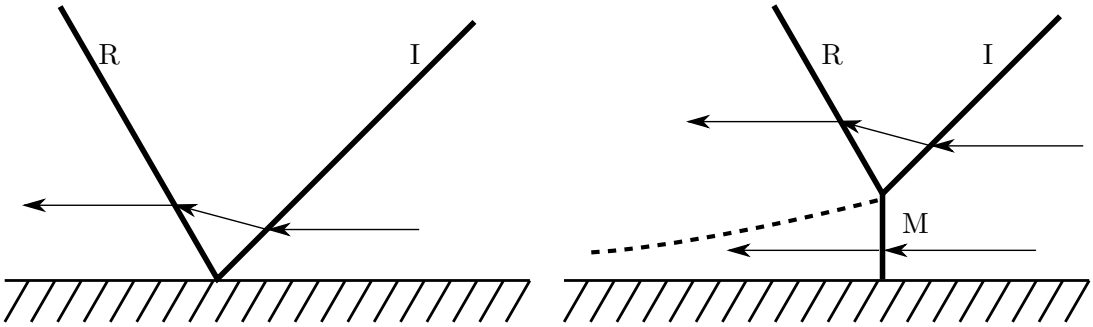


Figure 2.5: Schematic of regular shock wave reflection (*left*) and direct Mach reflection (*right*)

As a result of the different conditions to which flow entering the incident shock wave and Mach stem are subjected, there is a difference in the temperature, density, and velocity of the flow exiting the Mach stem and reflected shock wave. This results in the formation of a shear layer separating the two regions. In unsteady shock wave flows this shear layer is typically inclined towards the reflecting surface, referred to as direct Mach reflection. However, it can also be parallel to the reflecting surface (stationary Mach reflection) or be inclined away from the reflecting surface (inverse Mach reflection).

The shear layer is often used as an indication of the transition from regular to Mach reflection because the Mach stem starts at infinitesimal length and cannot practically be resolved visually or computationally. While these shear layers are initially stable, they must naturally decay as the shear cannot be indefinitely sustained. The process by which these shear layers degrade into turbulence normally includes the formation of quasi-stable instabilities of regular forms which develop over time.

One such instability that has been noted of the compressible shear layer is the Kelvin-Helmholtz instability (KHI). Named for its initial description by both William Thomson, Lord Kelvin (Thomson (1871)) and Helmholtz (1868) in incompressible flows, this is an instability characterised by a series of s-shaped curves of the shear layer which grow in time. While there were a significant number of studies exploring the incompressible KHI experimentally, Papamoschou and Roshko (1988) were the first to consider the possibility of this instability of the compressible shear layer produced by the co-flowing of gases originally separated by a splitter plate with a sharp trailing edge.

The primary outcome of this study defining the compressible KHI is that the growth thereof correlates with a convective Mach number relating the magnitude of the velocity difference across the shear layer to the sound speed in the flow. Effectively the convective Mach number

defines the level of compressibility of the velocity shear. The conclusion was that the growth rate of the instability decreases with increasing convective Mach number until it becomes steady when the convective Mach number is supersonic. In other words, high levels of compressibility of the velocity shear will stabilise the shear layer and inhibit the growth of the KHI.

Rubidge and Skews (2014) explored the possibility of the same instability occurring in unsteady flow fields by considering the shear layer of a direct Mach reflection. They proved the existence of the unsteady KHI in these flow fields but noted that the development was subject to noise in the experimental apparatus and that it formed more readily for higher incident shock wave numbers and shallower incident shock wave inclination to the reflection surface. An example of their results is shown in Figure 2.6, where the instability gives the shear layer a braided appearance initially and then grows in size farther along the shear layer.

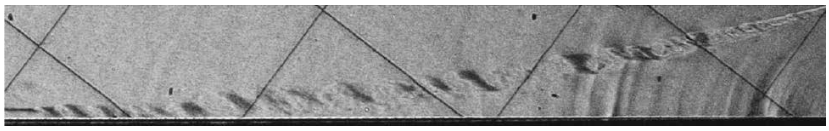


Figure 2.6: Kelvin-Helmholtz instability of the shear layer of a direct Mach reflection (shock wave at right of image) (Rubidge and Skews 2014)

2.2.2.2 Shock wave-induced vortex flows

One of the most common causes of compressible vortices is the impulsive flow generated by shock waves and so naturally these were the most common studies undertaken of compressible vortex loops.

Among the first studies to explore the behaviour of shock-induced vortex loops was that undertaken by Elder and De Haas (1952) which looked at the simple case of the vortex ring formed at the open end of a shock tube. As is well understood from studies of shock waves, the diffraction of a shock wave generally produces a region of separated flow or a vortex near the diffracting edge. The nature of this region is a function of the angle of diffraction and for corners approaching 90° there is generally a strong vortex present. In the case of a shock wave exiting the normal end of a shock tube, this toroidal diffraction will result in the generation of a toroidal vortex.

The study by Elder and De Haas was the first to generate time series of the evolution of the vortex ring formed by the shock wave exiting a shock tube cut normal to the axis of the tube based on repeated experiments. Beyond this, observations were also made of the change of the position and size of the vortex ring as a function of time. It was noted that the vortex

ring generated initially has negligible convection velocity and undergoes acceleration as the flow develops. Related to this is the growth in the vortex ring diameter and core diameter as a function of time. The growth in the core of the vortex is comparable to that seen in the incompressible study by Didden (1979) where the change is in part due to the entrainment of more fluid into the vortex. The use of an orthogonal tube exit in this study would set up a norm for studying this behaviour in compressible flows only significantly addressed by the current study.

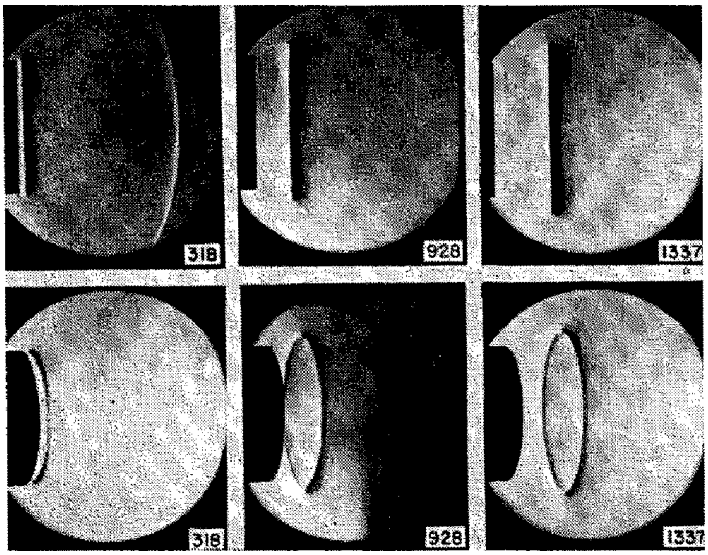


Figure 2.7: Schlieren images of vortex development at the end of an open shock tube normal (top) and at 15° (bottom) to the axis of the shock tube. Numbers indicate the time in μs from the emergence of the shock wave (Elder and De Haas 1952)

As is to be expected, the study of compressible vortex loops progressed along much the same lines as that for incompressible vortex loops and explored many of the same features. However, features unique to compressible vortex rings were also identified. In the study by Phan and Stollery (1984), which explored muzzle dynamics and was not focused on vortex rings, a significant pressure reduction at a point near the muzzle and along its axis was noted and attributed to the passage of the vortex ring formed by the diffraction of the primary shock wave out of the muzzle.

A subsequent study by Baird (1987) identified the specific cause of this pressure reduction as being due to an embedded, rearward-facing shock wave which forms inside of the vortex ring due to the high induced velocities in the core. The approach taken in this study made use of differential interferometry instead of shadowgraph or schlieren imaging to allow the embedded shock wave to be clearly visualised with little obstruction by the surrounding vortex because of the insensitivity of the method to the significantly weaker density gradients in the vortex core. An example of the images acquired using this method can be seen in Figure 2.8 where

the embedded shock wave can be distinguished as the discontinuity in the colour fringes downstream of the muzzle along the axis. In the earlier image the primary shock wave which emerged from the muzzle can be seen in the right of the image.

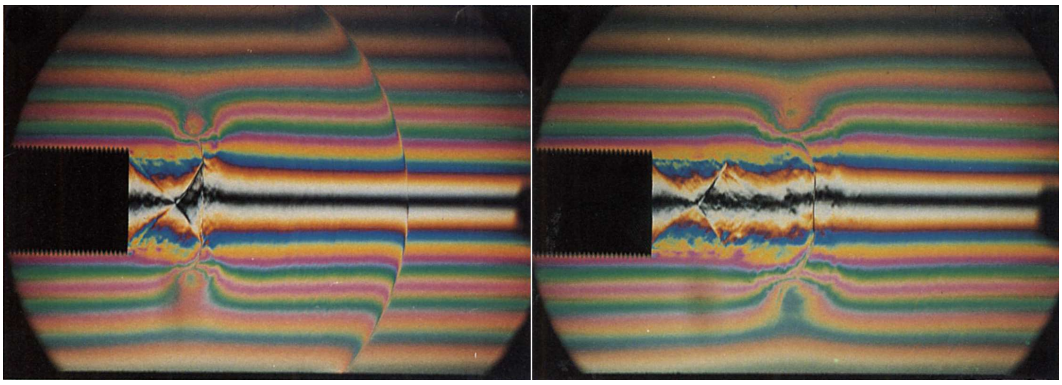


Figure 2.8: Differential interferograms of the development of the embedded, rearward-facing shock wave in the vortex ring produced from a muzzle 220 μs (left) and 380 μs after the emergence of the primary shock wave (Baird 1987)

While the embedded shock wave in a vortex ring has become an expected feature in systems of this sort, the study by Baird was one of the first to formally identify it and also to estimate the strength of the shock wave, where the Mach number of the flow entering this shock wave was approximately 1.31 (in the frame of reference of the vortex) for an initial shock wave strength of Mach 1.50. Furthermore, one of the most significant conclusions of this study was that the embedded shock wave in a vortex ring does not extend entirely to the core of the vortex but rather to a point near the vortex core at which the viscous forces tend to dominate. This effect can be observed by careful study of the later image in Figure 2.8.

Following this study, a detailed qualitative study was made of the effect of changes in initial shock wave strength on the behaviour of compressible vortex loops by Brouillette and Hébert (1997). From this it was found that for Mach numbers below 1.43, no discernible rearward-facing shock wave is formed within the vortex ring generated at the exit of a shock tube. The rearward-facing shock wave is a consistent feature in vortices produced by initial shock waves of greater strength because of the supersonic flow entering the vortex ring induced by the greater vortex circulation.

In addition to defining the limits for the formation of the rearward-facing shock wave in a shock-induced vortex ring, the study by Brouillette and Hébert also identified another feature of compressible vortex rings previously unidentified, the counter-rotating vortex ring (CRVR) formed ahead of the ring in the direction of convection. This vortex ring is induced along the inner boundary of the primary vortex ring by the shocked flow passing through the centre and rapidly increases in size as the mutual induction between the two vortices entrains the secondary vortex into the primary one. The result of this is that the secondary vortex moves

around the outer periphery of the primary vortex loop in the downstream direction at which point the two vortices merge into a poorly-defined structure. The development of this vortex can be seen in Figure 2.9.

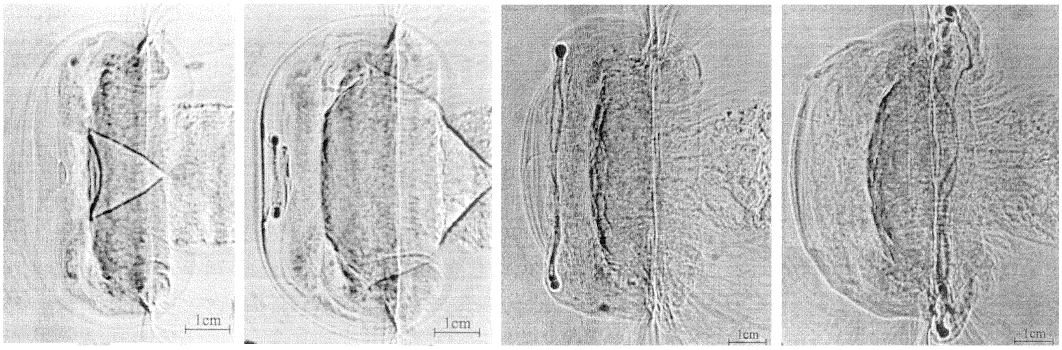


Figure 2.9: Development of the induced secondary vortex ring for an incident shock wave of M1.65 (from left to right) 330 μs, 470 μs, 740 μs, and 870 μs after the emergence of the primary shock wave (Brouillette and Hébert 1997)

The study of these secondary vortex rings, and other secondary features, has been recently extended in the work by Murugan and Das (2010) and Murugan, De et al. (2011). In the study by Murugan and Das, smoke visualisation was used to study in more detail the behaviour of the secondary vortex ring (or CRVR) formed for higher Mach numbers of the initial shock wave. Their hypothesis is that the CRVR forms as a result of a Kelvin-Helmholtz-like instability on the shear layer of the jet trailing the vortex. This is the hypothesis also explored by Lim (1997), but at significantly higher Reynolds numbers.

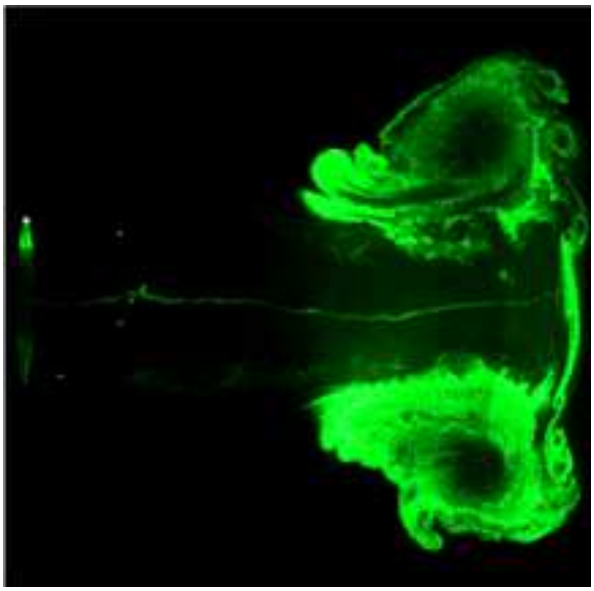


Figure 2.10: Laser sheet visualisation of multiple CRVRs formed on a high Reynolds number vortex ring (Murugan and Das 2010)

They were also able to identify conditions at later times than those studied by Brouillette and Hébert for the generation of multiple CRVRs, an example of which is shown in Figure 2.10, and showed that the dynamic behaviour of these rings is a characteristic of the shock tube length for short shock tubes. The study by Murugan, De et al. (2011) extended this work by using particle imaging velocimetry (PIV) to gather numerical data for the velocities in such a vortex ring and identified the shear layer vortices identified as part of the cause of the CRVR.

A study by Jiang, Takayama et al. (1997) explored a similar flow field to the emergence of a shock from the free end of a shock tube by considering a sudden change in area of a shock tube. An important distinction between this and the previous studies undertaken was the interaction of the reflected diffracted primary shock wave with the vortex formed at the step change. Of particular interest was the complex system of shock wave-vortex interactions and secondary induced shock waves resulting from this interaction. Specifically, the presence of the toroidal secondary shock waves embedded within the vortex ring suggests a series of regions around the periphery of the vortex which are, respectively, subsonic and supersonic. An annotated experimental image depicting the flow field at a late stage of development of these complex interactions is given in Figure 2.11

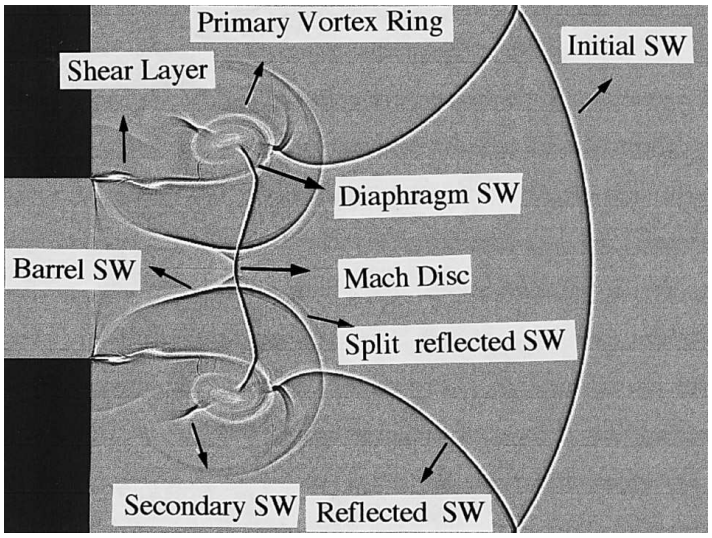


Figure 2.11: Description of shock wave-vortex interaction flow field for the sudden area change in a shock tube (Jiang, Takayama et al. 1997)

A recent study by Kleine et al. (2009) has extended the studies of the CRVR by using high-speed visualisation of the flow field to explicitly demonstrate the formation and shedding mechanism suggested by Murugan and Das, amongst others. Here it was also shown that the embedded shock wave seen in many studies is initially a toroidal shock wave formed on the shear layer rolling up into the vortex and grows to form the embedded shock wave previously

studied. This study provided a time-resolved demonstration of this process which was originally proposed by Baird (1987). In addition, it suggested that the coalescence interactions of the secondary shock waves that form into the embedded shock wave are fundamental to the formation of the CRVR.

As with the studies made of incompressible vortex loops, most work had focused on the dynamics of compressible vortex rings and little consideration had been given to the dynamics of the more general case of a non-circular vortex loops. Possibly the earliest experimental study of non-circular vortex flows induced by shock waves was that by Abe, Watanabe and Suzuki (1992) which used holographic interferometry to visualise the flow field at the open end of a shock tube of square cross-section. Although little detail of the vortex itself was visualised, it was clear from this study that the vortex evolution in time was not uniform between the centre-point and diagonal axes of the square and suggested that further study was required.

This extension of the experimental study was undertaken by Jiang, Onodera and Takayama (1999) also using holographic interferometry which allowed for axial visualisation of the flow. They also explored the case of a step change in the cross-section of a square shock tube (Jiang, Wang et al. 2003). However, neither of these studies provided significant experimental visualisation of the vortex dynamics.

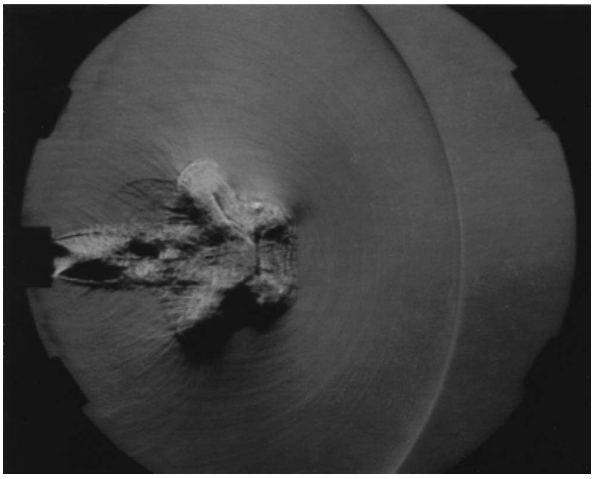


Figure 2.12: Schlieren visualisation of the flow field at the exit of a 0.4 aspect ratio elliptical nozzle approximately 320 μs after the emergence of the primary shock wave (Zare-Behtash, Kontis and Gongora-Orozco 2008)

A spate of recent studies by Zare-Behtash, Kontis and Gongora-Orozco (2008), Zare-Behtash, Gongora-Orozco and Kontis (2009), Zare-Behtash et al. (2009) and Zare-Behtash et al. (2010) have made significant advances in exploring and visualising these dynamics. In the first study, nozzles of square, elliptical and circular profiles were studied and comparisons were made of

the evolution of the vortices produced using both schlieren imaging and PIV. As can be seen in, for example, Figure 2.12 the non-circular geometry of these nozzles leads to a complex vortex structure which deforms in time. The change in dimensions and positions of these vortices with time were also mapped. As postulated by Jiang, Onodera and Takayama, it is believed that these deformations are as a result of the variation in vorticity along the core of the vortex loop as a result of the singularities of the nozzle geometry. The subsequent study exclusively used PIV to quantify this vorticity in the various parts of the vortex loop.

In the third study by Zare-Behtash, Kontis and Gongora-Orozco, the effect of the initial profile of the vortex ring was explored further and generalised representations were made of the dynamics of elliptical and square vortex loops. Although the presented behaviour of the elliptical vortex loop, Figure 2.13, corresponded well with that modelled by Kambe and Takao (1971) (see § 2.3.1), no general representation had previously been made of the dynamics of a square vortex loop. As can be seen in Figure 2.13, the general behaviour of such loops is that the region of highest curvature (the corners) will convect faster than the uncurved section of the vortex ring and the induced curvature and contraction of the vortex that results from this will cause the regions of highest curvature to change position along the vortex line. This means that the square profile of the vortex loop will undergo a transformation with the end result being that the major axes of the square are rotated by 45° and the vortex profile is again approximately plane. This differs considerably with the results of Jiang, Onodera and Takayama (1999) where it was shown that the vortex profile does not remain plane.

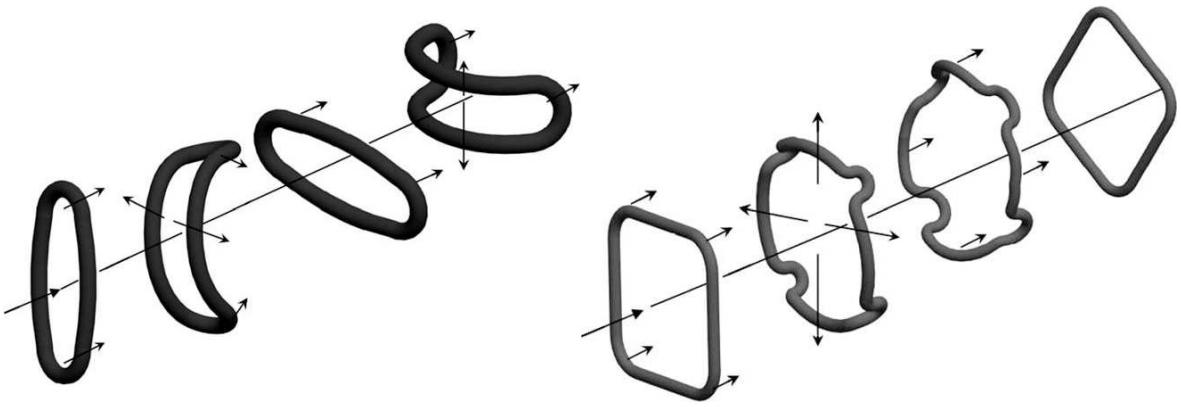


Figure 2.13: General representations of the dynamics of elliptical (left) and square (right) vortex loops (Zare-Behtash et al. 2009)

In the latest work by Zare-Behtash, Kontis and Gongora-Orozco, the extended range of nozzle geometries including lenticular orifices with singular corners was tested to specifically explore the effects of the singularities. Although the vortices produced from these nozzles are approximately elliptical, it was found that over the development of the vortex and jet the presence of the singular corner resulted in a distension of the plume behind the vortex

unlike that seen in flows from elliptical nozzles at high pressure ratios although no reason was suggested for this. An example of the nozzle profile used and the flow field with the distorted plume may be seen in Figure 2.14.

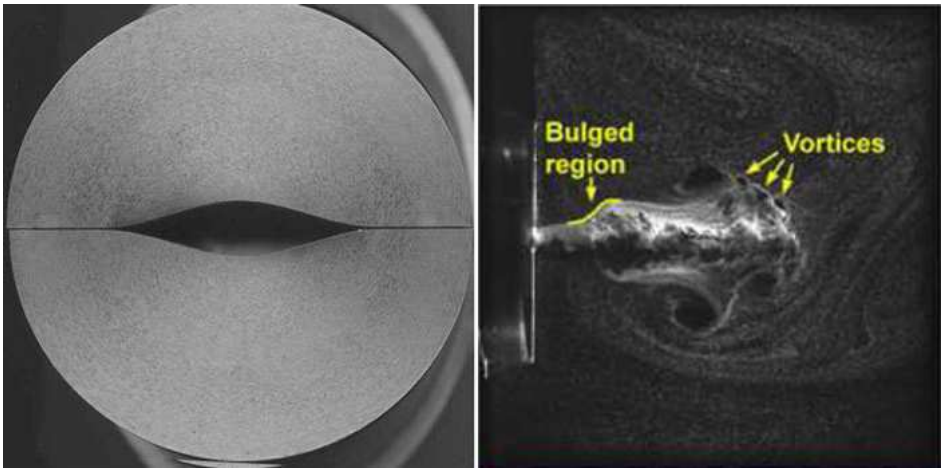


Figure 2.14: Singular lenticular orifice (left) and resulting flow field (right) (Zare-Behtash et al. 2010)

2.3 Numerical Studies

As with any other observed physical phenomenon, vorticity and vortices have provided rich material for numerical studies ranging from rigorous analytical treatments to the more modern computational modelling approaches.

2.3.1 Analytical treatments

Many of the earliest approaches to the study of vorticity and vortices were predominantly analytical. In part this was due to the attitude at the time in which it was believed that mathematics should be used to describe as completely as possible any observed physical phenomena and reconciled later with the details of the observation. Largely, though, this dominance of mathematics in early studies of vortex dynamics was as a result of the total lack of readily available means to capture data relating to unsteady behaviour such as photography. Extensive studies were thus originally made of steady, or near-steady, state vortex behaviour such as large eddies in estuaries.

As discussed in § 2.1.2, the earliest models of the vortex were two dimensional and used different specifications of the vorticity to describe different observations of the flow in vortices.

The most significant contribution in these early times were those by Rankine (1872), Hill (1894), and later Hicks (1894). However, it is the modern studies of vortex behaviour which have the greatest bearing on the current work. The study by Wedemeyer (1961) was one of the first to consider the mechanism of vortex ring formation at an orifice or tube exit. He proposed that the vortex is formed by the rolling up of the vortex sheet formed at this orifice and, based on this, modelled the formation in time of the vortex ring without swirl. Figure 2.15 shows the non-dimensionalised growth of the streamline emerging from the lip of the formation orifice according to Wedemeyer's model. As with the experimental verification undertaken as part of the study, Wedemeyer's model assumed a laminar formation behaviour and could not, therefore, be used to explore turbulent vortex behaviour.

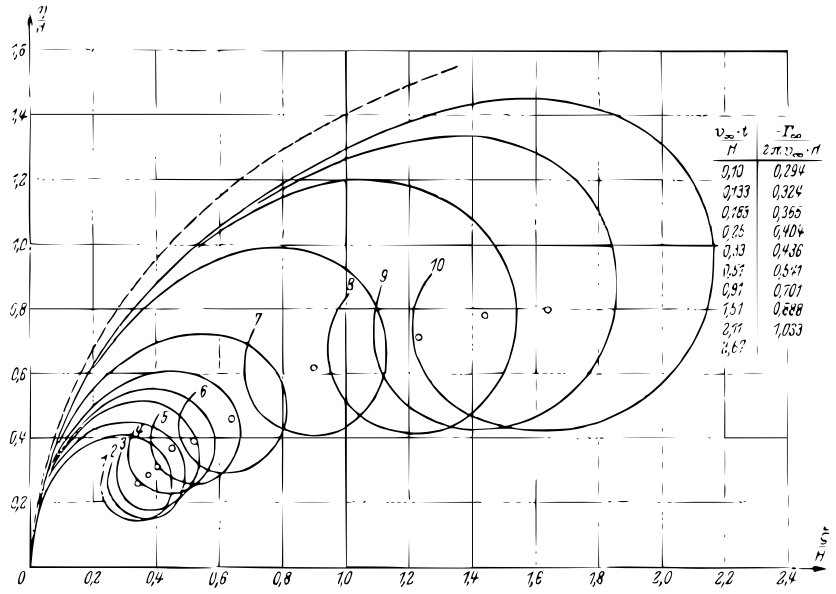


Figure 2.15: Non-dimensionalised growth of the vortex streamline (Wedemeyer 1961)

While the work by Wedemeyer was one of the first to specifically explore the mechanism of vortex formation, it was essentially a two-dimensional model and suitable only to limited cases. Following this study, therefore, there was a growing body of work which aimed to explore the dynamics of arbitrary vortices. In the large part, these studies made use of the thin circular vortex core approximation, or vortex filaments, to create a mathematical framework conducive to rigorous modelling of arbitrary vortices. The works by Hama (Hama (1962) and Hama (1963)), and Betchov (2006) all explored the dynamics of a free vortex filament with curvature and specifically the effects of that curvature on the change in shape with time of the vortex filament. These models all used the LIA, where the effect of a portion of a vortex filament is only significant in a region near it because of the small cross-section. In the case of Betchov, this was derived as a simplification of the Biot-Savart law which expressed the induced velocity at any point in space as a result of circulation.

In the case of Hama, a different approach was taken in part due the objective of the study being to explore the transition from laminar to turbulent flow assuming a strong effect of vorticity in this process. In all these cases it was found that in cases of localised induction, the curvature of the vortex filament has a strong effect on the deformation of the vortex loop, where higher filament curvature results in proportionally higher self-induced convection speed.

Working from the basis of the concept of self-induction for slender vortex filaments, Viets (1972) and Kambe and Takao (1971) explored the dynamics of specific vortex loop geometries. In the case of Viets, the focus was specifically on elliptical vortex loops of various profiles. Kambe and Takao made a broader study as they too were exploring questions of transition to turbulence but specifically that of the decay of vortex rings. As an analogue to the waves which had been identified on decaying vortex rings, Kambe and Takao wished to model modal perturbations of circular vortex rings to produce several azimuthal waves and hence explore the dynamics of these perturbed rings as a possible cause of the transition to turbulence.

On the basis of a simplification made to the LIA, Kambe and Takao were able to model several cases of the motion of perturbed vortex rings. Examples of the behaviour can be seen in Figures 2.2 bottom and 2.16 for elliptical and trilobal vortex loops respectively. These models specifically showed that the greater induced velocity of sections of the vortex loop with greater curvature would cause new regions of increased curvature which would then convect faster than the formerly faster portions. The result was that the vortex loops would deform from plane profiles and portions formerly of lowest curvature would become portions of highest curvature. The nett result of this was periodic motion in which the vortex loop would undergo a swapping of the orientations of the major and minor axes of the deformed profile, ignoring the effects of viscosity.

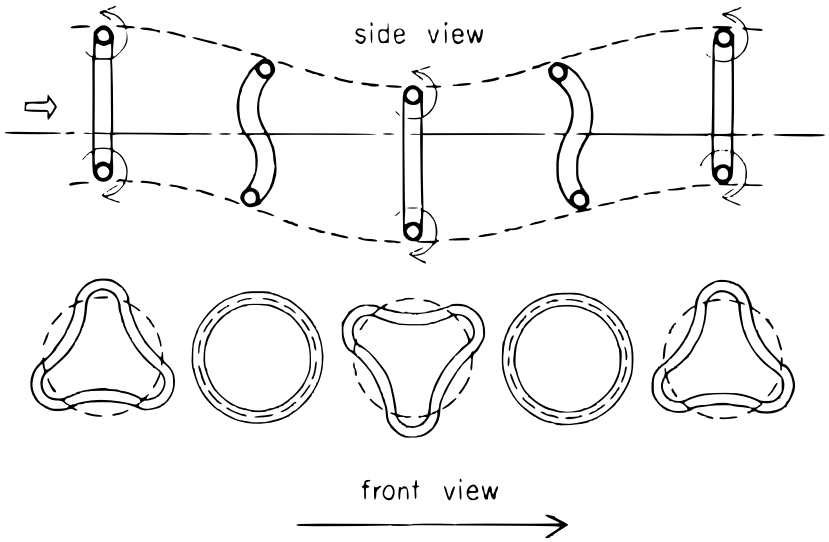


Figure 2.16: Calculated deformation of trilobal vortex loop (Kambe and Takao 1971)

The subsequent study by Widnall and Sullivan (1973) used a similar framework to extend the study of azimuthal waves as a cause of the transition to turbulence of vortex rings with the important difference that the vortex core was small but not infinitesimal. The result of this analysis was that vortex rings in ideal fluids are almost always unstable and that the effects of viscosity could only serve to exacerbate this behaviour.

Most analytical studies of vortex loop dynamics had explored incompressible fluids due to the complexity which compressibility adds to the fluid property interactions. This has remained almost exclusively the case though some studies were made exploring the effect of compressibility on specific properties of vortex loop behaviour. For example, the study by Moore (1985) made some attempt at describing the effect of compressibility on the propagation speed of a vortex ring though no conclusive model resulted. One issue clearly identified by the study was that transonic and supersonic vortex filament velocities could not be modelled analytically because of the effects such flows would have on the consistency and isentropy of the vortex cores. There has thus been almost no subsequent analytical work in this regard.

2.3.2 Empirical treatments

Given the limitations of analytical methods highlighted by comparison with physical observations, empirical methods have often been pursued as a means of developing mathematical treatments of vortex dynamics that encompass phenomena typically precluded by the assumptions of analytical models. A typical example of this is the study by Didden (1979) which explored the formation behaviour of vortex rings. From careful observation of the flow field induced by the piston-driven ejection of fluid from a submerged, sharp-lipped tube he was able to determine relationships describing the change in various vortex parameters as functions of time.

By and large though, the focus of empirical studies has been on the identification of parameters affecting the transition of vortex rings to turbulence. As an example, the study by Auerbach (1991) identified non-dimensionalised limits for the ranges in which various phases of the transition of a laminar vortex to turbulence (as previously identified in Auerbach (1988)) could exist and the difference in the behaviour of the vortex in each of these, such as the degree of entrainment of fluid originally downstream of the forcing orifice versus fluid ejected from the orifice.

2.3.3 Computational Fluid Dynamics

The tool which has undoubtedly come to be one of the most widely used in the study of unusual vortex dynamics is that of computational fluid dynamics (CFD). Use of CFD has been made almost exclusively in only the most recent studies due the requirement of access to suitable computing facilities. Possibly the earliest identified study of vortex loop dynamics using CFD was that by Oshima (1988) in which the dynamics of elliptical vortex loops of various aspect ratios were modelled. Although the images shown in Figure 2.17 may seem simple by today's standards, this study was quite ground-breaking in that it considered the propagation of non-circular vortex loops in a fully three-dimensional domain.

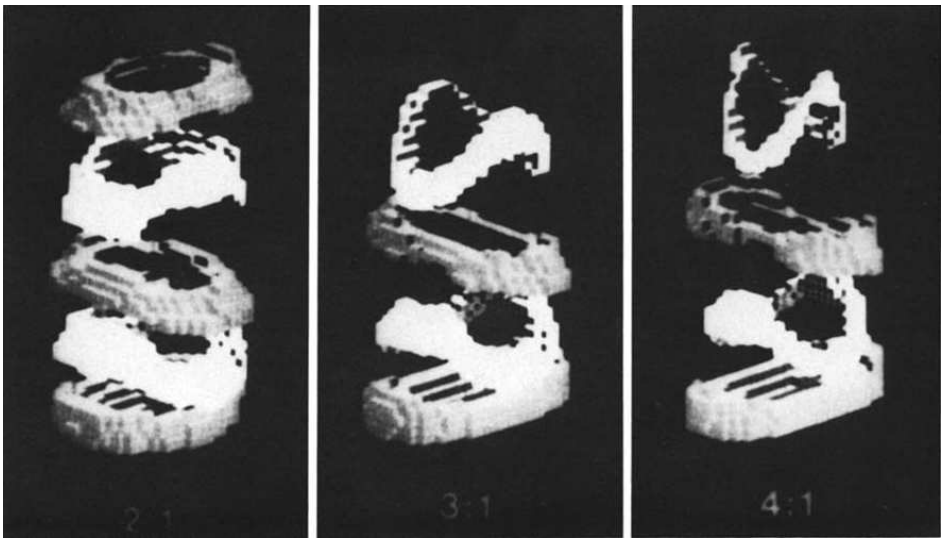


Figure 2.17: Propagation of elliptical vortex loops (from left to right AR = 2, 3, 4) (Oshima 1988)

By contrast, studies at that time were typically limited to two-dimensional fields and aimed at exploring various models to determine the most suitable for use in particular regimes. One example of this was the study by Brown and Minion (1995) which explored the formation of vortices on incompressible shear layers.

Since then, the use of CFD in the study of vortex dynamics has become commonplace. As with the experimental studies, many of the computational studies have explored the dynamics of vortices induced by body motion or fluid motion past a body, and the forces these exert on the bodies in question. The use of CFD in the particular context of vortex rings has also allowed for detailed mapping of the processes in time and space which may be impossible experimentally. The study by Krueger (2008), for example, allowed for detailed modelling of the circulation as a function of time and forcing parameters, such as the orifice diameter, to be accurately modelled providing validating insight specifically to the formation of the vortex ring. Another study by Kollmann (Kollmann (2011a) and Kollmann (2011b)) has allowed

for detailed study of the interaction of swirling vortex rings and the decay of these swirling vortices into turbulence. This study has been one of the first to provide detailed topologies of these interactions and precise quantitative data of the changes in the velocity and vorticity fields as a function of time. An example of the complex topologies successfully resolved by the use of CFD is given in Figure 2.18. The surfaces shown are isosurfaces of enstrophy, which is the quantity related to kinetic energy which corresponds to the dissipation effects in the fluid.

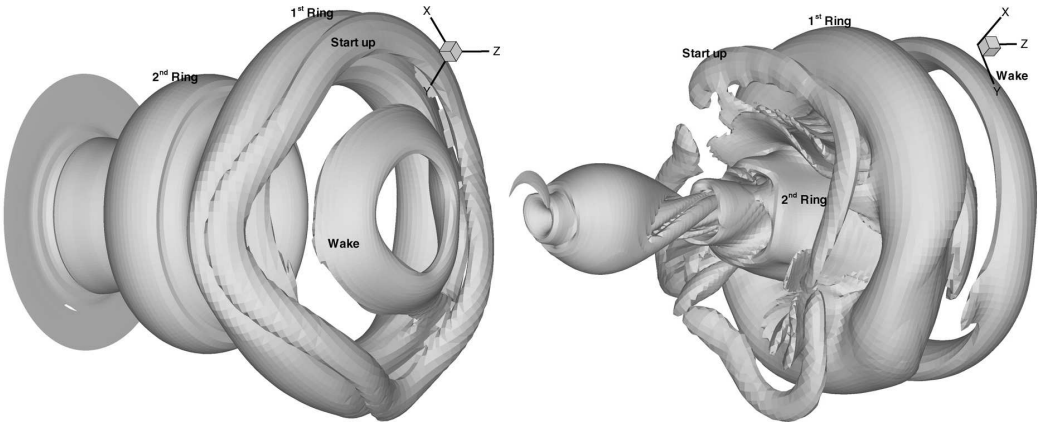


Figure 2.18: Isosurfaces of enstrophy for interacting swirling vortex rings (Kollmann 2011b)

An additional benefit of the use of these methods is the ability to plot isosurfaces of various flow parameters. Experimental visualisations of vortical flow fields are typically limited to visualisation of velocity, by the use of scalars possibly with additional processing (e.g. PIV), or gradients of tensors such as density (e.g. schlieren imaging). One particular development that has been beneficial to the modelling of vortices is the technique proposed by Jeong and Hussain (1995) which plots isosurfaces of the λ_2 eigenvalue of the velocity tensor. The λ_2 method defines a vortex in terms of eigenvalues of the symmetric tensor $\boldsymbol{\mathcal{S}}^2 + \boldsymbol{\Omega}^2$ where $\boldsymbol{\mathcal{S}}$ and $\boldsymbol{\Omega}$ are respectively the symmetric and antisymmetric parts of the velocity gradient tensor $\boldsymbol{\Delta}\mathbf{u}$. This method therefore identifies the pressure minimum in a plane perpendicular to the vortex axis and produces vortex geometry which is intuitively clear. Although intended for incompressible flows, this method is one that has a simple implementation and produces images which accurately represent vortices observed experimentally and has become known as an industry standard for this purpose.

While the studies identified so far have focussed primarily on body motion-induced vortex flows, work has also been done in studying the vortices induced by shock waves. One example of this by Sun and Takayama (2003) explored the classical case of the vortices produced by the diffraction of a shock wave over a corner. Specifically, the secondary vortex structures previously identified in inviscid numerical models but not observed experimentally were studied and it was found that these features were produced in a Navier-Stokes model but that the application of various turbulence models could suppress these. The use of such a numerical

'experiment' allows one to identify the causes of various phenomena. In this case, it was found that the dissipation of vorticity by the turbulent dissipation inherent in a turbulence model applied to such a field dampens the formation of these features. This suggests that they would be dependent on viscosity and thus may be subject to variation with the Reynolds number of the flow. There is also the possibility of three-dimensional effects changing the appearance or presentation of such features. The use of such a model could therefore suggest revision of phenomena studied at length scales quite different to the original observation which may have triggered the study.

Regardless of the exit orifice diameter profile, studies to date have focused almost exclusively on plane exit surfaces normal to the axis of the exhaust tube. From observation of the everyday world it is apparent, however, that most of the orifices from which vortices may be generated involve inclination, curvature, or both, of the exit surface. Only one previous study by Kim, Kweon and Setoguchi (2003) has been identified which explores such dynamics. Here the field of interest was that of a plane shock wave diffracting from the inclined plane exit of a shock tube of circular cross-section. The focus of the study was primarily on the CFD techniques being tested and the experimental results were gathered only for validation purposes. Although perhaps not consequential, the experimental images gathered were of poor quality and few or none of the detailed features could be discerned, as can be seen in Figure 2.19.

2.3.4 Conical shock wave interactions

A specific case of particular interest in the current field is the behaviour of conical shock waves. Interest in these particular shock waves arises primarily from two fields of research and development: scramjet engine intakes and compression of fusible materials for fusion power generation. While the former is principally a steady state condition, the latter is inherently dynamic.

2.3.4.1 Steady conical flows

Steady conical shock waves are common. While these may be axisymmetric, such as in the case of an attached shock wave for a sharp bullet or missile; they may also be non-axisymmetric, such as in the shock wave attached to the nose cone of a supersonic jet fighter craft where the nose is typically no longer a symmetrical right cone. Generally they are external shock waves attached to the leading edge of an object with a supersonic relative flow. These shock waves can form a sharp point if the leading edge of the generating object, here a cone, is sharp and the wave remains attached to the cone. The attachment to the cone

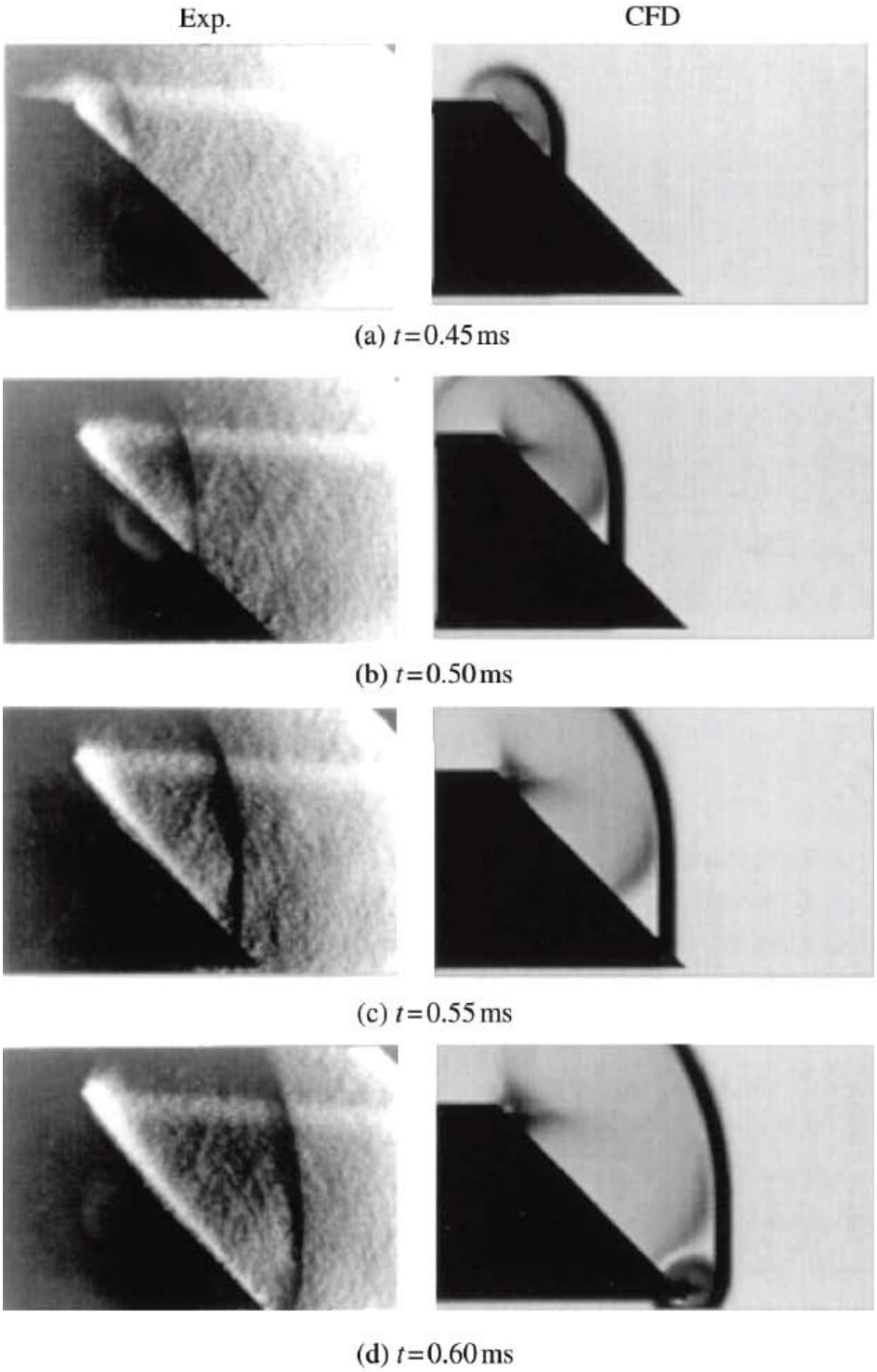


Figure 2.19: Comparison of experimental and computational diffraction of a plane shock wave at the inclined plane exit of a shock tube (Kim, Kweon and Setoguchi 2003)

is a function of the cone half-angle and free-stream Mach number. However, the conical shock waves of interest in this context are concave cones (rather than the convex cones relative to the upstream direction of flow). Such waves arise as internal flow features of ring-shaped

apertures in a supersonic free-stream, the readiest example of which would be a cylindrical supersonic inlet.

Due to the deflection of flow away from the axis of symmetry by a shock wave inclined toward the upstream direction, there is a physical constraint in that such flow would violate the continuity of mass and require the spontaneous destruction of mass at the axis. A solution was proposed by Courant and Friedrichs (1948) that there must be a Mach reflection on the axis. This Mach reflection must form at the axis to break the conical symmetry since the Mach stem would be perpendicular to, and allow for a streamline along, the axis. However, no Mach stem is apparent in experimental observations of such flows.

Various approaches to testing the Courant and Friedrichs conjecture, both experimental and computational, were undertaken in the following years. Following studies by various groups, Mölder et al. (1997) undertook a combined experimental and computational experiment to assess this possibility. As in previous experiments, no Mach disc was immediately visible in several of the parameter combinations (shock angle and Mach number) tested. Since a Mach reflection cannot form for weak waves at such shallow angles, the theory was advanced that the incident conical shock wave curves near the axis to increase the angle and thus a Mach reflection may form. The initial computational results also did not show evidence of the Mach disc. However, on refining the model to very high spatial resolution, the predicted Mach disc was observed with the curvature (indicated by the change in angle) of the shock wave upstream.

2.3.4.2 Cylindrical shock wave dynamics

The dynamics of conical shock waves can be thought of as an extension of the case of a collapsing cylindrical shock wave. Whereas the angle of the cylindrical shock wave surface to the axis is 0 (it is parallel to the axis), the angle of a conical shock wave is non-zero and thus the flow near the axis can be expected to be quite different. It is therefore germane to consider previous studies exploring the dynamics of collapsing cylindrical shock waves.

The case of a cylindrical shock wave had been considered theoretically by Guderley (1942). The first experiments to practically study the behaviour of these shock waves were performed by Perry and Kantrowitz (1951). The apparatus was an annular shock tube which converted a plane incident shock wave into a cylindrical one through propagation around a tear drop-shaped insert in a tube which produced an annular gap at the end of which the shock wave was bent through 90° to form a cylindrical shock wave propagating between the insert and the transparent end wall.

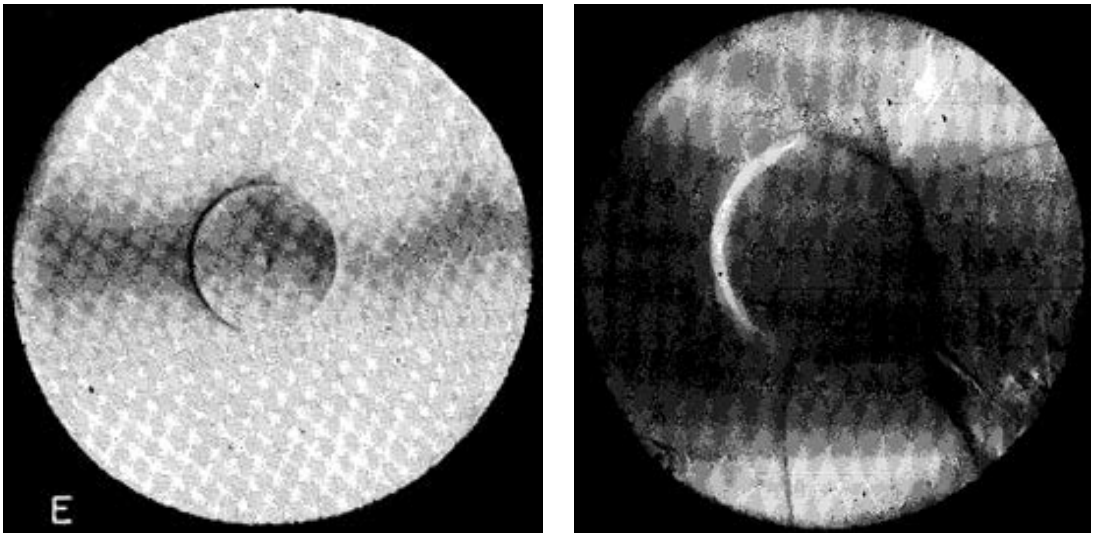


Figure 2.20: Experimental schlieren images by Perry and Kantrowitz (1951) showing the convergence of a weak cylindrical shock wave in air (*left*) and reflections developing on a stronger cylindrical shock wave as a result of random disturbances (*right*)

It was shown in the study that cylindrical symmetry breaks down when the radius of curvature of the cylindrical shock wave becomes small and that this effect becomes more pronounced as the strength of the initial shock wave increases. The breakdown of cylindrical symmetry usually occurs in the form of reflections forming in the wave front. While these were produced by the introduction of a perturbation in the path of the shock wave, such disturbances also seemed to arise randomly. Examples of the images produced by Perry and Kantrowitz (1951) are shown in Figure 2.20.

This work was extended by Takayama, Kleine and Grönig (1987) by comparison of the cylindrical shock wave dynamics in two different facilities. Each of these facilities was similar in concept to that used by Perry and Kantrowitz (1951) but with differences in scale, the precise construction of the annular insert, and in the use of holographic interferometry to visualise the flow field. In this work it was then shown that the geometry of the instability of the cylindrical shock wave near the focusing axis is related to the perturbations introduced by the annular insert supports upstream of the end wall corner, with a direct correlation between the number of perturbation sources and the number of lobes of instability in the focused shock wave. This suggests that the mechanism of distribution of curvature along the shock wave surface does not completely remove such upstream influences and that the eventual geometry formed at the focus is sensitive to this, which affects the design of future apparatus. A comparison of the interferograms produced in a shock tube with three or four insert supports is shown in Figure 2.21.

The study by Eliasson, Apazidis and Tillmark (2007) was undertaken to determine the possibility of tailoring the shape of a collapsing cylindrical shock wave by means of the geometry and layout of struts. They were able to demonstrate that resultant wave geometries of quite arbitrary profile could be generated through combinations of struts of various sizes as well as relative position.

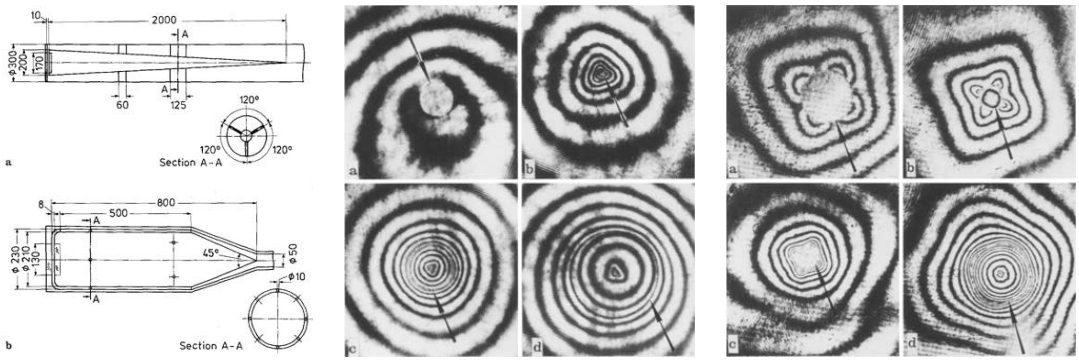


Figure 2.21: Comparison of the experimental apparatus used (*left*) and holographic interferograms of the corresponding instabilities of the converging cylindrical shock waves produced by each of the apparatus (*centre* and *right*) (Takayama, Kleine and Grönig 1987)

More recently studies of collapsing cylindrical shock waves were undertaken in which the objective was confirmation of the self-similarity constants for the propagation of the shock wave as a function of time (Kjellander, Tillmark and Apazidis (2011)). This was undertaken for several gases and successfully identified the relevant constants. However, as with previous experiments, the symmetry of the wave broke down at small radii. The same group then considered that the objective of high pressure and temperature at the axis could be achieved by properly shaped polygonal shock waves rather than trying to stabilise a cylindrical shock wave (Apazidis, Kjellander and Tillmark (2013)). The geometry of the struts was tailored to minimise the energy losses associated with the reflection of the incident shock wave off of blunt struts and the resultant focus produced successful ionisation of the air under loading.

2.3.4.3 Conical shock wave dynamics

Following the fairly extensive work on cylindrical shock waves and conical shock waves in steady flows, Barkhudarov et al. (1991) undertook a comparative experimental and theoretical analysis of the shock waves generated from toroidal ring wedges lined with a large number of spark gaps. The primary result of this study was that a Mach disc is formed on the axis of symmetry though, as with the steady state flows, in some instances the reflections appeared to be regular. As with the original proposition by Courant and Friedrichs, the idea was suggested that the Mach disc at the axis in such cases is very small. The later work

by Mölder et al. bears this out. The images obtained by Barkhudarov et al. can be seen in Figure 2.22.

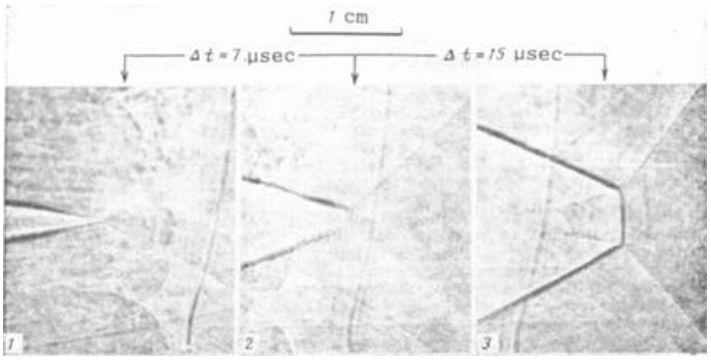


Figure 2.22: Experimental images of reflection of a conical shock wave generated by a toroidal ring wedge (Barkhudarov et al. (1991))

The primary origin of this study, however, is in the consideration of the shock wave dynamics at the end wall of a shock tunnel, where a shock wave is used to produce a high enthalpy reservoir state behind a nozzle. The interaction of the incident shock wave with the nozzle geometry produces reflected shock waves of a conical profile which interact at the axis of symmetry of the system. This problem was abstracted in Hornung (2000) to the rupture of a conical diaphragm and the resulting flows as a function of the initial shock wave strength were identified. This was extended in Hornung and Schwendeman (2001) where the results from different computational methods were compared and found to be in good agreement.

From the outset it was emphasised that regular reflection of the shock waves at the axis cannot occur and that all reflection types are variations of the Mach reflection. Thus, the primary characteristics used to distinguish the various modes of reflection of conical shock waves from the axis of revolution are the shape of the Mach stem produced and the vortices affecting this shape. The basic layout of each type is given in Figure 2.23.

The S-type, or simple type, of reflection is that which most closely resembles the simple, two-dimensional Mach reflection of a shock wave. There are two significant differences to note: the significant curvature of the Mach stem near the triple point and the shallow angle of the reflected wave. This is so pronounced that the reflected wave and Mach stem appear to be continuous in curvature through the triple point. However, as indicated in the original paper, the S-type reflection is small in scale and the spatial resolution is low compared to the solution for the other two configurations. The shallow angle of the reflected wave relative to the axis is local behaviour and changes upstream of the triple point when the reflected wave shape changes due to curvature of the shear layer to run parallel to the axis and then subsequently with the contact surface from the rupture of the conical diaphragm.

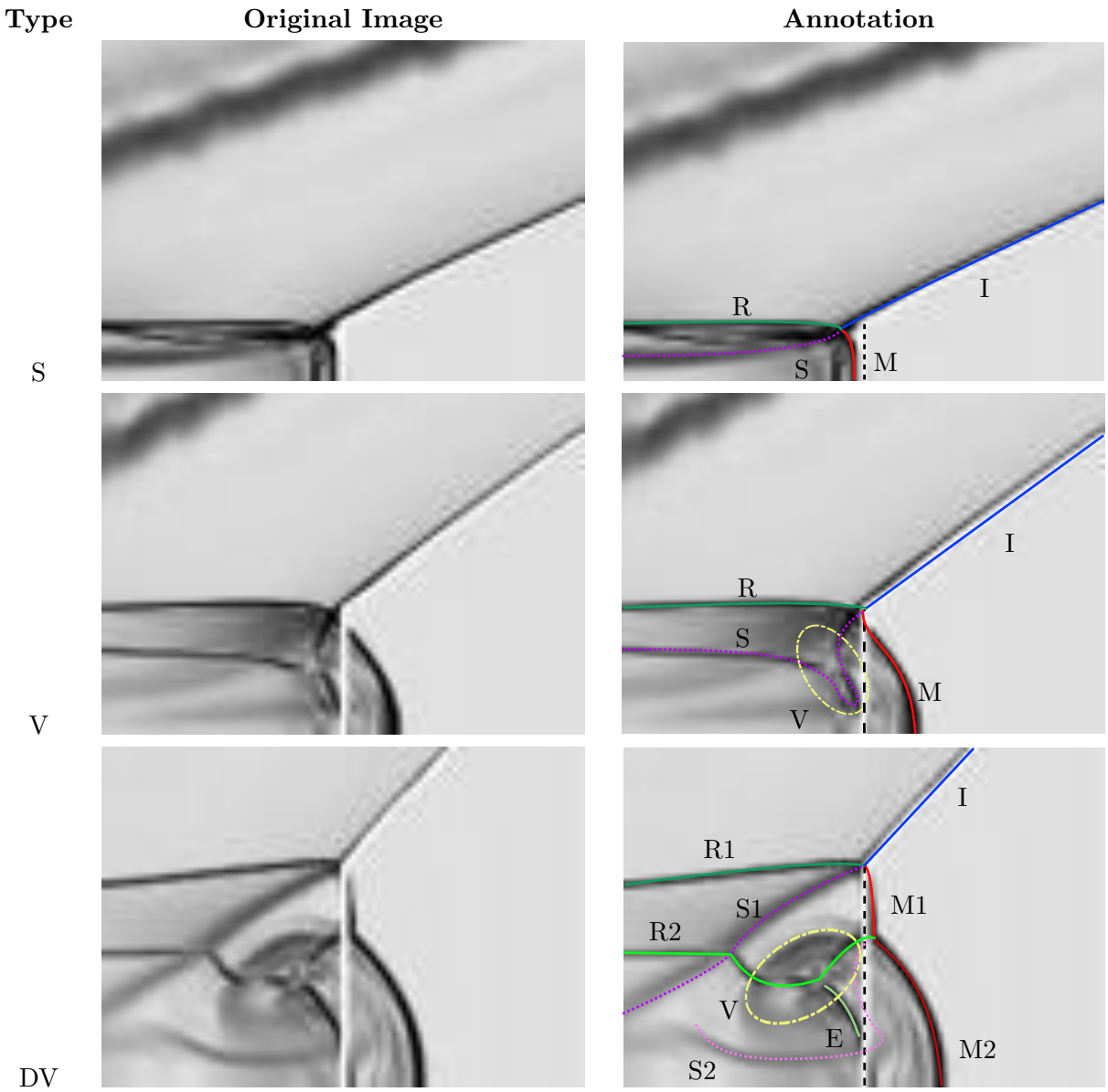


Figure 2.23: Pseudoschlieren images of the types of conical shock wave reflection patterns (S, V, and DV). Detailed views of the reflection types as given in Hornung and Schwendeman (2001) with additional annotation indicating (primary or secondary as appropriate): the incident shock wave (I, blue); the primary reflected wave (R / R1, dark green); the primary shear layer (S / S1, purple); the primary Mach disc (M / M1, red); the vortex (V, yellow); the secondary reflected wave (R2, light green); the secondary shear layer (S2, pink); the secondary Mach disc (M2, dark red); the induced, vortex-embedded shock wave (E, medium green); and the theoretically estimated position of the plane Mach stem from shock dynamics theory (Whitham 1959) by the dashed black and white line. In all images the bottom of the image represents the axis of symmetry

The next most complex of the reflection types is the V-type, or vortical type, reflection. This configuration is characterised by the significant curvature of the Mach stem downstream of

axial position of the triple point. This is caused by the influence of the vortex ring formed along the axis by the jetting of the fluid from the early reflection near the apex of the conical shock wave. This vortex induces flow through the centre of the ring and hence along the axis which causes local strengthening of the Mach stem. This portion of the wave thus translates farther downstream and the wave assumes the curved shape shown. Also, in contrast with the S-type reflection configuration, the shear layer emanating from the triple point undergoes a convoluted deviation through the vortex before continuing downstream along a trajectory away from the axis. Here the shear layer and reflected wave seem to terminate in the contact surface downstream.

The most complex of the reflection configurations identified by Hornung is the DV-type, or double vortex type. This type is related to the V-type in that the vortex influences the shape of the Mach stem but differs in that the Mach stem is dominated by the vortex in the V-type while only part of the Mach stem is deformed in the DV-type. The most characteristic feature of this configuration, however, is the presence of a second triple point on the primary Mach stem caused by the stronger vortex flow. This causes the outer portion of the Mach stem to more closely resemble that for the S-type, while the inner portion resembles the V-type with a second reflected wave and shear layer emanating from the second triple point.

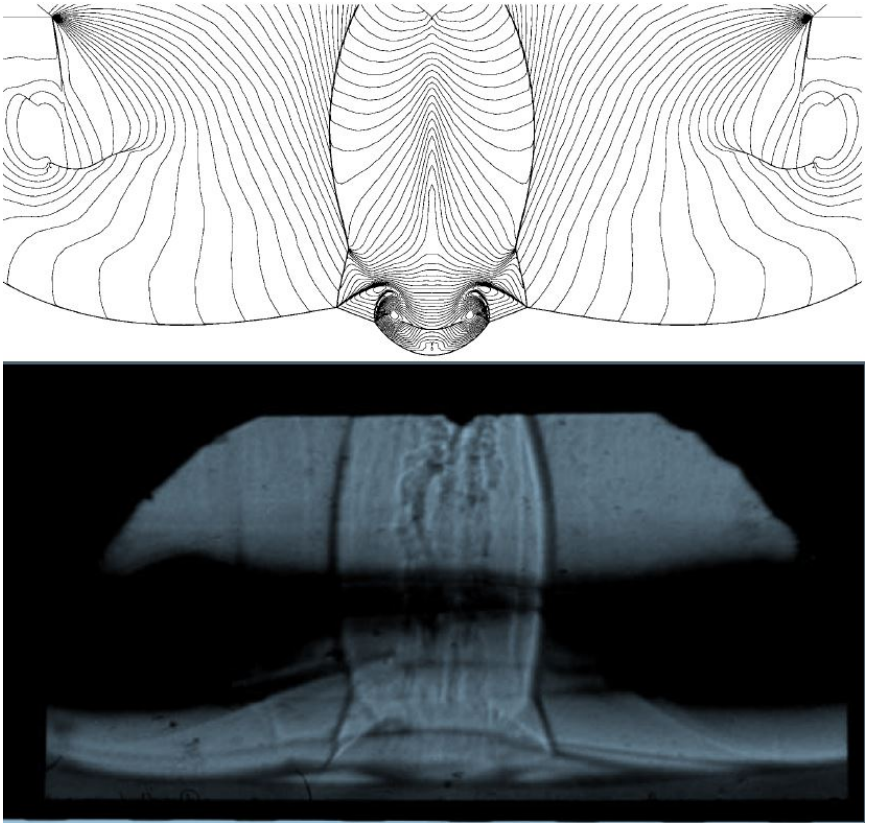


Figure 2.24: Comparison of numerical and experimental results showing DV-type reflection (Skews, Menon et al. 2002)

The second reflected wave passes through the vortex and then interacts with the primary shear layer and, later, the primary reflected wave and contact surface. The vortical flow is strong enough nearer the axis that an embedded shock wave is induced within the vortex and the presence thereof also causes the secondary shear layer to be deformed downstream of the triple point before eventually passing into the aperture of the vortex ring and dissipating in the primary shear layer.

An experimental apparatus was developed by Skews, Menon et al. (2002) which was used to test the configurations described by Hornung. They were able to produce the V- and DV-types of reflection both experimentally and computationally but did not observe the S-type experimentally. Again, the small scale of S-type reflection and limited spatial resolution of the visualisation would have made this difficult to discern from the experimental schlieren images because of the high density gradients in the vortex loop shed from the outer edge of the tube aperture. Their comparison of the numerical and experimental results showing the DV-type reflection is shown in Figure 2.24.

2.4 Conclusion

There is a clear gap in the understanding of the diffraction of shock waves from non-orthogonal exits and the flow phenomena that this produces in two primary ways. This first is that the behaviour of conical shock waves has been well considered computationally but that there is a dearth of experimental studies exploring the parameters affecting the reflection patterns of the primary shock wave. Also, since conical shock waves cannot form regular reflections, there will certainly be shear layers following the Mach reflection and thus the possibility of instabilities thereof.

The second way in which shock wave diffraction from non-orthogonal exits is not yet clearly understood is in the effect of the surface inclination or curvature on the diffracted shock shape and the vortex formed at the diffraction edge. Since no vortex is shed for very shallow diffraction angles, there exists the possibility of shock diffraction from a pipe exit where there is no vortex shed for at least part of the periphery. In such cases, the development of the remainder of the vortex in time is uncertain since it may not form into the vortex loop commonly seen with diffraction from the normal exit of a shock tube.

Chapter 3 Objectives

The over-arching objective of this study is to compare and contrast the flow fields produced by shock waves diffracting from non-orthogonal apertures. Consideration is given to the shock wave shape after diffraction and other flow features such as expansion waves, vortices, and other phenomena which may arise in the flow field. To explore this more fully, the following detailed objectives are proposed:

1. Explore the flow field produced by a collapsing conical shock wave
2. Experimentally observe time-resolved evolution of the vortices produced at the inclined plane exit of a shock tube
3. Characterise the development of the principal features of such vortices as they develop in time
4. Additionally observe the behaviour of vortices produced at the curved exit surface of a shock tube
5. Develop detailed CFD models to facilitate the identification of features not readily resolved from experimental images

Chapter 4 Apparatus

4.1 Overview

The study undertaken was predominantly experimental, with appropriate use of CFD to complement the results gathered experimentally and provide insight into flow features which cannot be discerned using typical flow visualisation and measurement techniques. Two different facilities were used for this with similar flow visualisation methods applied.

4.2 Experimental Apparatus

4.2.1 Flow at the oblique exit of a shock tube

The shock tube used for the study of the diffraction of a shock wave from the oblique exit of a shock tube was a conventional, diaphragm-restrained shock tube as shown in Figure 4.1. The cross section of the shock tube was circular with an internal diameter of 92 mm. Both the driver and driven gases were air with the driven section at ambient conditions of approximately 300 K and 83 300 Pa.

In this study the diaphragm material used was polyester film of either 50 μm or 100 μm in thickness and used in combinations up to 400 μm. The diaphragm was allowed to rupture naturally under the pressure loading resulting in Mach numbers ranging from approximately 1.25 to 1.6.

Two different types of test section were used in characterising the behaviour of shock waves undergoing oblique diffraction. The first was characterised by an exit surface which was plane and inclined by a fixed angle, α, to the tube axis normal (i.e. the shock wave plane before diffraction). An example of one of these test sections is shown in Figure 4.2. The angles of inclination of the plane exit surface tested were 30°, 45°, 60°, and 75°.

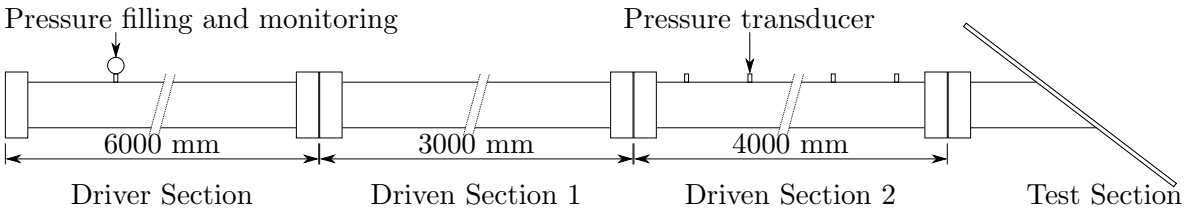


Figure 4.1: General arrangement of conventional shock tube used for oblique exit study

The plane exit surfaces were used as these define a continuous variation in local diffraction angle, α_ϕ, from the most obtuse at the extreme upstream point of diffraction located in the vertical symmetry plane of the tube (an azimuth of $\phi = 90°$) to the most acute at the extreme downstream point of diffraction located in the vertical symmetry plane of the tube (an azimuth of ϕ = -90°). The points of 90° diffraction lie in the horizontal symmetry plane of the tube. This variation of diffraction angle around the diffraction edge would mean a continuous variation from a strong, obtuse diffraction at the extreme upstream diffraction point (where the flow field is mostly independent of the diffraction angle) until the horizontal symmetry plane after which point the diffraction would weaken until the weakest diffraction takes place at the extreme downstream position.

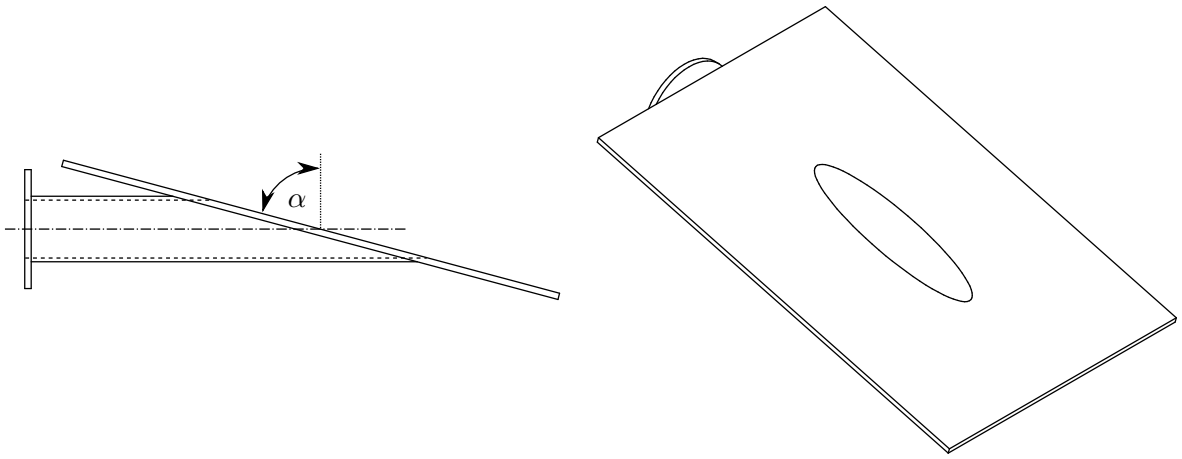


Figure 4.2: Plane exit test section inclined 75° to shock normal (elevation (*left*) and isometric (*right*))

To generalise the consideration of a shock wave diffracting from an oblique exit, the case of one cylindrical pipe intersecting the side of a second cylindrical pipe orthogonally was considered. In this case the ratio of the radii of the shock tube (inner diameter 4" / 101.6 mm) and the exit surface, RR, was identified as a characteristic dimension. Since a large value of RR would approximate a flat plate and a small value of RR would define the diffraction of a shock wave into a second pipe of equal radius, radius ratios of approximately 3 (3.01 for an exit surface of radius of 153.5 mm) and 5 (4.78 for an exit surface of radius 244 mm) were selected to give an indication of the effect in the rate of change of azimuthal diffraction angle on the studied flow field.

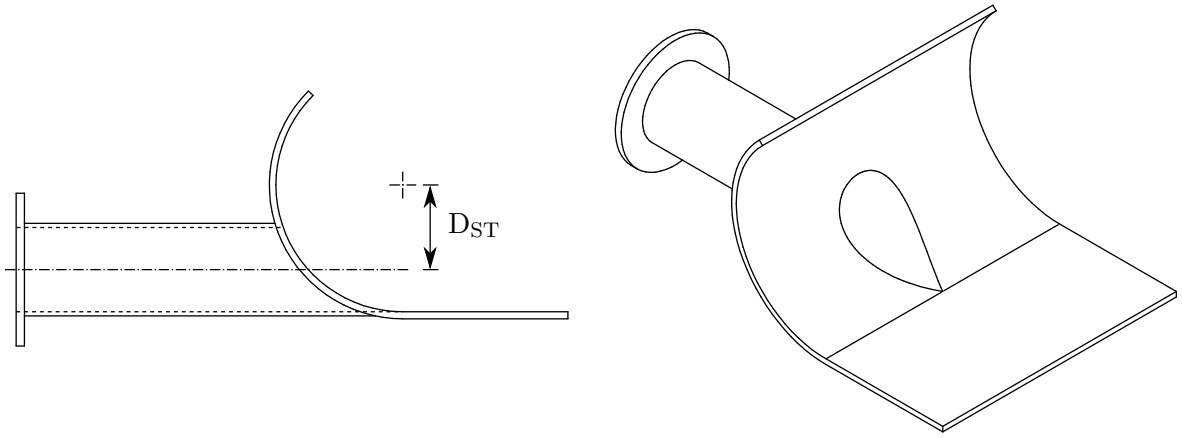


Figure 4.3: Radius ratio 3 (RR3) model with tangent exit (elevation (*left*) and isometric (*right*))

Three test sections were created to explore this parameter field. Two of the models were designed so that the centreline of the shock tube was offset from the centreline of the exit cylinder by one shock tube diameter. For RR = 3 (hereafter RR3) this resulted in the shock tube inner surface being tangent with the inner surface of the exit cylinder, as shown in Figure 4.3. Thus an extension plate was fitted at this position to observe the effect of the limiting condition of no diffraction of the shock wave at one point along the diffraction edge while strong diffraction occurs at the other extreme (a diffraction angle of approximately 107°). For the RR5 model, the offset of one shock tube diameter from the centreline of the exit cylinder resulted in a more general case of limiting azimuthal diffraction angles of 51° and 102°. This geometry is shown in Figure 4.4

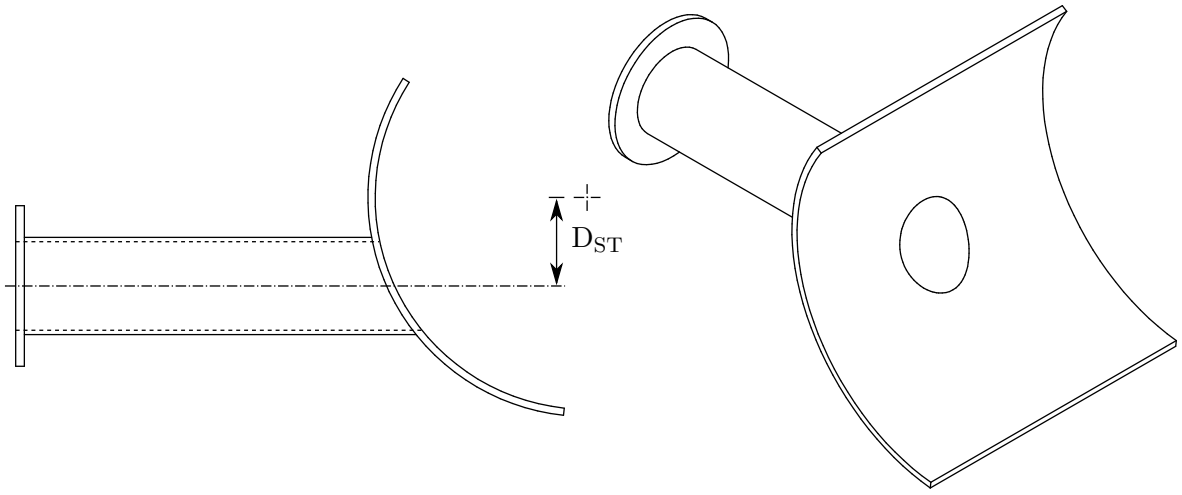


Figure 4.4: Radius ratio 5 (RR5) model with centreline of shock tube offset from exit cylinder centre by D_{ST} (elevation (*left*) and isometric (*right*))

To complete the geometric range studied, a third RR3 model with the edge of shock tube placed on the centreline of the exit cylinder, resulting in a maximum diffraction angle of 90°,

was tested so that the effect on vortex behaviour of strong diffraction could be limited and to place the strongest diffraction in the vertical symmetry plane for purposes of visualisation. This resulted in an acute diffraction angle limit of 48°, close to that in the RR5 model allowing for vertical symmetry plane comparison of the effect of different curvatures on the acute diffraction region of the flow field.

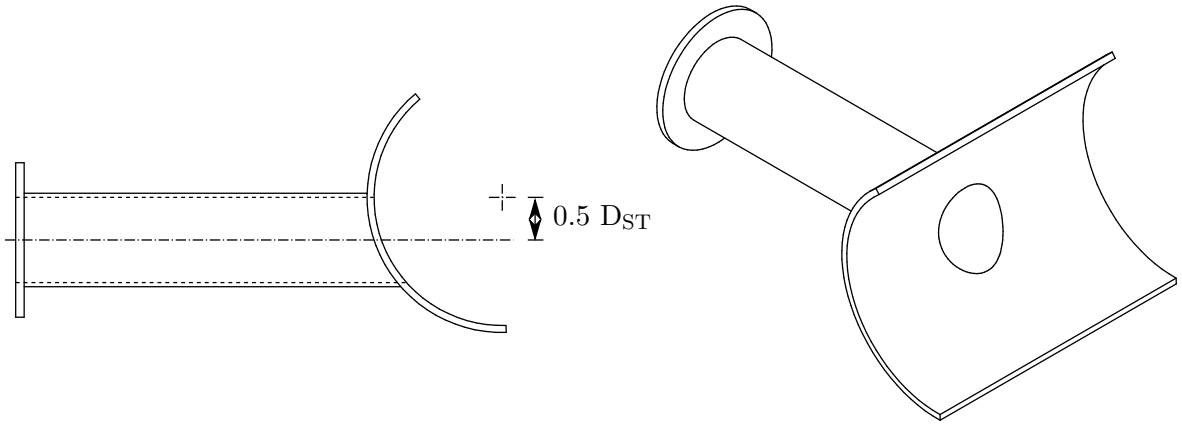


Figure 4.5: Radius ratio 3 (RR3) model with centreline of shock tube offset from exit cylinder centre by 0.5 D_{ST} (Elevation (*left*) and isometric (*right*))

Since diffraction around the oblique exit of a cutoff tube would involve the additional characteristic length of the tube thickness, a plate was affixed to the tube which added a length no less than 2 tube diameters in all directions from the diffraction edge to remove this additional length scale. Once fitted, all plates were covered with an automotive putty to fill any gaps or notches in the surface which may disturb the shock wave travel and then sanded to a smooth finish. Once prepared, all models were painted matt black to prevent optical mirage in testing.

4.2.2 Flow produced by a conical shock wave

The general arrangement of the conical shock tube is as shown in Figure 4.6. This apparatus was originally developed for the study of these shock waves by Skews, Menon et al. (2002). The conical shock tube is vertically arranged with the test section near the floor for ease of installation of the flow visualisation system. The operating principle is the same as that of any other diaphragm-restrained shock tube in that a diaphragm is used to separate the driver gas from the driven gas until the required pressure ratio is achieved.

The diaphragm material used in these experiments was polyester film either 100 μm or 190 μm in thickness. This was used in combination to produce composite thicknesses ranging from 100 μm to 570 μm for diaphragm pressure ratios between 3.6 and 8.5 respectively. The diaphragm was mechanically ruptured once the required pressure ratio was achieved by a

pneumatically-driven bursting mechanism contained within the driver section.

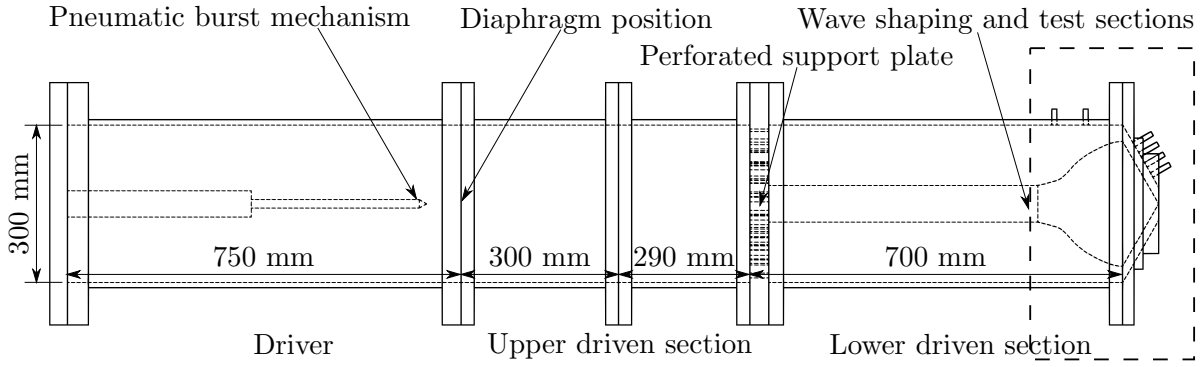


Figure 4.6: General arrangement of conical shock tube (top to the left)

The significant difference from conventional shock tubes is the placement of a perforated plate to which an axial support sting 70 mm in diameter for a shaped contraction is attached. The contraction consists of two portions: the upper portion which focuses the plane wave transmitted through the perforated plate into the contracting conical channel, and the lower portion which defines the conical channel and hence the shock wave. The upper portion of the contraction was designed iteratively using CFD to produce as plane a wave at the entrance to the conical channel as possible. As such, the profile is arbitrary though it was originally based on an inverted parabolic cup and circular fillet connecting the parabolic surface to the sting surface. The lower conical portion is matched by an outer conical section which creates a contracting conical gap approximately 20 mm high (measured normally from the inner to the outer cone surface) for a 50° cone.

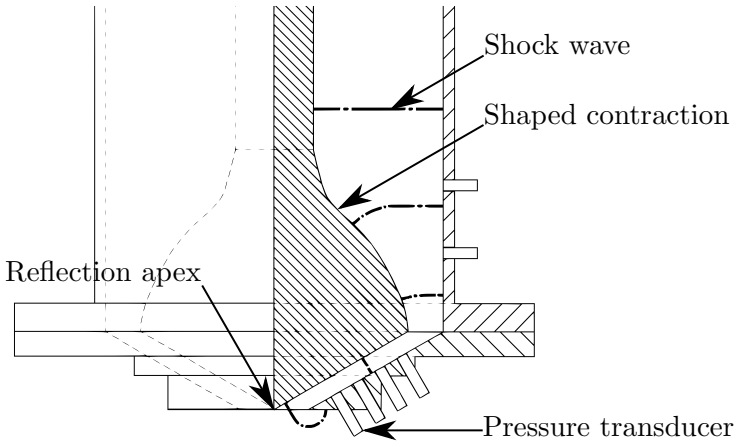


Figure 4.7: Detailed view of wave shaping and test sections of conical shock tube showing general change of wave shape

Given the issues identified with the breakdown of symmetry of axisymmetric waves near focus because of upstream disturbances, the contraction in the conical shock tube is suspended

from a perforated plate which is 36 mm thick with 49 evenly spaced holes 30 mm in diameter and distributes the upstream disturbances evenly over the incident plane wave and leaves the annular contraction channel free of all support struts which may produce perturbations. This turns the transmitted shock wave through a series of reflections into a collapsing conical shock wave as approximately illustrated in Figure 4.7. Since this arrangement allows the contraction to hang without support from the side walls of the tube, the shock wave produced is free of the instabilities noted by Takayama, Kleine and Grönig (1987). As such, the conical shock wave produced has a high level of stability approaching the reflection apex.

The initial plane shock Mach number for these pressure ratios ranged from 1.2 to 1.36. The experimental value of these Mach numbers were determined using high-frequency PCB Piezotronics pressure transducers mounted in the side wall of the lower driven section. The conical shock wave strength at the apex was estimated by extrapolation of the instantaneous Mach numbers measured using similar pressure transducers mounted in the outer conical plate. The signals from these lower transducers were also used to trigger the flow visualisation data acquisition system.

In addition to the basic setup as described above, occlusion plates were designed to block either some sector of the perforated plate or of the entrance to the conical channel. These were used to test the theory that azimuthal momentum deficit in the post-shock flow as a result of blockage of some part of the upstream channel results in dynamic curving of the central jetting produced by the conical shock wave reflection as discussed in § 5.1.4.2.

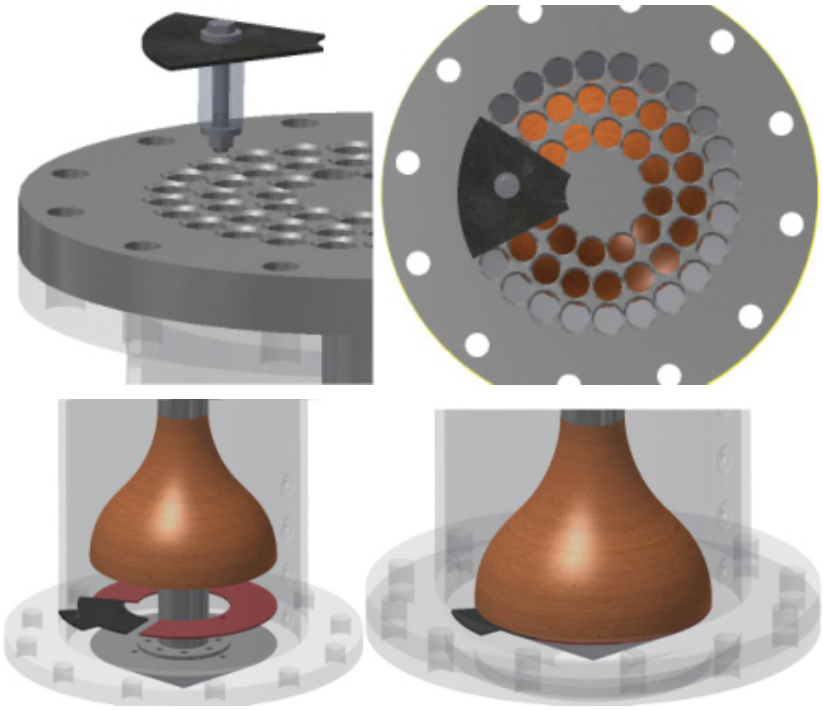


Figure 4.8: Schematic of the upper (*top*) and lower (*bottom*) occlusion plates

The upper occlusion plates were designed to cover holes on the perforated plate subtending sectors of 30°, 45°, and 60°. The lower occlusion plates made to subtend sectors of 10°, 20°, and 30° immediately before the conical contraction near the bottom of the apparatus. Here, the smaller angular ranges were used as it was assumed that the plates located closer to the exit of the tube would have a greater effect on the jet curvature due to lower diffusion. Due to limitations of the existing design, the lower occlusion plates were mounted on the opposite side of the tube to the upper occlusion plates. Schematics showing the installation of each of the upper and lower occlusion plates are given in Figure 4.8.

4.3 Flow Visualisation

The flow field in all cases was visualised using a standard z-type, two-mirror shadowgraph system of the sort described in Settles (2001). A specification of the apparatus used in the schlieren system is given in Appendix A. The illuminated field diameter was 406.4 mm (16") and images were captured using a Photron Fastcam SA5-775K operating at speeds of 50 000 or 75 000 frames per second (fps) with a resolution of 512 x 272 px or 320 x 264 px respectively, an approximate spatial resolution between 0.5 mm/px and 1 mm/px.

The field was illuminated using a conventional flash lamp triggered by a TTL signal derived from the pressure signals received from the high-frequency pressure transducers. Given the finite rise time for the illumination produced by the flash lamp, the camera was triggered slightly after the flash lamp to ensure full illumination during acquisition of the feature of interest. However, since the duration of the illumination period was around 1 ms, this meant that a visualisation of the entire flow field development was composited from several tests with staggered start times of acquisition.

Chapter 5 Results

5.1 Flow Produced by a Conical Shock Wave

5.1.1 Estimation of apex Mach number

The tests conducted on the conical shock tube were categorised by the driver pressure at rupture of the diaphragm. However, for better understanding of the flow fields observed the Mach number of the conical shock wave at the apex of the inner cone was estimated based on pressure transducer data. If the transducers fitted into the outer cone were labelled from 1 to 4 from the outermost to innermost, the average Mach number between each pair was first calculated from the pressure transducer data i.e. $M_{1\text{-}2}$, $M_{2\text{-}3}$, and $M_{3\text{-}4}$. These were assumed to be the instantaneous Mach number of the conical shock wave at the mid-point between each pair of transducers. These locations were projected normal to the outer cone surface onto the inner cone as it was assumed that the shock wave is normal to both the inner and outer cones. A quadratic extrapolation of the Mach number at the apex was then calculated. A quadratic extrapolation was used since an exponential extrapolation gave unreasonably high values for the apex Mach number.

5.1.2 Reflection behaviour

Tests were conducted for driver gauge pressures of 2, 4, 6 and 8 bar. Time evolutions of the shock behaviour are given in Figures 5.1 and 5.2 for pressures of 2 and 8 bar respectively. These cases correspond to approximate Mach numbers at the apex (M_{Apex}) of the inner cone of 1.11 and 2.30 respectively. The approximate time since the incidence of the wave at the axis is shown in each image. The shock wave is generally referred to as conical although only the section near the axis is truly conical at exit due to the diffraction of the outer edge of the shock wave. In all of these images there is a vortex induced by the diffraction of the imploding shock wave over the lip of the outer cone, not to be confused with the vortex present in the V-type reflection (Hornung 2000). At early times this diffracted shock wave

and induced vortex obscure the focusing behaviour of the section of the shock wave in contact with the inner cone or reflecting at the axis of the system. For this reason only images from later times are presented from the experimental series. Although several tests per apex Mach number were executed for each cone angle, the presented data were selected for clarity of images and the highest level of symmetry of the presented flow field (more on experimental asymmetry in § 5.1.4.2). However, the main features identified were present in all tests.

In Figure 5.1, at early times the reflection pattern may be of type S as identified in Hornung but from frame b) the curvature of the Mach disc is quite evident. The Mach disc grows in radius as the wave expands outwards until eventually the wave front resembles a single hemispherical wave. The vortex behind the Mach disc is evident in these frames, making this a V-type reflection. In the last frames the shear layer emerging from the triple point of the Mach reflection is entrained in this vortex.

Initially the curved reflected wave is smooth but undergoes a typical shock-vortex interaction with the diffraction vortex although, atypically, the portion between the exit plane and core of the diffraction vortex appears to steepen at early times.

The case of the much stronger wave with M_{Apex} of 2.30 in Figure 5.2 is very similar. However, preceding the interaction of the reflected wave with the diffraction vortex, a shocklet develops on the inner upstream side of the vortex due the very high induced velocities caused by the vortex flow and the jetting of the flow along the axis caused by the Mach reflection there. This shocklet is evident from frame a) in this series and merges with the steepened reflected wave so that only one wave is evident in the final frame.

The Mach disc appears curved from frame a) suggesting that, if it does occur, the S-type reflection does not persist for strong driver pressures and steep cone angles. The induced vortex behind the curved Mach disc is visible, as is the entrained shear layer from the primary triple point. In frame e) the second bulge of the Mach disc caused by the induced flow through the centre of the vortex is clearly visible. The second triple point of the DS-type reflection can be distinguished though the reflected wave. The resulting shear layer is indistinguishable from the boundary of the vortex plume, although part may be seen to the right of the vortex in frame e).

Also of note is that the Mach disc vortex is closer to the Mach disc itself for higher apex Mach numbers than for lower ones. For example, the vortex is approximately one vortex diameter upstream of the Mach disc in the final frame of Figure 5.1 for M_{Apex} of 1.11 while the vortex for M_{Apex} of 2.30 in Figure 5.2 is less than half of the vortex diameter upstream of the Mach disc.

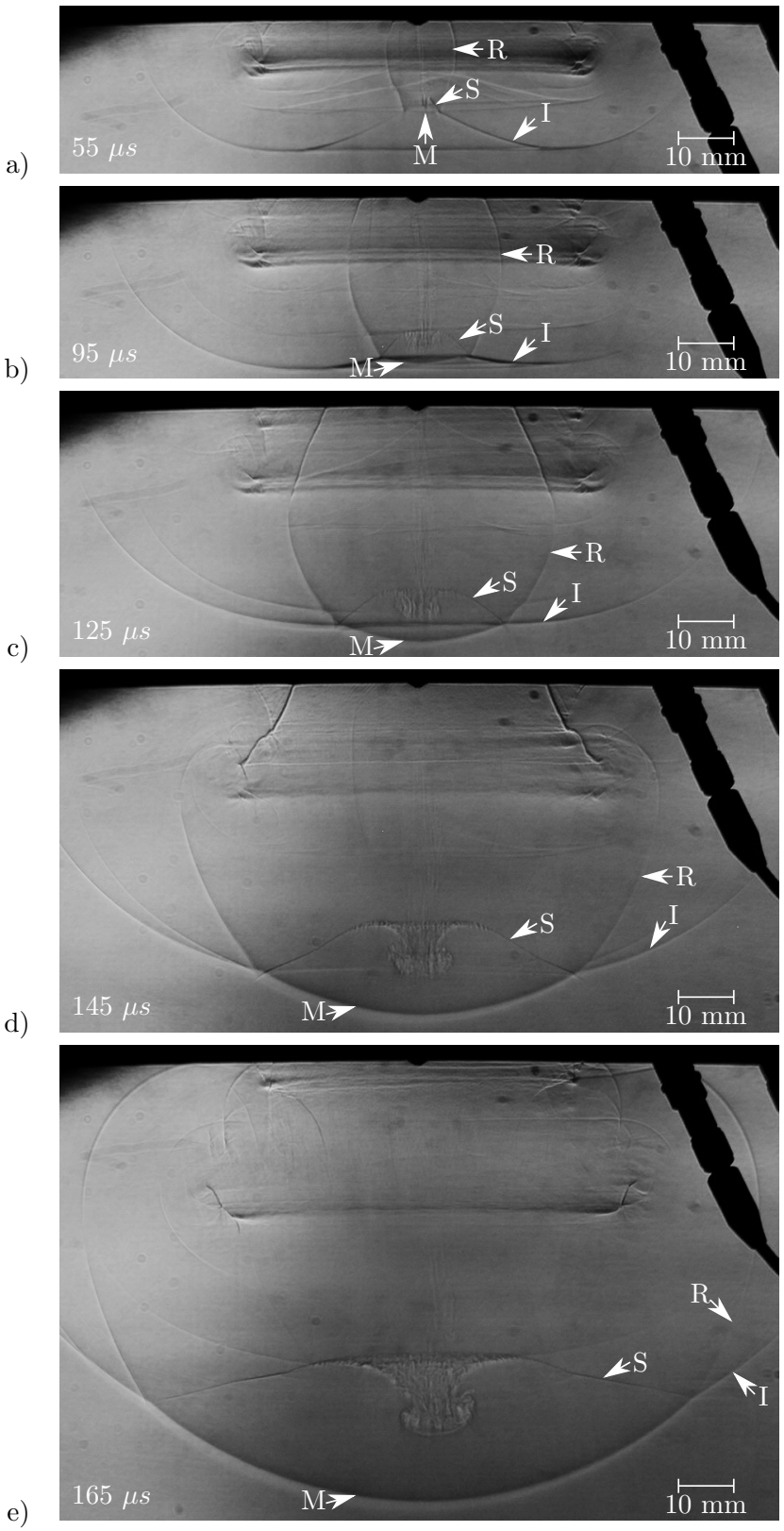


Figure 5.1: Evolution of the flow from a conical gap with apex Mach number of 1.11 and a 60° cone half-angle (*I - incident wave, R - reflected wave, M - Mach disc, S - primary shear layer, TP2 - second triple point*)

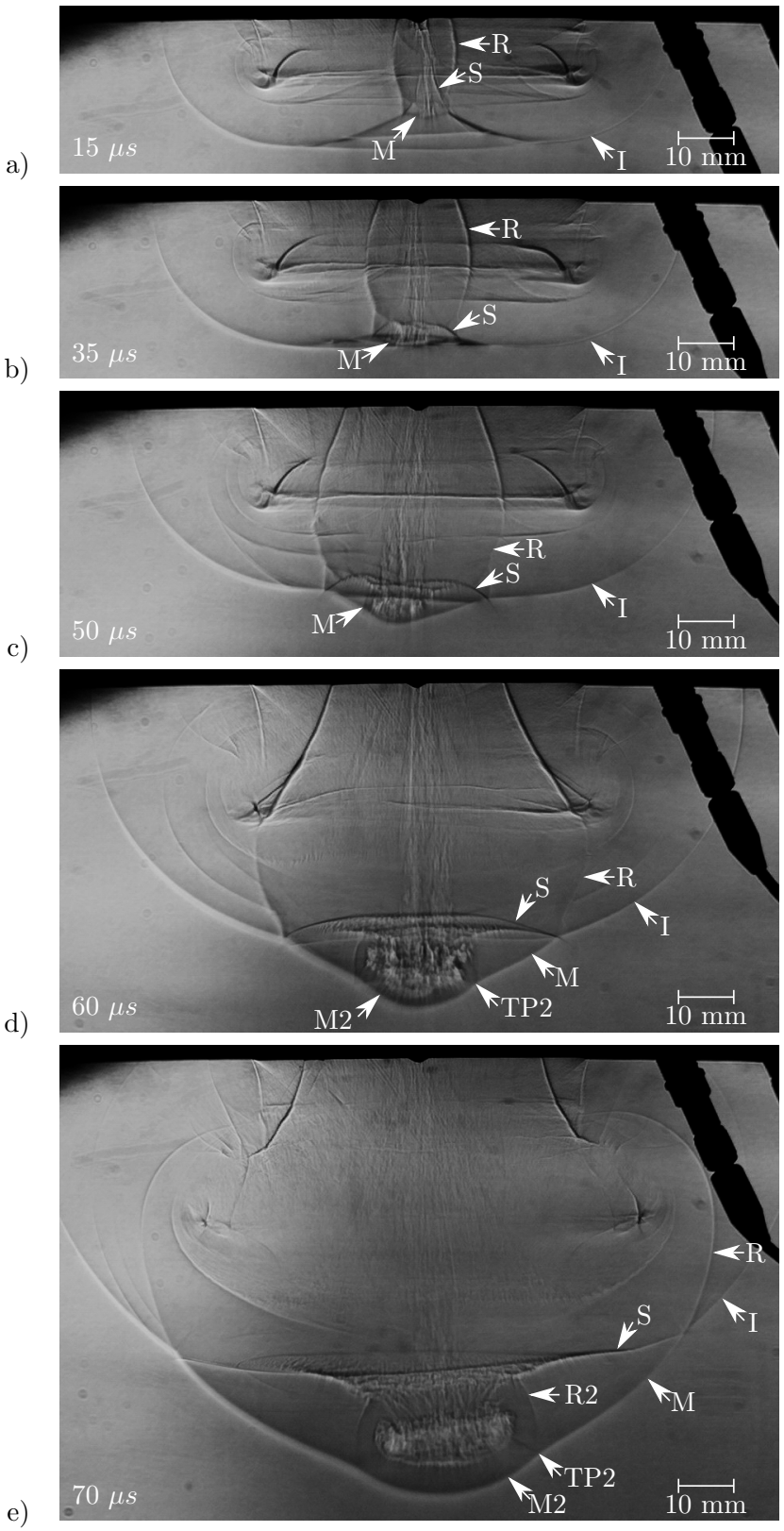


Figure 5.2: Evolution of the flow from a conical gap with apex Mach number of 2.30 and a 60° cone half-angle (*I - incident wave, R - reflected wave, M - Mach disc, S - primary shear layer, TP2 - second triple point*)

5.1.3 Computational Fluid Dynamics

The experimental apparatus was modelled using the commercial code Fluent 12.0 using a truncated axisymmetric domain, where the inlet was located halfway between the perforated plate and exit plane as a point at which the wave transmitted through the perforated plate was expected to be stabilised to a plane wave. The flow properties on this inlet were set using the properties of the plane shock wave Mach number measured experimentally in the lower driven section before the contraction. The outlet boundaries in the exit region were set to a pressure of 83 300 Pa (the ambient condition in the laboratory) and temperature of 294 K. An Euler solver was used for a mesh divided into several blocks to allow for the best mesh quality in each and an expansion region downstream of the exit 200 mm long and 200 mm in radius.

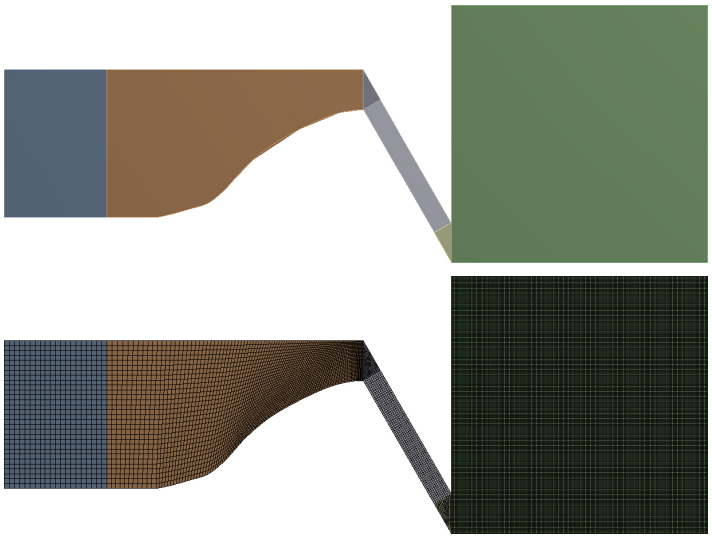


Figure 5.3: CFD geometry (*top*) and mesh (*bottom*) for conical shock tube model

Following a simple mesh independence study, the domain was meshed with a quadrilateral-dominant scheme with cells ranging in size from 3 mm in the inlet region to 1 mm at the exit as shown in Figure 5.3. The cells were set to be uniform where possible but some distortion was inevitable especially in the upper contraction region. The resultant initial meshes contained between 45 000 and 55 000 cells depending on the cone angle with mean element quality of 0.96, where the element quality is a composite quality metric which compares the cell aspect ratio and skewness to a regular element i.e. a square or equilateral triangle for quadrilateral and triangular cells respectively.

The model was processed using the axisymmetric, single-precision Fluent solver for density-based equations. Due to time and resource limitations, all models were solved using an inviscid solver with a Courant-Friedrichs-Levy factor of 2 and constant time stepping of 1 μs. An

implicit Roe-FDS scheme was used for linearisation and second-order upwind schemes were used for spatial discretisation. Adaptive mesh refinement based on the normalised gradients of density and Mach number was used to refine the mesh every 10 μs. Models were calculated for 2 000 μs. The inlet shock wave Mach numbers considered were 1.10, 1.23, 1.27, and 1.36 based on the specified driver pressures of 2, 4, 6, and 8 bar respectively. The simulations were executed on an Intel Core i7-3770 processor with 4GB of RAM.

5.1.3.1 Effect of driver pressure

The series presented in Figures 5.4 and 5.5 show the evolution of the wave from the computational model from the initial incidence of the converging wave on the axis, taken as a time of 0 μs. All images have been reflected about the axis of symmetry, indicated by a white line down the centre of each image, to be directly comparable with the experimental data.

The curvature of the outer portion of the wave and vortex produced by the diffraction over the outer lip are clearly evident in frames a) of each series. While the Mach disc in the frame b) of Figure 5.4 appears quite flat and is hence possibly an S-type reflection, the Mach disc in the frame b) of Figure 5.5 is curved, characteristic of the V-type reflection. This suggests that the S-type reflection may occur for all incident wave strengths but is obscured by the diffraction vortex experimentally and can only be clearly seen numerically. It also suggests that S-type reflection may occur for all incident wave strengths but quickly transitions into a V-type reflection. [Note that from this frame of the series there is a black region in the centre of the high velocity magnitude region immediately behind the Mach disc. This represents a region of velocity magnitude greater than 500 ms^{-1} which was clipped in limiting the display range.]

While for M_{Apex} of 1.11 the Mach disc remains smooth and the V-type reflection persists, for M_{Apex} of 2.30 V-type reflection quickly develops and then becomes DV-type reflection. The greater strength of the jetting from the initial reflection and of the Mach disc vortex resulting from the higher driver pressure induce much higher velocities behind the primary front than the 2 bar case resulting in the second Mach disc forming in the primary wave. As with the experimental images, the reflected wave is only vaguely distinguishable here and the shear layer of the second triple point is indistinguishable from the vortex plume.

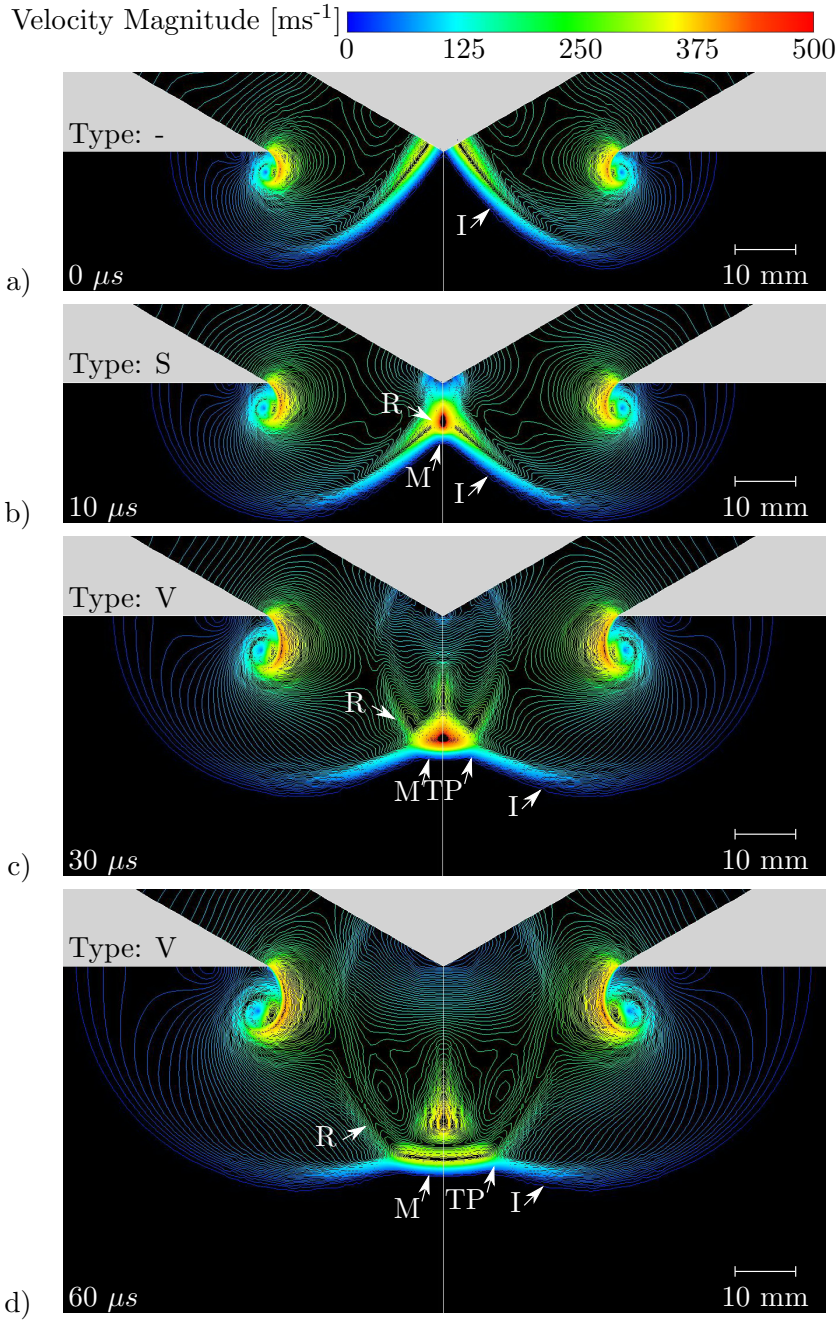


Figure 5.4: Velocity magnitude contours ($V \in [0, 500] m.s^{-1}$) for M_{Apex} of 1.11 and 60° cone half-angle showing the diffraction of the emerging shock, and the development of the triple points on the primary wave (*I - incident wave, R - reflected wave, M - Mach disc, TP - triple point*)

5.1.3.2 Effect of cone angle

A brief study was also made of the effect of changes in the cone half-angle on the initial reflection behaviour and the evolution of these features with time. In the limit where the

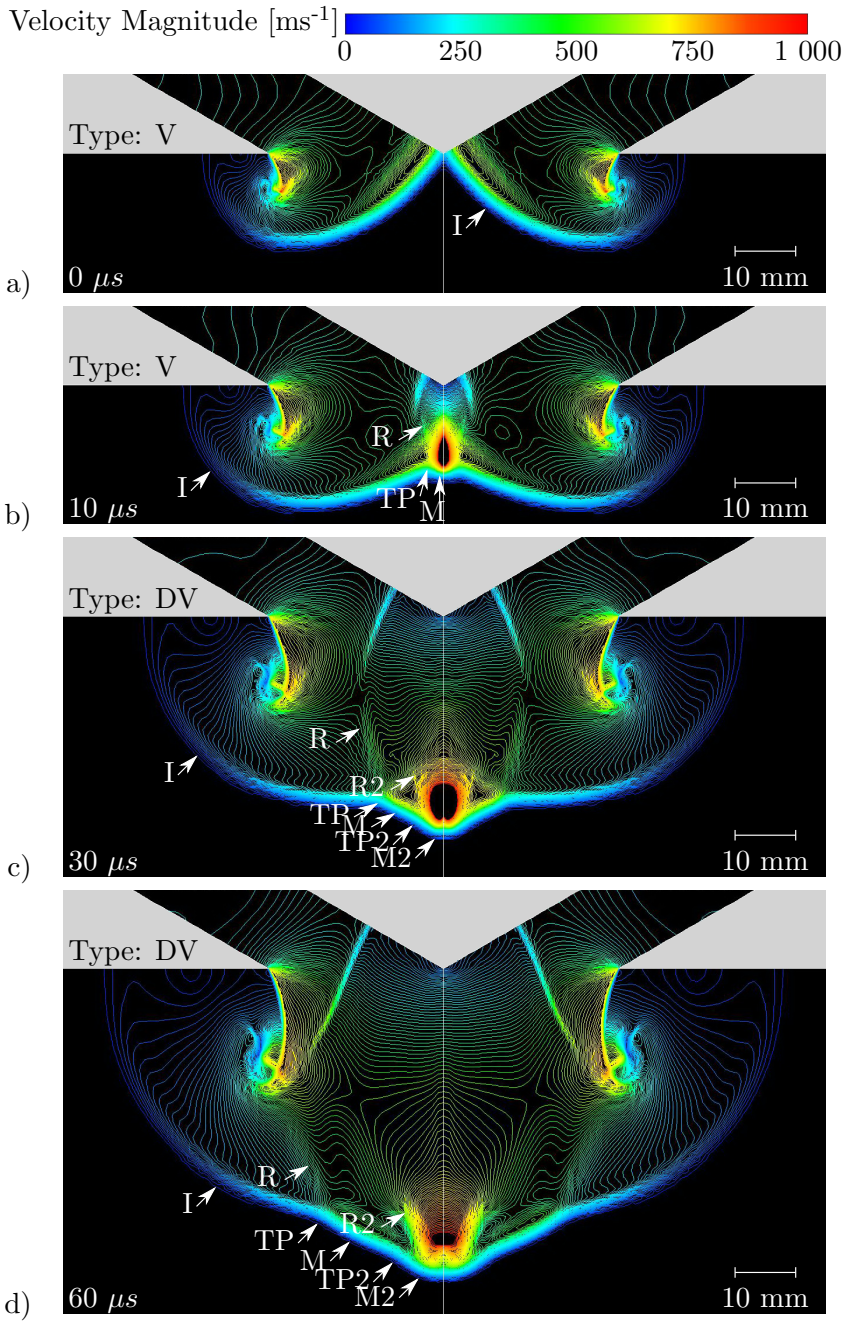


Figure 5.5: Velocity magnitude contours ($V \in [0, 1000] m.s^{-1}$) for M_{Apex} of 2.30 and 60° cone half-angle showing the diffraction of the emerging shock, and the development of the triple points on the primary wave (*I - incident wave, R - reflected wave, M - Mach disc, TP2 - second triple point*)

cone half-angle is 90°, the imploding conical shock wave is represented by the imploding cylindrical shock wave. This phenomenon has been studied, both experimentally (Takayama, Kleine and Grönig 1987) and analytically (Mölder et al. 1997), extensively in the past.

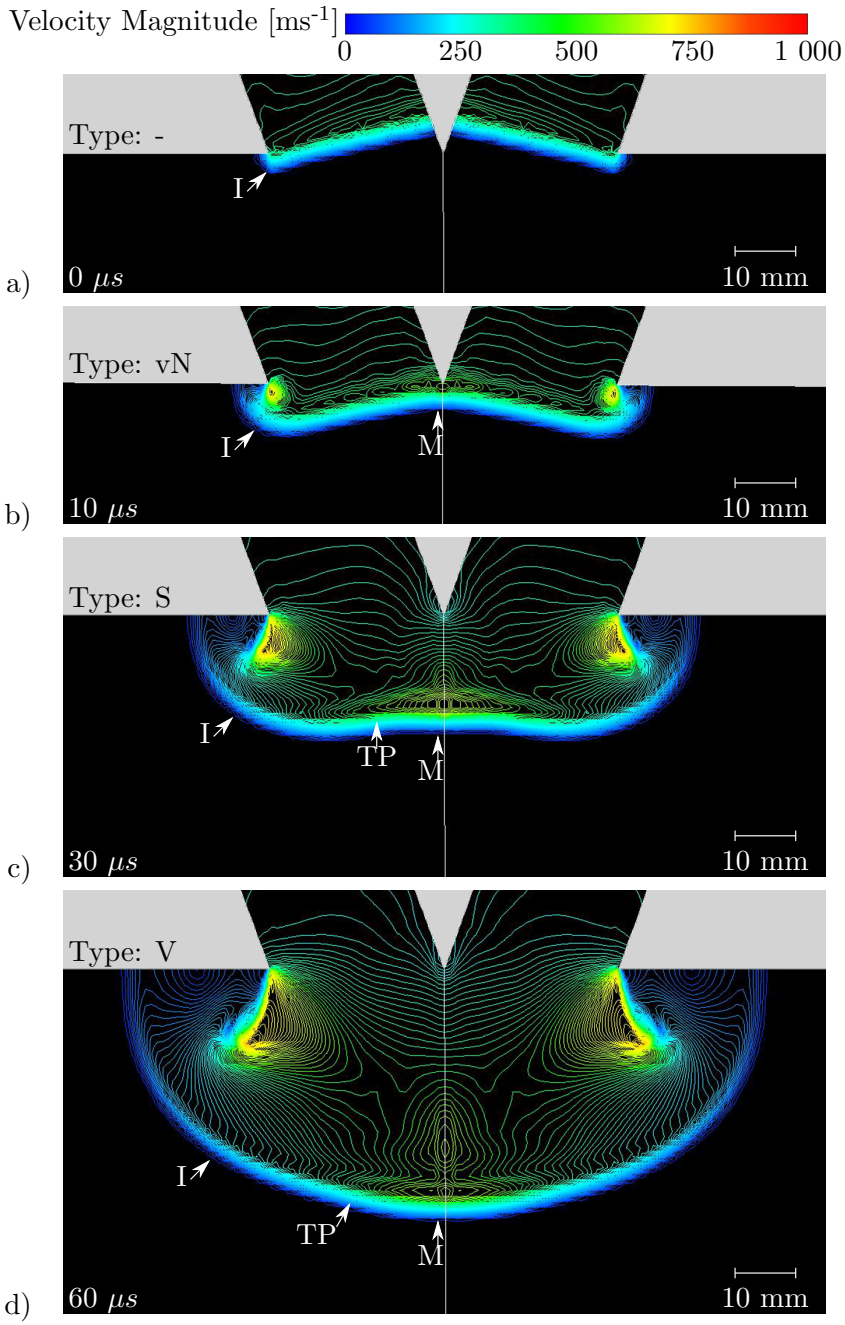


Figure 5.6: Velocity magnitude contours ($V \in [0, 1000] m.s^{-1}$) for M_{Apex} of 2.30 and 20° cone half-angle showing the diffraction of the emerging shock, and the development of the triple points on the primary wave (*I - incident wave, M - Mach disc, TP - triple point*)

In the other limit, a cone half-angle of 0°, the reflection behaviour could be thought of as a shock wave propagating along the axis of a straight wire of infinitesimal thickness i.e. the unperturbed propagation of a plane wave. This analogy suggests that there must be a lower limit of the cone half-angle at which the reflected wave formed at the axis becomes negligibly weak. To explore this trend, cone half-angles of 20° and 30° with an apex Mach number of 2.30 were modelled using CFD. These angles were selected with a view toward further

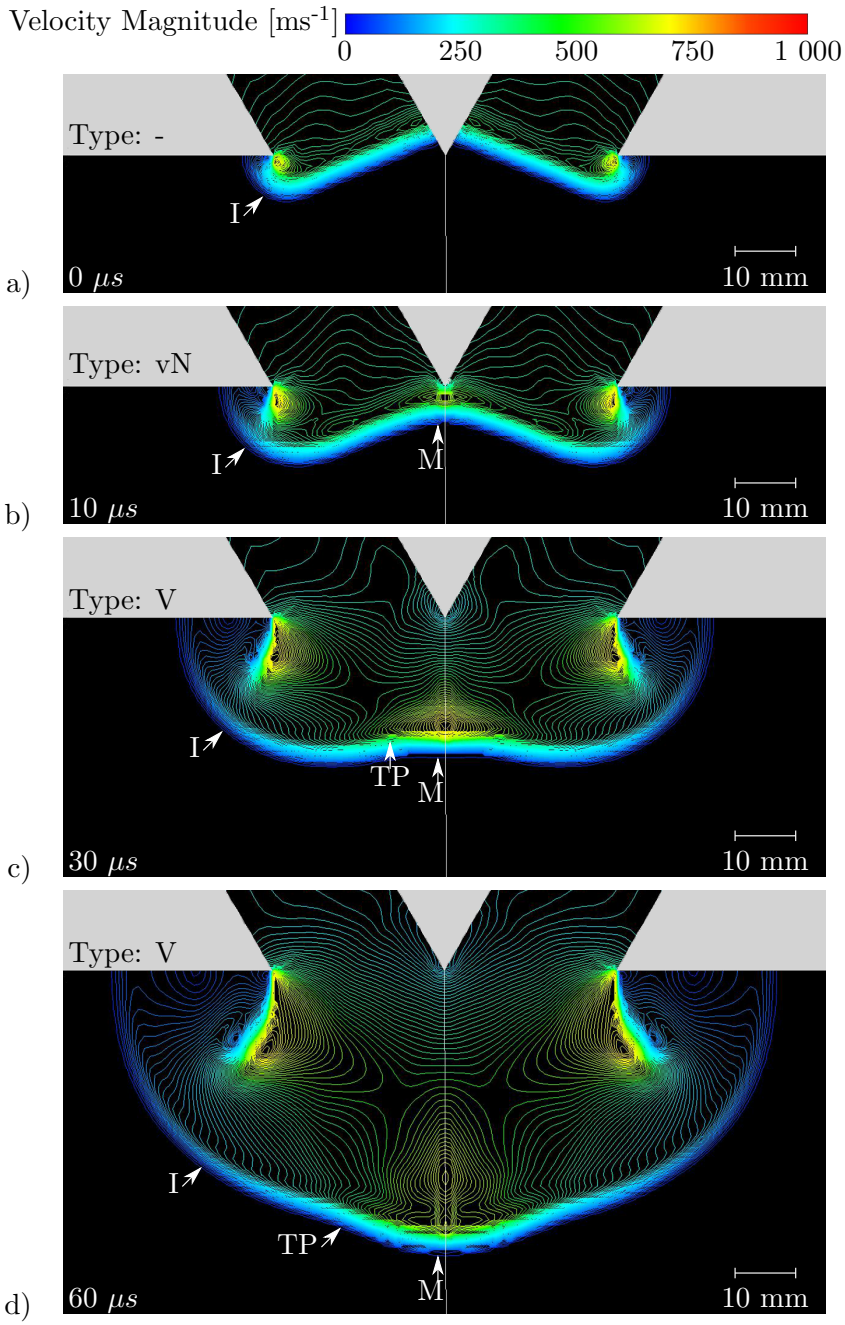


Figure 5.7: Velocity magnitude contours ($V \in [0, 1000] m.s^{-1}$) for M_{Apex} of 2.30 and 30° cone half-angle showing the diffraction of the emerging shock, and the development of the triple points on the primary wave (*I - incident wave, M - Mach disc, TP - triple point*)

experimentation though this proved to be impossible with the current installation of the apparatus due to height constraints.

For direct comparison, the same progression in time as used for the driver pressure comparison has been used. In these cases the first frame was taken as close to the initial incidence at the apex as possible, though the offset has been estimated as approximately 4 μs.

In both cases the initial reflection at the axis differs from that in Figure 5.5 in that the Mach disc and incident wave appear to be almost continuous in slope and there is little or no indication of a reflected wave, i.e. a very weak irregular reflection. Due to the similarity to the von Neumann reflection of plane waves, this will henceforth be called vN-type reflection. It is notable that the reflexed curvature of the incident wave-Mach disc surface in the 30° case (Figure 5.7, frame b)) is significantly higher than that in the 20° case (Figure 5.6, frame b)) due to the higher incidence angle of the incident wave while there remains little evidence of a reflected wave.

In Figure 5.6 30 μs after the start of reflection the Mach disc appears plane, suggesting an S-type reflection, and by 60 μs after the start of reflection the Mach stem is curved and appears almost continuous in slope with the diffracted incident wave as is typical for this system at later times. The curved Mach disc at these later times also suggests a V-type reflection following the typical progression from S-type to V-type.

By comparison, the Mach disc 30 μs after the start of reflection in the 30° case (Figure 5.7, frame c)) is slightly convex and the increased velocity directly behind it is quite clear, confirming that this is a V-type reflection, albeit a weak one judging by the induced curvature of the Mach disc. Thus, as with the higher incident angle cases for high apex Mach numbers, it would seem that the S-type reflection is short-lived and quickly transitions to V-type. However, unlike the higher angle cases, the DV-type reflection is not formed due to the weaker jetting as a result of the smaller turn angle required for the axial flow i.e. the flow is more similar to that behind a plane wave.

5.1.4 Other flow features

5.1.4.1 Conical Kelvin-Helmholtz instability

In some tests at lower apex Mach number it was noted that the shear layer emerging from the primary triple point shows signs of instability as shown in Figure 5.8. This instability shows the patterned lighter and darker regions which typically indicate the presence of the KHI. The smaller scale and three-dimensional shape of this shear layer made it difficult to accurately resolve this using the visualisation methods employed. Also, it was not very repeatable experimentally. Since this was the first instance identified of the KHI in an axisymmetric flow field, an additional experimental campaign was undertaken to specifically identify the nature of the instability of the shear layer.

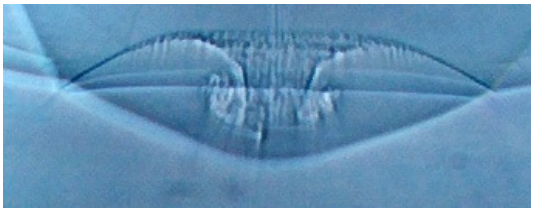


Figure 5.8: Possible Kelvin-Helmholtz instability of the primary shear layer for 60° cone at M_{Apex} of 1.11

The extended test campaign considered all except the highest apex Mach Numbers possible on the apparatus (due to safety restrictions) and only tests in which the flow was well centred on the axis of the apparatus were considered (see § 5.1.4.2 for more on this distinction).

The description of the basic flow field will be based on the images for the M_{Apex} of 1.11 flow in the left of Figure 5.9. In frame a) the shear layer can be seen extending between the triple points (one marked as TP in the figure) of the Mach reflection and the vortex ring toward the centre of the frame. While there are other vortex rings shed from the outer diffraction lip at later times for most of the Mach numbers, the vortex ring of interest here is the first one caused by the axial jet formed when the shock wave first reflects at the cone apex.

It should be noted that the shape seen here of the line connecting the tangent edges of the shear layer defines a concave cone where the outer edges of the cone are at the same level as the protruding portion closer to the centre line. The angle between the incident, reflected, and Mach stem waves is already quite shallow at this time. While some striations are visible in the shear layer near the centreline, the tangent edge of the shear layer still appears smooth.

In frame b), there is noticeable striation of the tangent edge of the shear layer suggesting a KHI. The shear layer is still a concave cone but the entire cone now appears to extend away from the plane of the base defined by the outer edge and the curvature is noticeably lower than at earlier times.

In the third image the outer edge region of the shear layer is becoming indiscernible and the inner section seems to be approximately a plane cone. There is noticeable striation of the tangent edges of the shear layer and the striations running through the centre of the image seem to link dark points in each of the tangent edges, suggesting that a Kelvin-Helmholtz instability has indeed formed as a series of vortex loops.

In the final image the shear layer is now a convex cone conforming to the shape of the central plume resulting from the flow toward the cone apex. While the portions closest to the centre line of the shear layer no longer show much evidence of KHI, likely as a result of the vortex ring below it out of frame, the middle portion still shows indications of the instability though

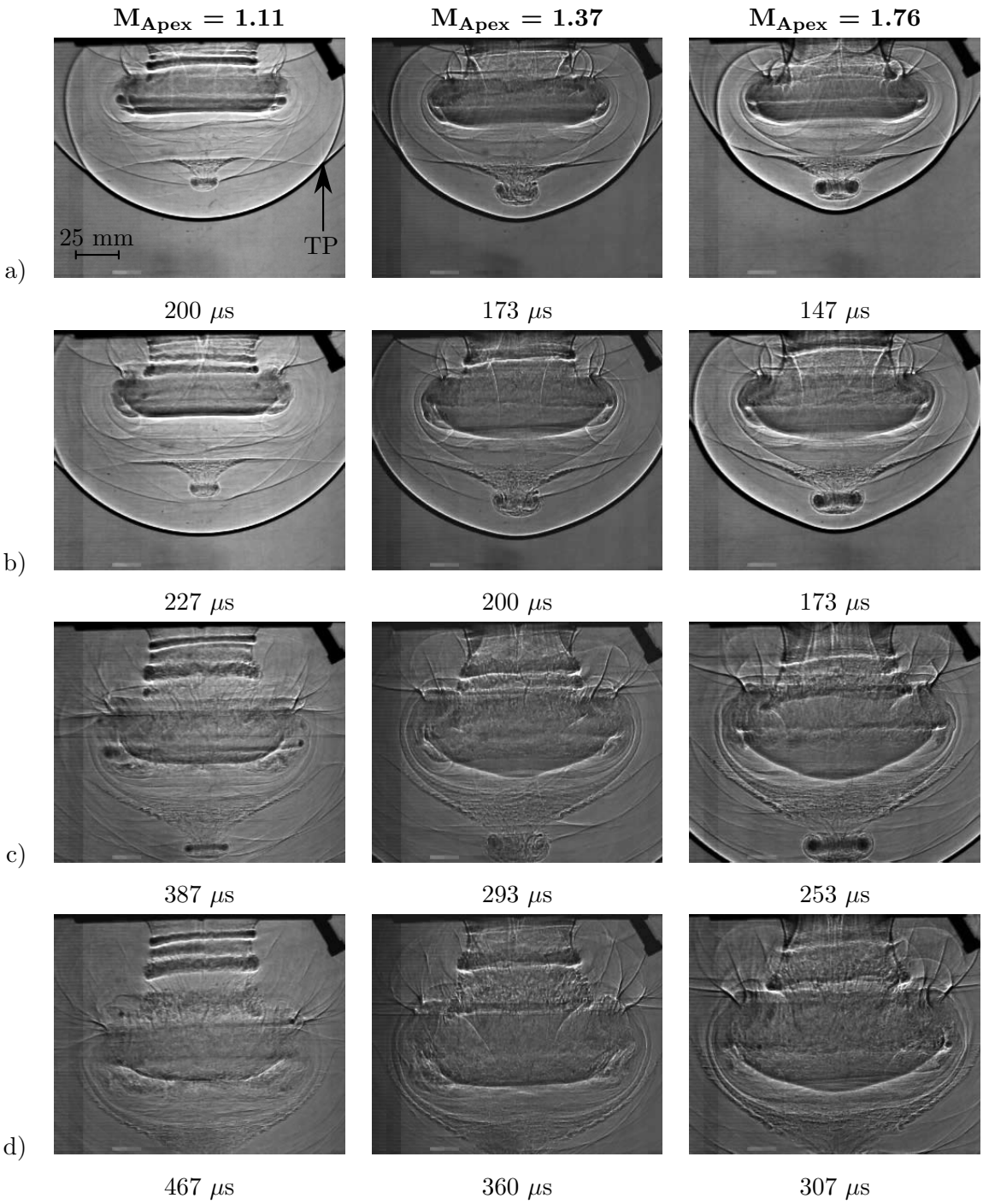


Figure 5.9: Shadowgraphs of the flow field for M_{Apex} of 1.11 (*left*), 1.37 (*centre*), and 1.76 (*right*) bar driver pressures when: the shear layer is first clearly visible (*top*); the tip of the shear layer reaches the edge of the frame (*top-middle*); the central vortex reaches the edge of the frame (*bottom-middle*); and the shear layer conforms to the central plume (*bottom*). Times given are the approximate time since the first arrival of the incident shock wave at the cone apex

the striations linking dark nodes in the tangent edges are difficult to discern through the distortions of the central plume.

There are two notable differences in the behaviour as the Mach number increases: the Kelvin-Helmholtz instability is visible at earlier times and the shear layer cone is less concave initially. The first aspect is evident in the first images of the flows for the M_{Apex} of 1.37 and 1.76 flows respectively where the amplitude of the perturbation of the shear layer by the KHI is noticeably larger for the higher Mach number suggesting that the instability has been present longer.

The change in curvature of the shear layer surface can be attributed to the higher convection speed of the axial flow for the higher initial Mach number since the central portion of the shear layer is entrained in the axial vortex ring. It can also be seen in the early images that the shock wave for the higher Mach numbers has greater curvature than for the lower Mach numbers and so the vertical distance travelled by the Mach disc is less and hence a steeper shear layer cone geometrically. There is also a noticeable discontinuity in the slope of the shear layer in the first frame of the M_{Apex} of 1.76 data though the cause of this is not immediately apparent.

In order to better compare the results for the different driver pressures, the images presented in Figure 5.9 were cropped and arranged to show the growth in time and also to compare with the analogous plane KHI from Rubidge, Skews et al. (2015) for the incident plane shock wave Mach number closest to the apex Mach number. This comparison is shown in Figure 5.10.

Regardless of initial shock wave strength, the KHI only appears in the conical case when the conical shear layer most resembles a right cone. At times where the shear layer is significantly curved no KHI is evident. The curvature of the shear layer at these times would serve to further compress the slower flow exiting the Mach disc than that exiting the reflected wave i.e. the slower flow below the shear layer. Similarly the faster flow above the shear layer may be accelerated by expansion over the curved shear layer. Since this would increase the convective Mach number, it would serve to stabilise the shear layer and thus prevent the transition to KHI as originally proposed by Papamoschou and Roshko (1988).

Another factor contributing to the KHI only being evident on the inboard portion the shear layer is that as the reflection develops in time, the outboard portions of the shear layer are produced by waves of decreasing strength as they expand approximately spherically in space. The result is that the lower flow speeds on either side of the shear layer would reduce the absolute shear and thus the shear layer itself would be more stable.

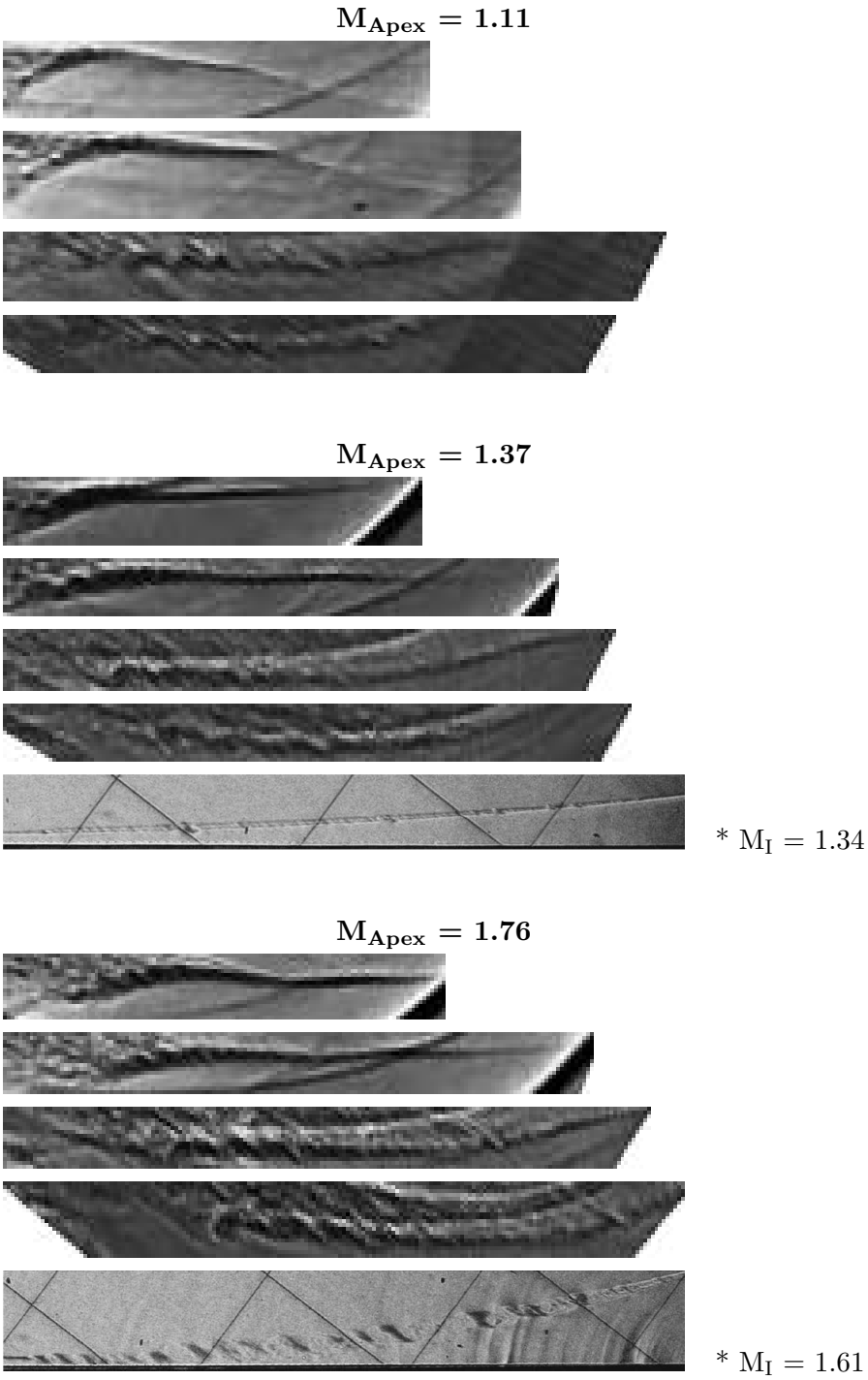


Figure 5.10: Detailed view of the development of the Kelvin-Helmholtz instability along the tangent edge of the shear layer (axis to the left) as well as a comparison of the developed instability for the nearest Mach number for the plane wedge case in Rubidge, Skews et al. (2015) (marked by *)

The clearest evidence that the deformation of the conical shear layer is a Kelvin-Helmholtz instability (KHI) is the characteristic braided appearance of the shear layer in the latest image of the M_{Apex} of 1.76 results. Unlike the two-dimensional KHI, the vortices formed in

the shear layer would by necessity be vortex rings rather than straight vortex lines. It would be advantageous to use a visualisation system that could only illuminate a plane passing through the axis but unfortunately no such system could be implemented which produced results suitable for inclusion here. Thus the vortex rings passing between the far edges of the shear layer cone could cause general darkening rather than striation of the central region.

Computational Fluid Dynamics would be a logical choice to confirm the existence of the conical KHI. However, as noted when attempted by Rubidge and Skews (2014), Reynolds-averaged Navier-Stokes (RANS) simulation of transient Mach reflections resolves the reflection geometry and shear layer but the instability does not develop or presents weakly because of the dampening of vorticity by most such models in commercial CFD packages such as the one used here. Rather, as noted in Rubidge, Skews et al. (2015), a custom solver would be needed instead. Since access to such a solver was not possible and deemed beyond the scope of this work, it is suggested that such a numerical investigation be undertaken in future.

5.1.4.2 Curved jetting

It was noted in some tests at higher pressure where the V-type reflection exists that the trajectory of the central jet and vortex plume was not straight along the axis but rather curved away from the axis. This followed from the trajectory of the shock front also being curved away from the axis. It was noted that this phenomenon only seemed to occur in instances where a large piece of the diaphragm had blown down onto the perforated support plate blocking several of the holes. It was theorised therefore that this behaviour was a result of the occlusion of the flow path and possibly as a result of a momentum deficit versus the remainder of the azimuthal range in the wake of the occlusion. As mentioned in § 4.2.2, occlusion plates fitted either to the perforated plate or the shaped contraction were used to test this theory.

The images in Figure 5.11 show typical results for these tests. The approximate trajectory of the jet has been highlighted by the transparent white line. Two points should be made about the resultant flow field:

As expected, the 30° lower occlusion appears to have approximately the same effect on the jet deflection as the 60° upper occlusion bearing out the theory that occlusions closer to the exit have a greater influence on the jet deflection due to the greater concentration of the low momentum region downstream.

More significant than this though is the fact that the jet deflection for the lower occlusion is toward the same side as for the upper occlusion. The deflection of the jet downstream of the

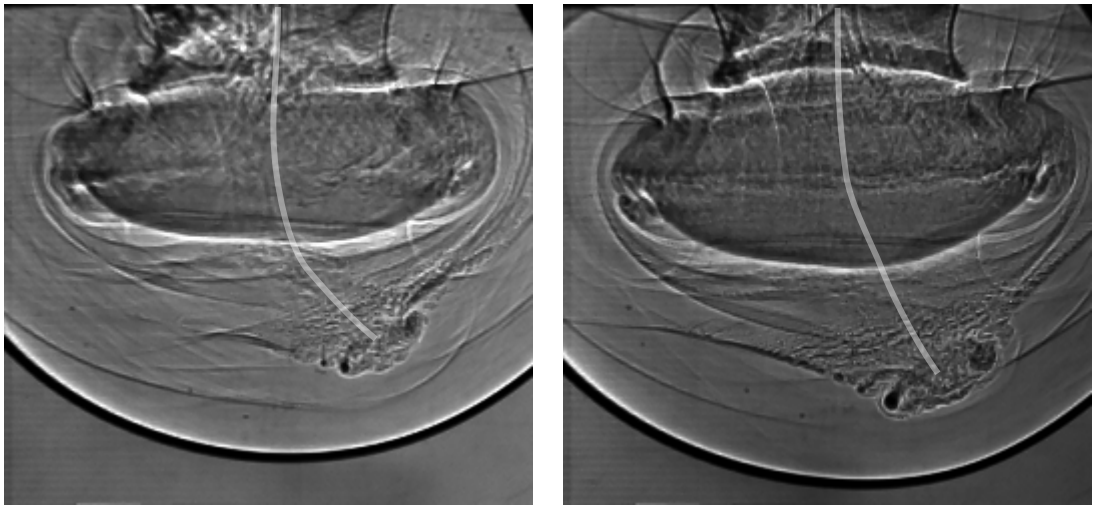


Figure 5.11: The deflection of the central jet for M_{Apex} of 1.76 with the 30° lower (*left*) and 60° upper (*right*) occlusion

lower occlusion is toward the side of the tube on which the occlusion is installed as would be expected if the deflection were simply a result of azimuthal momentum deficit. However, in the case of the upper occlusion, the curvature of the jet is away from the side of the tube on which the occlusion is installed. This suggests that the alignment of the planes of deflection for the two perturbation types may be a coincidence of the apparatus design and that the deflection of the jet is more likely as a result of the effect of the complex shock front shape entering the conical contraction as a result of the diffraction of the incident shock wave around the occlusion. A more detailed study using a range of geometries is warranted.

Of interest in the right image in Figure 5.11 is the pronounced braided appearance of the right portion of the shear layer with the roughly banded region connecting it to the left portion of the shear layer. This suggests that the conical Kelvin-Helmholtz instability (KHI), as discussed in § 5.1.4.1, may be present for more complex shear layer geometries than simply approximately right cones.

5.1.5 Summary

The configurations of conical shock wave reflection previously identified numerically were confirmed although no direct evidence of the S-type reflection could be found experimentally. This is because the high gradients in the diffracted portion of the conical shock wave in the particular apparatus used here obscured any S-type reflection that may have occurred. CFD modelling showed that S-type reflection may occur for a wide range of incident shock wave Mach numbers and cone angles but that it transitions almost immediately to V-type reflection and possibly later DV-type reflection.

A new reflection configuration, named the vN-type, was identified inn addition to the confirmation of the previously described reflection patterns for conical shock waves. The distinguishing characteristic of this type of conical shock wave reflection is that there is no reflected wave apparent following reflection similar to the weak reflection pattern for plane waves described by von Neumann.

Two additional flow features were identified: Kelvin-Helmholtz instability of the conical shear layer and curved jetting. The former is suggested by striation observed in the images of the shear layer starting in the triple point of the V-type reflection configuration and terminating in the vortex. Only a portion of the shear layer appears to be affected by the instability. Specifically, the variation in the convective Mach number of the shear layer as the flow field develops in time and the curvature of the shear layer both act as stabilising factors to inhibit the development of the KHI. This instability may be facility-dependant and triggered by the weak reflected waves trailing the incident shock wave as a result of the focusing into the conical channel and would thus require verification using bespoke, high-resolution CFD.

The curved jetting relates to the jet formed by the focusing of the flow at the conical apex and typically forming a jet aligned with the system axis. However, occlusions upstream of the focusing point allow for repeatable curvature of the jet. This is an unsteady jet and thus the final flow field will likely settle at late times into an axisymmetric flow. However, this finding suggests that a mechanism using partial occlusion of the upstream flow could be used to dynamically actuate steady jets.

5.2 Flow Produced by Diffraction of a Plane Shock Wave at the Inclined Exit of a Shock Tube

5.2.1 Experimental results

The development of the flow field for each of the Mach numbers tested for an exit plane inclined 30° to the tube normal is shown in Figure 5.12. The selected flow field stages shown are: when the diffracted shock wave reaches approximately 1 and 2 tube diameters downstream; and then when the vortex ring formed at the exit of the shock tube has convected approximately 1, 2, and 3 tube diameters (4") away from the exit plane. All measurements are taken along the level of the centreline of the tube and to either the front edge of the visible shock wave or the apparent centre of the thickness of the vortex. Where necessary, linear extrapolation is used to select the appropriate frame. The vortex ring is only partly visible when it has convected 3 tube diameters downstream because of the limits of the flow visualisation field of view.

5.2.1.1 The general nature of the diffraction

A primary difference between the canonical diffraction at the normal exit of a shock tube and the cases studied here is that the diffraction of the shock wave is not simultaneous at all azimuthal positions. Thus the vortex shed around the exit edge, if any, varies in 'age' with points farther upstream being more developed than those downstream. The angle of diffraction also changes from a very oblique one upstream to an acute one downstream and thus the strength of the expansion wave formed varies, especially after the horizontal centreline position where the diffraction angle reaches 90° and the subsequent acute diffractions decrease in strength (while diffractions greater than 90° are basically independent of angle as per Skews (1967a)).

The final feature of this change in diffraction behaviour is that the time taken for total diffraction (i.e. the time taken for the incident shock wave to travel along the length of the exit from its most upstream to most downstream edge) ranges from approximately 100 μs to 370 μs depending on exit angle and Mach number. Hence for higher exit angles and lower Mach numbers the shock wave diffracting at the downstream edge of the exit is often no longer plane and uniform in strength as it has been affected by the expansion waves originating at other parts of the diffracting edge.

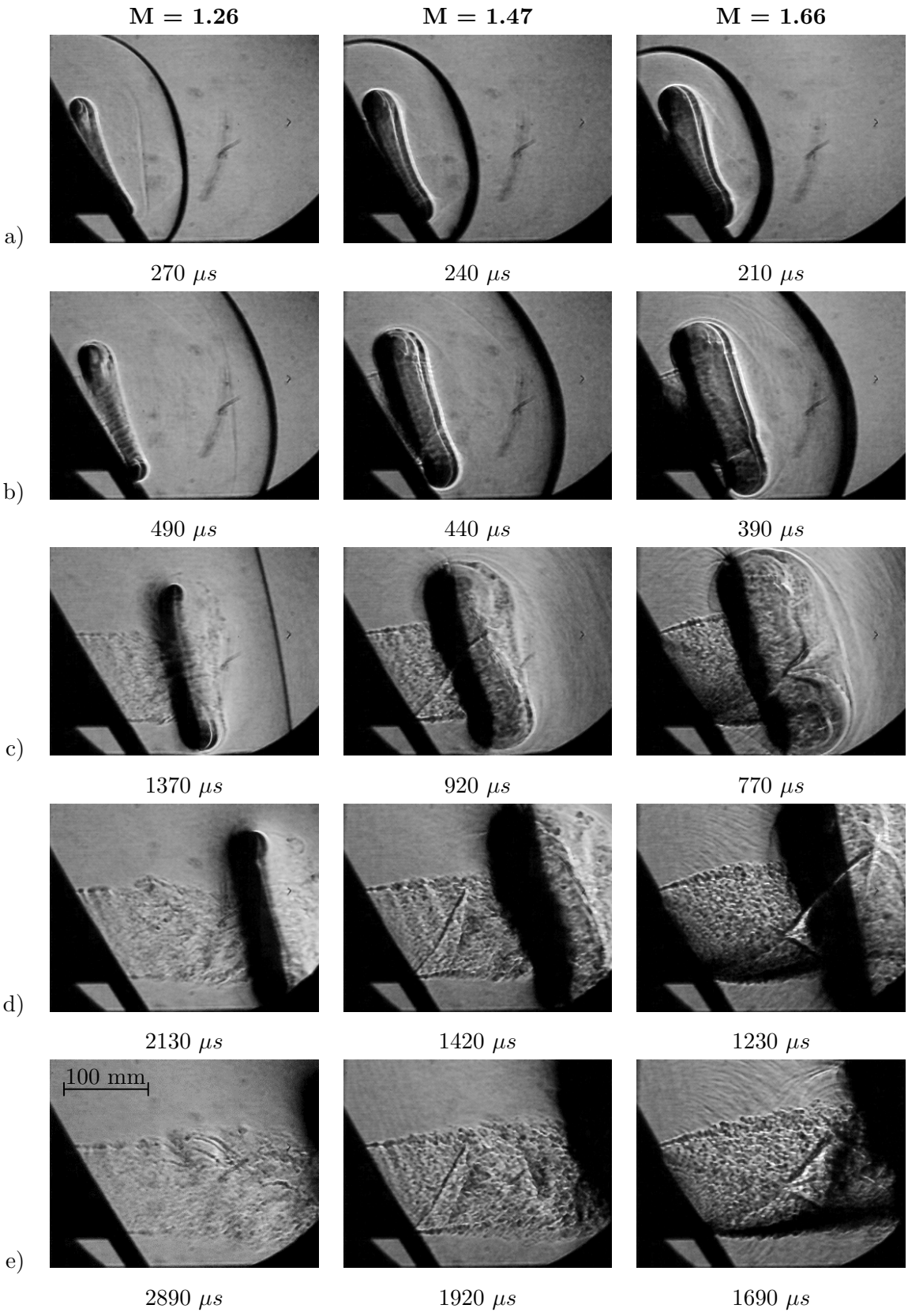


Figure 5.12: The flow field development for the exit of a shock tube inclined 30° to the normal for Mach numbers of 1.26, 1.47, and 1.66

5.2.1.2 Flow field development

In order that the description of the flow field given below is as clear as possible, annotated versions of selected frames from Figure 5.12 have been repeated in Figure 5.13.

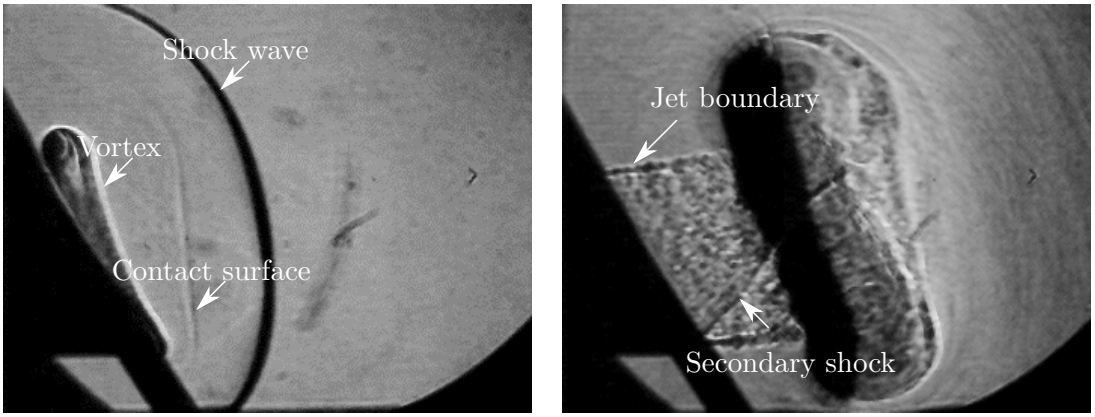


Figure 5.13: Annotated experimental images for the early (Mach 1.26 (*left*)) and later (Mach 1.47 (*right*)) flow field development

In Figure 5.12 frames a) the vortex produced by the initial diffraction of the shock wave is thicker at the upstream edge than at the downstream edge. This is a function both of the stronger diffraction at those azimuthal positions because of the greater local diffraction angle and the greater age of the local portion of the vortex. The contrast within the vortices also increases with Mach number suggesting greater density gradient and therefore higher velocity gradients, confirming the greater strength of the vortices. The stand-off distance of the upstream part of the vortex from the diffracting edge also increases with Mach number, confirming the greater induced velocity of this section and hence the greater velocity within that portion of the vortex.

Frames b) of Figure 5.12 show the position of the vortex when the axial portion of the shock wave is two tube diameters downstream of the centreline of the exit. It is clearly noticeable that the convection speed of the vortex increases significantly with Mach number, with the vortex produced by the Mach 1.66 incident wave having travelled approximately thrice the distance of that produced by the Mach 1.26 wave. It is also clear that the vortices shed by shock waves of higher incident strength are much thicker and entrain much more of the surrounding fluid. The embedded shock wave expected in the Mach 1.47 and Mach 1.66 cases, since the Mach number is higher than Mach 1.43 as suggested by Brouillette and Hébert (1997), is not clearly visible though the light line running through each of the vortices at the right side of each is probably the embedded shock wave. It should be noted that the

embedded shock wave may not yet entirely fill the aperture of the vortex loop as it may still be the initial toroidal shock wave visualised by Kleine et al. (2009).

Figure 5.12 frames c) show the flow fields for the different Mach numbers when the vortex has convected one tube diameter downstream. As expected, no embedded shock wave is present in the Mach 1.26 case. While the vortex ring appeared to be slightly curved forward in the previous frame, it is clear that the upper portion of the vortex is convecting downstream faster than the lower portion. This is evident from the decreasing longitudinal separation between the centres of the upper and lower portions of the vortex ring. Since the cross-section at an incline of the circular shock tube is elliptical, this is in line with the observations in both Kambe and Takao (1971) and Zare-Behtash, Kontis and Gongora-Orozco (2008) that regions with higher local curvature convect faster. That finding would suggest that the upper edge of the vortex, with high curvature, would convect faster than the centreline portion, with the lowest diffracting edge curvature. The vortex core also has a greater diameter at the upper portion than at the lower portion. Both of these are as a result of the stronger diffraction at the upper portion of the tube and greater local induced velocity of the vortex. This effect could also be because of the later diffraction at the downstream edge, though the vortex shed there has by this time detached from the diffracting edge meaning that the diffraction formation thereof is complete.

Another shock wave is noticeable in this frame for the Mach 1.26 case as well. Due to the arrangement of the optical system for the tests, the shock wave emanating from the shock tube will pass through the source leg of the Toepler-type arrangement of the schlieren system after passing through the test field. This is confirmed by the fact (better visible in the videos in Appendix B) that the passage of this shock wave does not affect the flow field in the test section at all, although the shock wave is distorted by the flow field density gradients indicating that it occurs 'uplight' (closer to the source in the optical path) of the test section. This would also explain the apparent greater speed of the shock wave as the source leg of the optical system is a diverging cone of light aimed at the first parabolic mirror. Since the light beam is smaller in diameter, the apparent speed of the wave in traversing it is greater than when traversing the beam passing through the test section. At very late times in the appended videos, the head of the jet plume can also be seen to arrive in the same location.

Figure 5.12 frames c) are the first time that jet can be clearly seen for the Mach 1.47 and Mach 1.66 cases and two features of the flow field are of note here. The more obvious feature of the jet is the asymmetric under-expansion whereby the upper portion of the jet bulges significantly farther away from the tube axis than the portion below the horizontal centreline. While the under-expansion of the jet is expected for the higher incident shock wave strengths, the nett effect of the asymmetrical under-expansion is that the jet is inclined upward away from the inclined surface. This is especially apparent in the Mach 1.66 case

where the top edge of the jet is inclined at approximately 15° upward while the lower edge is effectively parallel to the tube axis.

The second feature of note is the secondary waves visible within the jet originating near the exit surface, as marked in Figure 5.13 for the Mach 1.47 case, for example. This is related to the under-expansion of the jet since there will be expansion waves emanating from the diffraction edges. However, as covered in greater detail in § 5.3.2.2, the expansion wave here may meet part of the exit surface or even the interior of the shock tube unlike in the canonical case where it can only meet the free edge of the jet.

Consider the expansion wave formed at the upper diffraction edge (in the reference frame presented in the Figure) on the vertical plane of symmetry: if it were to meet the interior of the shock tube (a horizontal surface) at the lower side it would induce flow upward (toward the axis of the jet). Since this would violate the continuity of mass at that surface a compression fan or even a shock wave would have to form to induce the flow back parallel to the solid surface. If the expansion wave were to meet the inclined exit surface, the shock wave would form to induce the flow parallel to that surface. This description is based on an infinite-span, two-dimensional duct and thus, considering the fact that the shock tube is a cylindrical pipe, the expansion wave orientation and interaction will be much more complex here. Also, since the flow visualisation system can only visualise gradients in the plane normal to the optical axis, only the tangent edges of these secondary shock waves or compressions would be visible.

Therefore, considering the Mach 1.47 incident shock wave results, part of the strong expansion formed at the upstream diffraction edge must meet the interior of the shock tube at the lower surface. As explained, a shock wave forms to turn the flow back parallel to the wall of the pipe. Careful observation of frame d) of this series bears this out since the apparent foot of the secondary shock wave is inside of the shock tube. The tangent edge of the secondary shock wave is curved toward the jet boundary by the interaction with the expansion fan and then meets the jet boundary where it seems to undergo weak reflection or simply termination in the turbulent flow there.

Similarly, there is a secondary shock wave formed inside the lower portion of the shock tube in the Mach 1.66 case. Additionally, some part of the expansion wave formed at the lower diffraction edge meets the inside of the upper portion of the shock tube and induces some compressions there. Thus there is a secondary shock wave visible in the lower portion of the jet while a more diffuse compression fan is visible in the upper portion in frame c). These two compressive features meet near the tube axis and undergo what would appear to be regular reflection. However, as discussed in the consideration of the behaviour of conical shock waves, this cannot be the case since these features must be present all around the diffraction edge. Thus an irregular reflection of some sort must occur. This is confirmed by close examination

of frame e) which shows a shear layer feature downstream of the reflection point, consistent with the flow behind a Mach reflection.

Returning to the consideration of the Mach 1.28 flow, in frame d) the vortex is approximately two tube diameters from the tube exit. The jet appears aligned with the tube axis and is fairly uniform, although there is noticeable turbulence in the jet boundary, especially at the upper edge. There are no apparent secondary shock waves in the jet at this Mach number due to the jet being critically expanded or very weakly under-expanded.

Finally, at later times (Figure 5.12 frames e)) the Mach 1.28 and Mach 1.47 jets are steady with significant turbulence in the jet boundaries. In the Mach 1.28 case in particular the upper portion of the vortex has induced wave-like structures in the upper edge of the jet though these decay to turbulence quickly. In contrast the jet boundaries for the Mach 1.47 and Mach 1.66 cases, while turbulent, do not have any large-scale disturbance from the vortex. It is evident in the videos of the flow (see Appendix B) that the secondary shock waves waver. This is actually the termination of the shock waves in the jet boundary, the turbulence of which lends the wavering appearance.

5.2.1.3 Effect of exit plane angle

The flow fields for 45° and 60° exit plane inclinations are presented for the same range of Mach numbers in Figures 5.14 and 5.15 respectively. Qualitatively the flow field development for the 45° exit plane is similar to that for the 30° exit plane described in § 5.2.1.2 with only a few differences worth noting.

The jet is inclined upward in both the Mach 1.49 and Mach 1.66 cases (Figure 5.14 frames b) and c)) with even the bottom edge of the jet at least horizontal in both cases. While the upper edge of the jet is initially inclined upward (frame b)), it shows no inclination later in time in the Mach 1.28 case. This behaviour of the upper jet boundary being initially steeply inclined and then drawn shallower later in time by the vortex appears to be as a result of the induced velocity of the strong upper portion of the vortex ring, pronounced in the Mach 1.28 case where the upper portion of the vortex loop is at least twice as large in cross-sectional diameter as the lower portion.

The upper edge of the jet in the Mach 1.49 case also shows striations similar to that produced by the KHI. Given that there are counter-rotating vortex rings propagating around the primary vortex (noticeable in the videos in Appendix B), this provides further possible evidence of the hypothesis of Murugan and Das (2010) that these CRVRs may originate as KHI,

although the variation in vortex strength around its periphery would affect this induction and entrainment behaviour.

The secondary shock waves are visibly weaker for both of the higher Mach numbers and the shear tube emanating from the Mach disc is not discernible for either, though this is possibly attributable to the turbulence in the jet boundary blurring the interior of the jet. The weaker secondary shock waves are because more of the expansion wave originating at the upper diffraction edge, for example, will meet the inner surface of the shock tube for the same incident shock wave strength, because of the greater inclination of the exit surface. Since the inclination of the surface toward the origin of the expansion wave would be greater (since the secant of the circular cross-section of the tube subtended by the lateral spread of the expansion wave is greater), more of the secondary shock wave formed will be out of the tangent plane visible to the flow visualisation system. Therefore the tangent edge of the complex secondary shock wave would appear weaker.

The spread of the jet for the Mach 1.66 case is greater than for the 30° exit case. This is understandable given the stronger diffraction at the upper portion of the shock tube by the shock wave and thus the greater degree of under-expansion. In other respects the jets for the Mach 1.49 and Mach 1.66 cases are comparable to those in the 30° exit plane case. The disturbance of the jet boundary by the upper portion of the vortex for the Mach 1.28 case is more pronounced here and this seems causes the jet to be deflected downward in the far field.

The 60° exit plane flow field again shows further development of these features in Figure 5.15 however an important consideration is needed here. Unlike at shallower angles where the time between the start and the end of diffraction is reasonably short, at 60° the expansion wave generated by the diffraction at the most upstream edge of the exit lip will have affected the lower portion of the wave before the diffraction starts at the downstream edge. Therefore no part of the wave is plane when the final diffraction begins and thus the diffraction pattern will differ somewhat from the canonical two-dimensional studies due to the flow induced along the diffraction edge.

That said, the early stages of the development are very similar to that for lower exit angles. Specifically the scale of the upper portion of the vortex is similar to that for the lower angles as would be expected since the diffraction pattern is unaffected by increasing diffraction angle beyond diffraction angles of 90° (Skews 1967a). This greater strength means that the vortex approached an upright position much faster than at lower exit plane angles for all Mach numbers.

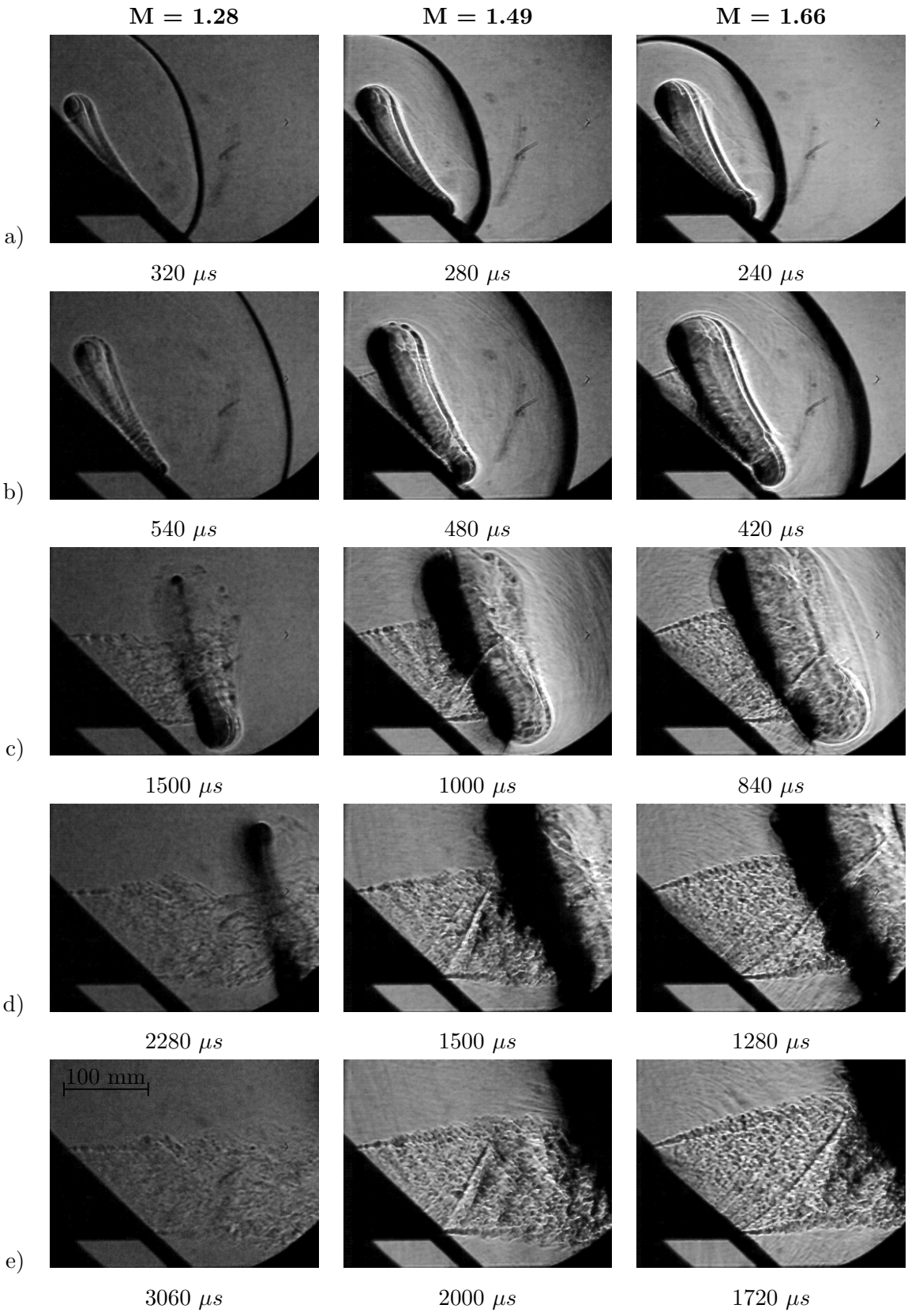


Figure 5.14: The flow field development for the exit of a shock tube inclined 45° to the normal for Mach numbers of 1.28, 1.49, and 1.66

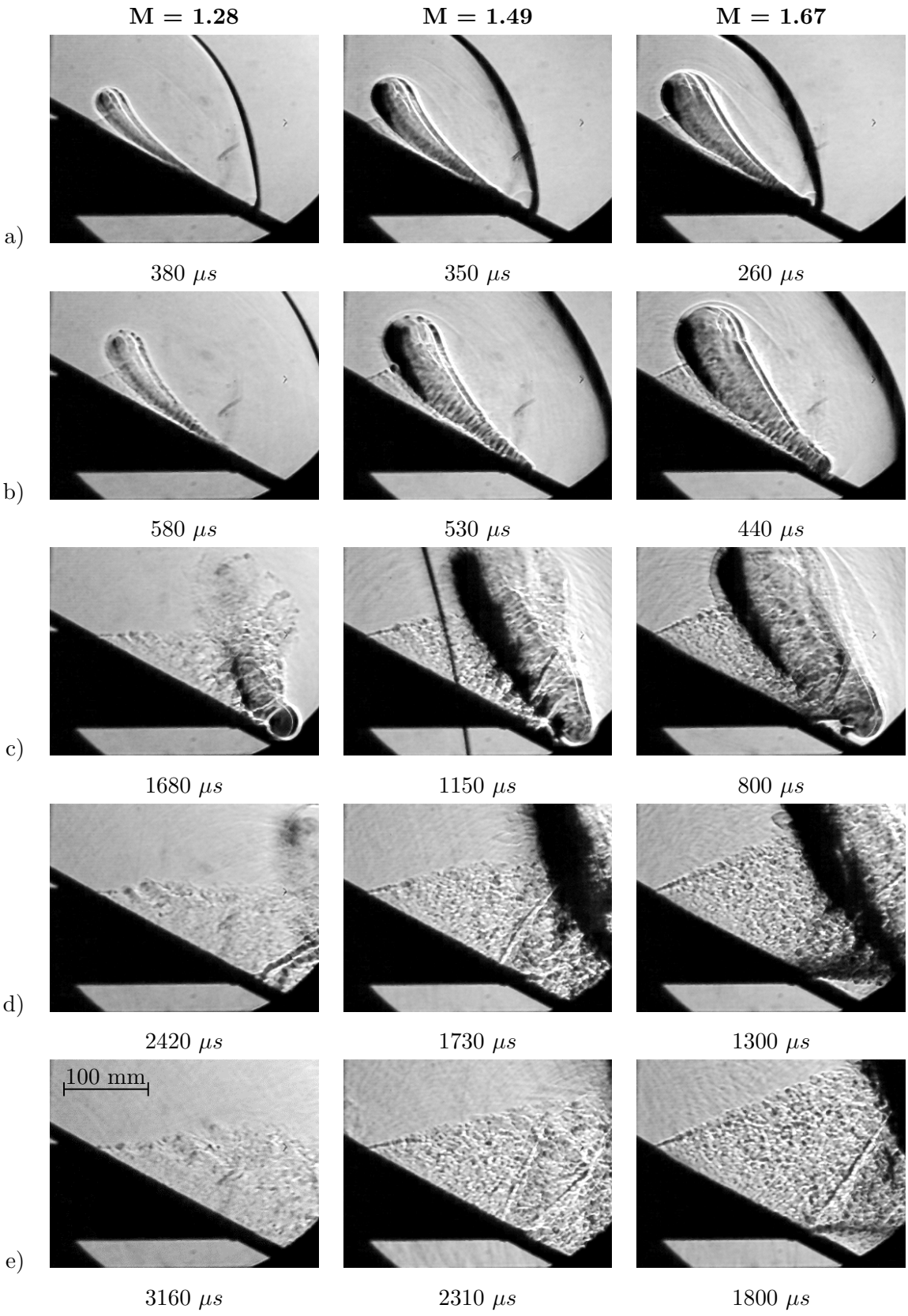


Figure 5.15: The flow field development for the exit of a shock tube inclined 60° to the normal for Mach numbers of 1.28, 1.49, and 1.67

At the downstream end, the vortex that is shed is much weaker than at shallower exit plane angles because of the acute diffraction angle of the shock wave in that area. This is clearest in Figure 5.15 frames c) where the lower portion of the vortex is not very coherent and shows signs of breaking down to turbulence quickly. This effect is more pronounced for lower incident shock wave strengths because of the overall weakness of the vortex formed.

The jet inclination and spread effects noted earlier are more pronounced here. Figure 5.15 frames d) and e) show this clearest. Especially worth noting is that the secondary shock wave clearly forms within the shock tube for both the Mach 1.49 and Mach 1.67 cases with it forming especially far upstream for the Mach 1.49 case. Again, due to the complex reflection of the expansion wave from the curved inner wall of the shock tube, the secondary shock wave is weaker. In the Mach 1.67 case, no upper secondary compression is visible because the expansion wave formed at the lower diffraction edge is weaker and cannot interact with the upper inner surface of the shock tube because of the steeper inclination of the exit plane.

Finally, there are two features of the jet worth noting at this higher inclination. First, the breakdown of the upper edge of the jet for the Mach 1.28 case is even more pronounced here though it seems that it is, in fact, independent of the upper portion of the vortex but related to the location of the downstream diffraction edge. In addition, for the Mach 1.28 and Mach 1.47 cases the late-time jet runs along the lower portion of the exit plane. This represents a change from jetting flow, expected from a shock wave emanating from a pipe, to the diffracted flow behind a shock wave from shallow diffraction, as described in Skews (1967a). This is not evident in the Mach 1.67 case as the flow appears to separate before possibly later reattaching to the lower portion of the plate.

5.2.1.4 Extreme exit plane angle

As discussed in Skews (1967a), the two-dimensional diffraction of a shock wave over a corner with a 15° angle sheds no vortex. Thus, as a limiting case of the behaviour studied here, a model was created with an inclination of 75°, with a resultant downstream diffraction angle of 15°. Since the length of the shock tube exit aperture at this angle is approximately 370 mm, the development of the flow field had to be visualised in two phases, namely upstream and downstream regions. This also necessitated a change in the selected frames for consideration because, for example, the shock wave will not have diffracted at the downstream edge when the portion along the centreline has traversed one tube diameter. In the downstream tests, the upstream edge of the exit aperture is not visible due to the limitations of the flow visualisation and so the selected frames there were selected based on the start of diffraction at the downstream edge.

5.2.1.4.1 Upstream flow field

The selected frames for the upstream tests are given in Figure 5.16. The instances chosen when considering the development of the flow field were: when the diffracted shock wave is approximately 1 and 2 tube diameters downstream; and then when the vortex ring formed at the exit of the shock tube at the centreline has convected approximately $\frac{1}{2}$, 1, and $1\frac{1}{2}$ tube diameters away from the exit plane.

Here again the early development of the flow field is similar to that seen thus far. The inclination of the upper edge of the jet is evident from the first frame (since the flow time is much later at the point where the centreline shock wave has travelled 1 tube diameter) . As before though, the upper jet boundary for the Mach 1.27 case quickly becomes more aligned with the tube axis while it persists in pointing upward for the stronger shock waves.

A less-evident feature in the still images but clear in the embedded videos in Appendix B is that a kink develops in the downstream surface of the vortex near the boundary of the upper cross-section. This kink travels down the vortex face and the effect is a folding or crumpling of the vortex in the downstream direction. The cause is that while the upper portion of the vortex is the result of strong diffraction and coherent, the lower portion weakens rapidly and thus a closed vortex loop cannot form because somewhere near the downstream diffraction edge, no vortex will be shed. Since a vortex cannot terminate in free space, the weak edges of the vortex must terminate in the exit plane surface and so the vortex arch is forced upward. The weak coherence of the ends of the vortex means that this stress of the vortex filament is reduced since the ends are a turbulent field.

At late times the distortion of the upper edge of the jet boundary for the Mach 1.27 case is clear even though it is nearly parallel to the tube axis. For the stronger incident shock waves the jets remain inclined steeply away from the tube axis and no secondary shock waves are visible. No secondary shock wave could be expected in the upper portion of the jet because of the very weak diffraction at the lower diffraction edge and the impossibility of the expansion interacting with the upper inner surface of the shock tube. At very late times for the Mach 1.48 case a weak secondary shock wave forms inside the shock tube but the complex interaction here means that the expansion will more likely reflect as a compression fan than a more coherent shock wave. This is not visible for the Mach 1.67 results in the upstream position.

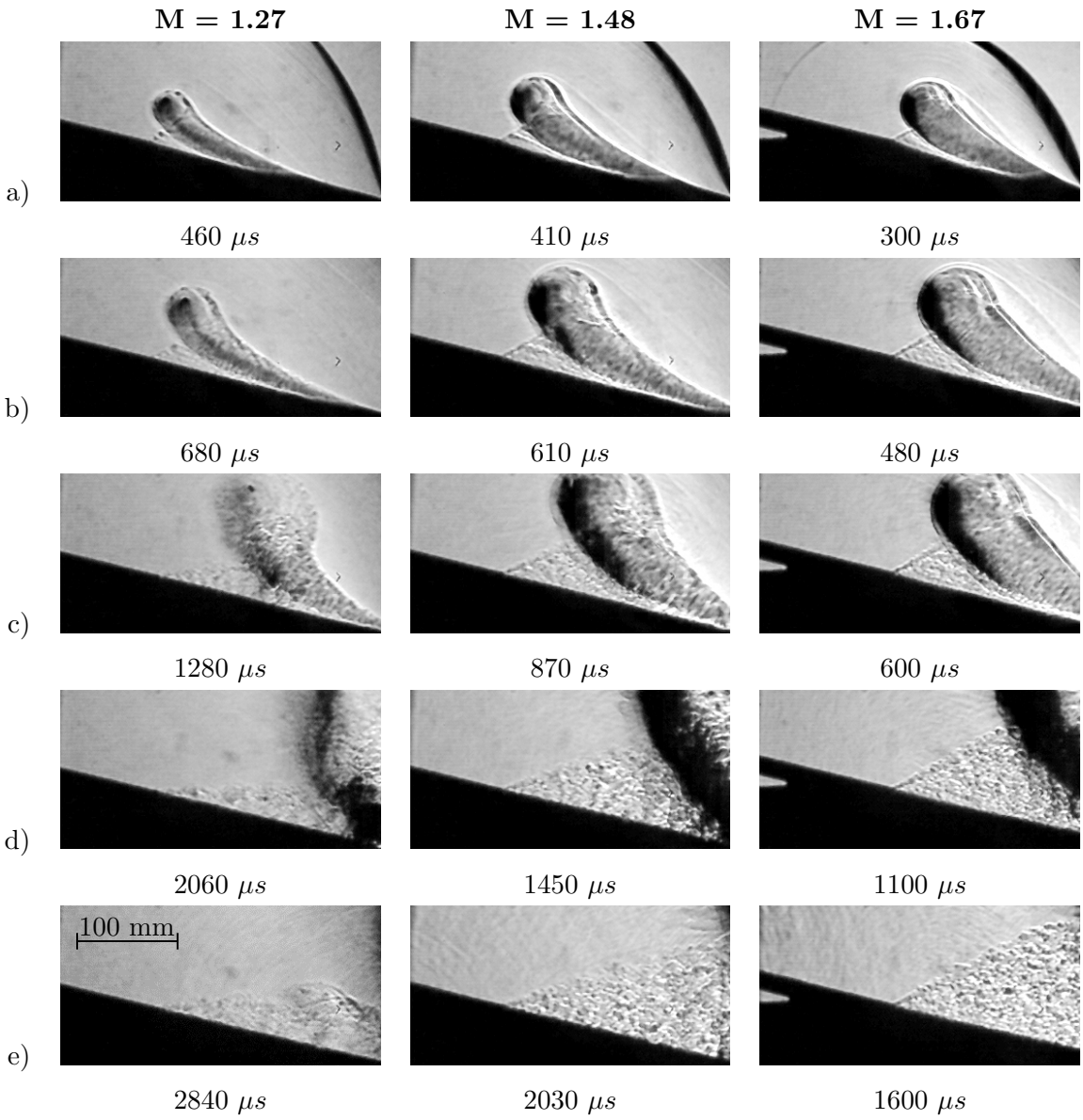


Figure 5.16: The flow field development for the exit of a shock tube inclined 75° to the normal for Mach numbers of 1.27, 1.48, and 1.67

5.2.1.4.2 Downstream flow field

The selected frames for the downstream tests are given in Figure 5.17. The instances chosen when considering the development of the flow field were: when the diffracted shock wave is approximately 1 and 2 tube diameters downstream of the downstream diffraction point; and then when the vortex ring visible near the downstream edge of the exit of the shock tube first arrives at the diffraction point and then when it has convected approximately 2 and 3 tube diameters away from the diffraction point.

In Figure 5.17 frames a) for Mach numbers 1.49 and 1.67 it is clear that the vortex shed along the exit lip of the shock tube reduces to zero cross-sectional diameter since the vortex profile comes to a point near the downstream diffraction edge even though the wave is some distance from it. However no such vortex is visible in the Mach 1.27 case.

This is not visible in the Mach 1.27 case because the vortex becomes more pronounced as the stronger upper portion convects downstream and entrains the weaker vortex shed at the acute diffraction portions of the tube lip. Thus, the angle of the tapering of the vortex as it approaches the downstream diffraction edge is greater in the Mach 1.67 case than in the Mach 1.49 case because a greater effect from the stronger upper portion of the vortex in the former case has entrained more of the weak vortex shed at the downstream edge. Since the vortex shed in the Mach 1.27 case is weaker overall, it will take longer for the effect of the upper portion to affect the lower portion, which may be vanishingly small, due to the lower induced velocities. Thus the continued absence of the vortex in frame b) for the Mach 1.27 case while the vortex has noticeably steepened in both of the higher Mach number cases.

In Figure 5.17 frames c) the effect of the stronger upper portion of each of the vortices has reached the downstream diffraction edge and the vortex presents as an increasingly steep wedge with increasing Mach number. More noticeable is that the portion of the vortex near the axis of the tube is increasingly turbulent with decreasing Mach number. There appear to be several smaller induced vortex lines in the Mach 1.27 case while the vortex front for the Mach 1.67 case is still quite coherent. In the following frames d), the jet flow rolls along the lower exit plane with a stronger leading edge vortex as Mach number increases. The higher momentum of the stronger jet above the centreline induces an additional vortex, which explains the increasing strength of this vortex tube as Mach number (and hence upper jet velocity) increases. This vortex tube again cannot terminate in free space and must therefore either connect to the upper vortex arch or terminate in the surface. This cannot be determined from the experimental images.

The overall effect of this induced vortex flow on the lower diffraction surface (shown in Figure 5.17 frames e)) is that, despite the weak diffraction of the shock wave at the downstream diffraction edge because of the shallow angle, the bulk flow emanating from the shock tube is along the lower surface. This effect was already discernible weakly in the 60° case but here, even for an incident shock Mach number of 1.67, the flow appears to remain attached to the exit surface and the jet is no longer inclined away from the exit plane.

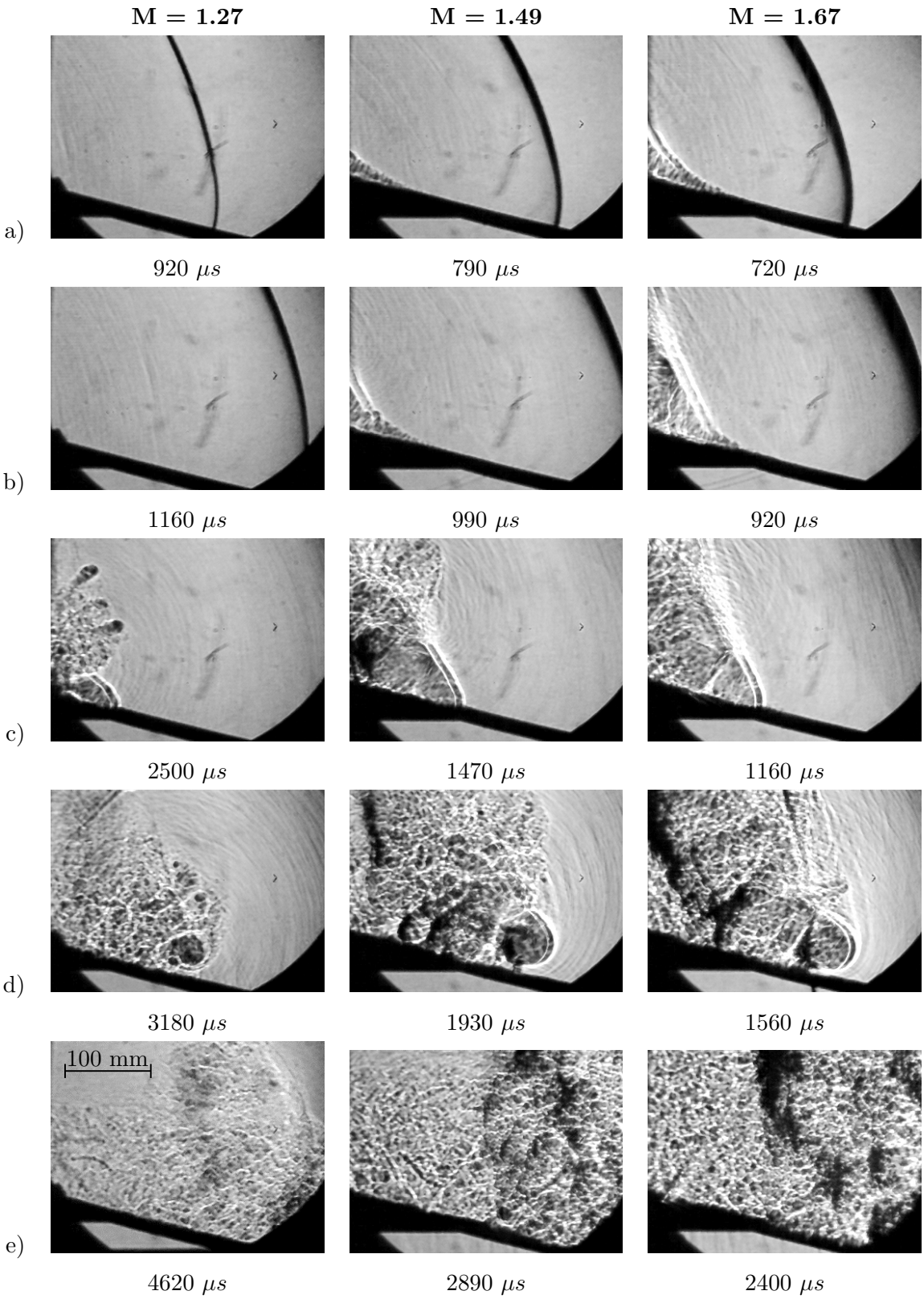


Figure 5.17: The flow field development for the exit of a shock tube inclined 75° to the normal for Mach numbers of 1.27, 1.49, and 1.67

While this seems to contradict the upward inclination of the jet for the higher Mach numbers observed in the upstream tests, the overall effect is consistent throughout all of the data presented. The jet shows increasing spread and upward inclination with increases in both Mach number and exit plane inclination. However, as seen in the weaker Mach 1.27 cases, the jet is initially spread and inclined in these ways and it then returns to a simple free cylindrical jet, albeit with high edge turbulence near the remains of the diffraction vortex. These transient effects are stabilised by the greater flow momentum and pressure differences caused by both the higher Mach number of the incident shock wave and the stronger upstream diffraction and so the relaxation to a cylindrical jet is simply slower for higher values of these properties. While the steady state would appear to be unchanged from the canonical free jet, these effects do suggest interesting ways in which such jets could be dynamically adjusted.

Finally, at very late times in the videos and somewhat in frames e) of the Mach 1.49 and Mach 1.67 flows the lower secondary shock waves do form in the shock tube though they are quite weak. These waves seem to move upstream in the videos and the precise cause of this change in position would need to be determined.

5.2.2 Computational Fluid Dynamics

Given the limitations of the experimental images to fully describe the flow field because the imaging can only be made in one orientation, a complementary computational fluid dynamics (CFD) study was undertaken to better explain the observed phenomena. Due to time constraints arising from the model size (described more fully below) only the 75° exit plane case was modelled for a range of Mach numbers.

5.2.2.1 Model parameters

The CFD was performed using ANSYS Fluent 17.2. The domain was developed such that there were at least 2 tube diameters upstream of the most upstream point of the diffraction edge. The total domain width was 550 mm, directly analogous to the exit plane plate width used in the experiments, though the domain size was reduced by employing the lateral symmetry of the model and only modelling half of the domain. The region downstream of the domain was modelled as a truncated domain which resembles the approximate shape of the diffracted shock wave in the far field to reduce the total number of computational nodes. Most of the boundaries of the domain were modelled as walls, though the inlet to the shock tube was modelled as a compressible inlet (the pressure-inlet boundary type) and the downstream faces as a non-reflecting compressible outlet (the pressure-outlet boundary type). An elevation of the computational domain is shown in Figure 5.18.

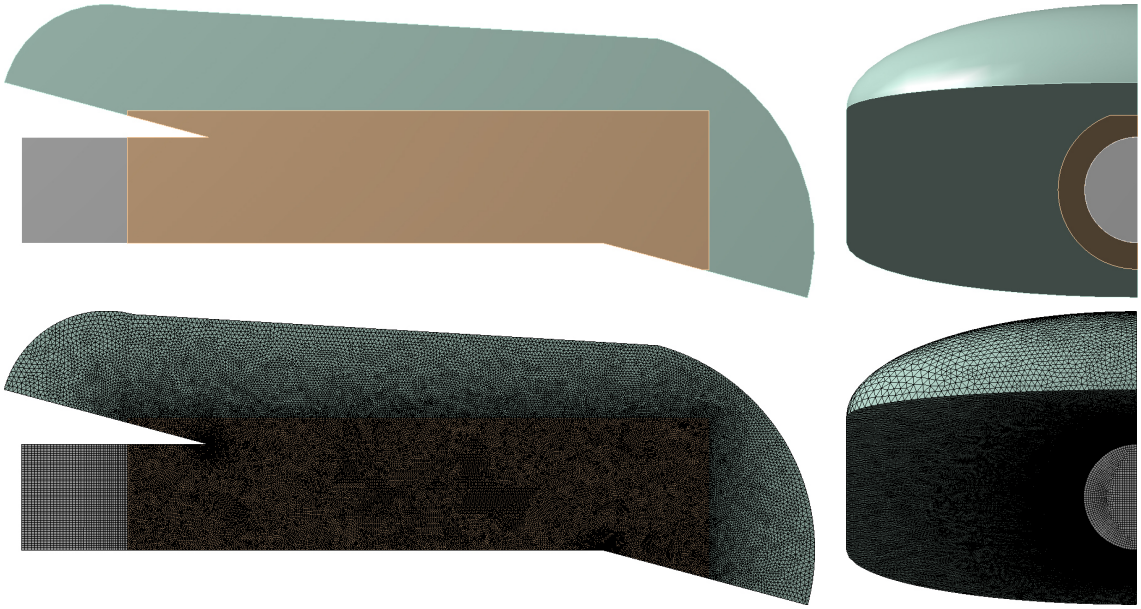


Figure 5.18: Geometry (*top*) and mesh (*bottom*) for shock diffraction at the exit of a shock tube inclined 75° to the normal. The view of the domain in elevation of the symmetry plane (*left*) and looking in the direction of shock wave travel (*right*) are given

Following a simple mesh independence study, the domain was initially meshed using a tetrahedral-dominant scheme with several refinement regions. A cylindrical region of refinement (shown in orange in Figure 5.18) centred on the axis of the shock tube and extended approximately 1 tube diameter upstream and downstream respectively of the corresponding limits of the diffraction edge and with a diameter of 1.5 tube diameters was employed. While the limiting cell size in the bulk of the domain was 3 mm, the imposed cell size limit on this region of refinement was 1.5 mm. Additionally, a minimum cell sizing of 0.75 mm was imposed on the diffracting edge where the shock tube intersected the exit plane. The growth rate of cells between these various values was capped at 2.5%. Using these values, the initial mesh for use in ANSYS Fluent comprised approximately 18 million mostly tetrahedral cells with a mean element quality of between 0.85 and 0.9, though the region between the pressure inlet face and the start of the refinement cylinder was meshed with hexahedral cells with a mean quality of 0.95. The cell quality is a composite metric comparing cells by skewness and aspect ratio to cubic and regular tetrahedral cells for hexahedral and tetrahedral cells respectively. A cell quality of 1 indicates cells with ideal regularity while a cell quality of 0 represents cells with negative cell volume.

The model was processed using the three-dimensional, double-precision Fluent solver for density-based equations. Due to time and resource limitations, all models were solved using an inviscid solver with a Courant-Friedrichs-Levy factor of 0.5, though this was reduced to 0.2 for the Mach 2.2 model, and constant time stepping of 1 μs. An implicit Roe-FDS scheme was

used for linearisation and second-order upwind schemes were used for spatial discretisation. Adaptive mesh refinement based on the curvature of velocity magnitude, density, pressure, and temperature was used to refine the mesh every 10 μs. Models were calculated for between 1 400 μs for a Mach 2.2 incident wave and 2 300 μs for a Mach 1.25 model with additional calculation as necessary to get data for particular times outside of these ranges. The incident shock wave Mach numbers considered were 1.25, 1.4, 1.6, and 2.2. Although the final Mach number could not be tested experimentally, it was selected as the minimum Mach number for which the post-shock flow is supersonic (approximately 1.06).

The simulations were executed on a cluster of Intel Core i7-3770 processors with a typical allocation of 40 compute processors per model for a total run time of around 240 hours per model. It was due to the limited availability of cluster time and the duration of the model execution that only such a limited number of cases were run. Later, additional runs were performed with up to 216 processes on Intel Xeon E5-2690 processors though time and availability limitations here also constrained to total flow time and number of cases that could be modelled.

5.2.2.2 Results

For direct comparison with the experimental results a combination of two visualisations was used. The first was the static pressure on the symmetry plane of the model since that would approximate the schlieren images (although these are based on gradients of density). Numerical schlieren could not be usefully implemented in these data sets as the integration of the gradient data through the domain exceeded the available computational resources. Moreover, the simplified data represented on the symmetry plane were deemed more informative when considering the data.

The second was the visualisation of the primary vortex loop (or line). This was visualised using isosurfaces of the λ_2 eigenvalue of the velocity gradient tensor originally proposed by Jeong and Hussain (1995) coloured by contours of static pressure. The wall surfaces of the model have been filled with contours of static pressure so that the progress of the shock wave and related expansion waves along those surfaces can also be seen. All contour values were defined for the Mach 2.2 case so that the features there could be clearly resolved. The same values were used for all Mach numbers for consistency of representation. The isovalue of λ_2 used (-1e8) was selected as it produced vortex tubes at early times closest to those observed experimentally.

5.2.2.3 Model validation

The results of the computational modelling were validated by direct comparison of features at key time points in the development of the flow field. Given the fact that the experimental flow field was visualised in an upstream and a downstream region, the validation was similarly split.

5.2.2.3.1 Upstream flow field

When considering the upstream portion of the flow field the principal features for validation were the shock wave position, vortex position, and vortex shape. Overall, when accounting for the differences in actual Mach number of the incident shock wave between the CFD and the uncertainty due to the estimation of the initial diffraction time in the experiments of approximately 5 μs, the final error between the CFD and experimental data was less than 2% for the shock wave position though it was around 25% for the vortex position for the Mach 1.27 case decreasing to less than 10% for the Mach 1.67 case. These comparisons are shown in Figures 5.19 to 5.21.

Considering frames a) and b) in each of Figures 5.19 to 5.21, the vortex tube shows good agreement in general shape though it appears consistently thinner in the CFD than in the experimental images. This can largely be attributed to the selection of the value of λ_2 used for creating the visualisation of the vortex from the CFD results. Although the range of values for λ_2 is large, the appearance of the vortex tube visualised is quite sensitive to the isovalue selected. Thus, the selected value was chosen for best overall representation although it represents effectively the stronger inner portion of the vortex tube and the difference in the experimental images is due to the more diffuse outer region of the vortex tube.

Another feature to note regarding the visualisation of the vortex tube (as seen in frames c) onward in Figures 5.19 to 5.21) is the apparent disappearance of parts of the primary vortex tube near the top of the image. The reason for this is that the vortex tube crosses the computational domain boundary at these times. Since the velocity gradients required to calculate the λ_2 eigenvalue cannot be calculated at these points due to a lack of information, there are no points of the selected λ_2 value (even away from the domain boundary) and so the vortex tube displayed develops gaps. While this could be countered by extending the computational domain, it was deemed unnecessary to do so as the vortex effect on velocity and other flow parameters was still modelled.

Considering first the flow field for the Mach 1.25 incident shock wave in Figure 5.19, the shock wave shape shows good correlation but the position in the experiments is ahead of

that in the CFD since the actual Mach number was higher (M1.27). The apparent kink in the downstream profile of the vortex tube is resolved as is the sharp curvature of the vortex tube centreline near the position of the upper boundary of the jet. As discussed in § 5.2.1.4, this is due to the stronger upper portion of the vortex convecting rapidly downstream while the weaker lower section starts to lose coherence. The stretching of the vortex line by this weakening of the feet of the vortex arch results in increased circulation in the stronger region and thus even greater convection speed.

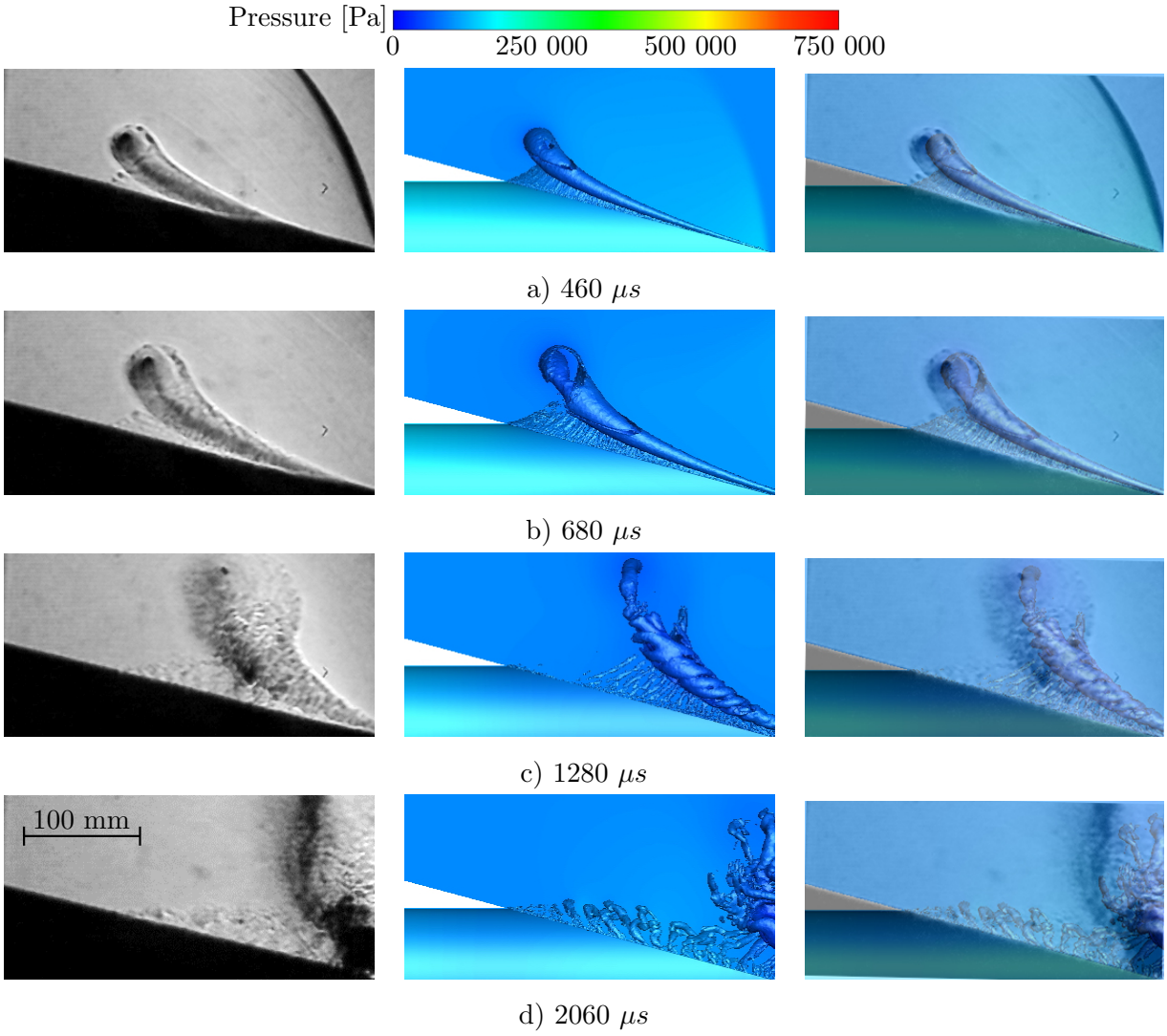


Figure 5.19: Comparison of the experimental and computational images at the upstream position for the Mach 1.27 (experimental) / Mach 1.25 (numerical) case. A direct overlay of the computational and experimental results is given at the far right

Similar behaviour is seen in both Figures 5.20 and 5.21 for Mach numbers 1.4 and 1.6 respectively, though again the stronger actual incident shock wave in the experiments means that the difference in shock wave position is quite stark. However, the λ_2 isosurfaces also

identify the induced vortices in the jet boundary and this helps to verify the inclination of the upper surface of the jet boundary. This is lower for both Mach numbers in the CFD than in the experimental images though the increasing jet boundary inclination with Mach number would mean that the experimental positions (for incident shock waves 4% and 6% stronger than the CFD respectively) would be expected to be greater.

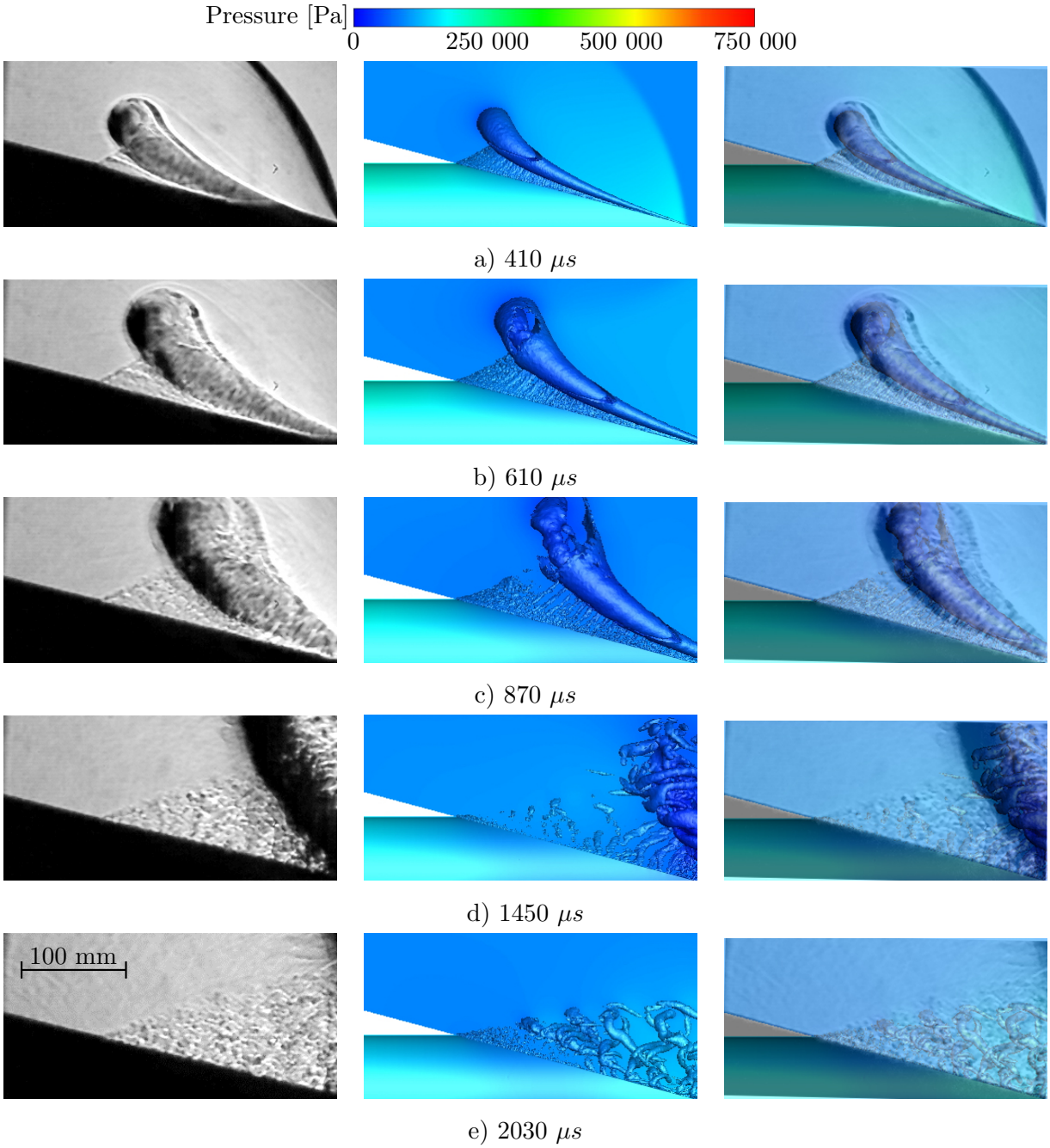


Figure 5.20: Comparison of the experimental and computational images at the upstream position for the Mach 1.48 (experimental) / Mach 1.4 (numerical) case. A direct overlay of the computational and experimental results is given at the far right

One particular point of interest in Figure 5.19 frame d) is the appearance of the developing jet as adhering to the exit surface. Since at the downstream end of the exit aperture there is no separation of the flow, there is the requirement that there is a transition from a free jet (in the upper region) to a diffracted surface flow (in the lower region). The breakdown of the vortex arch is thus a mechanism by which this is imposed on the flow physically.

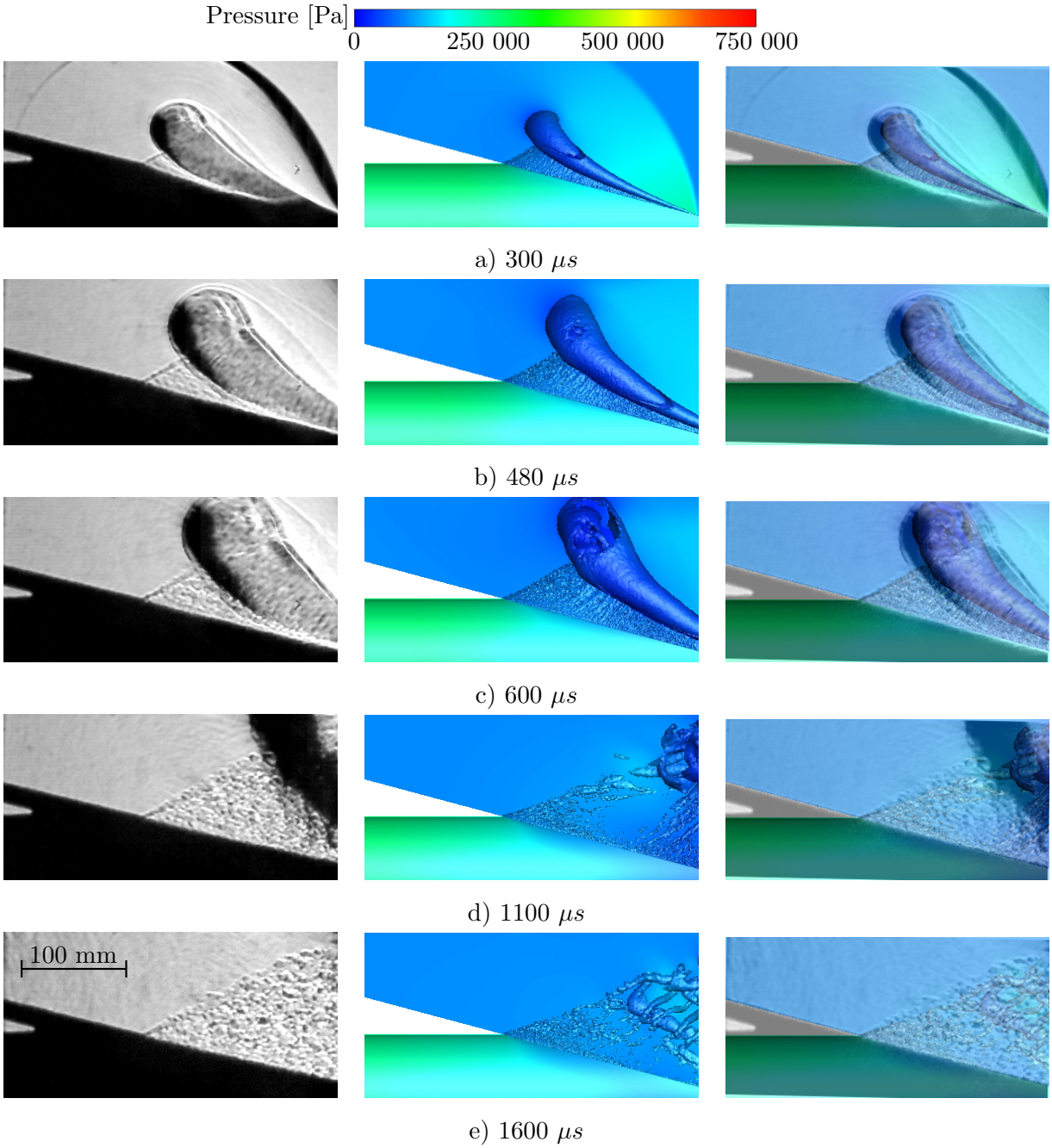
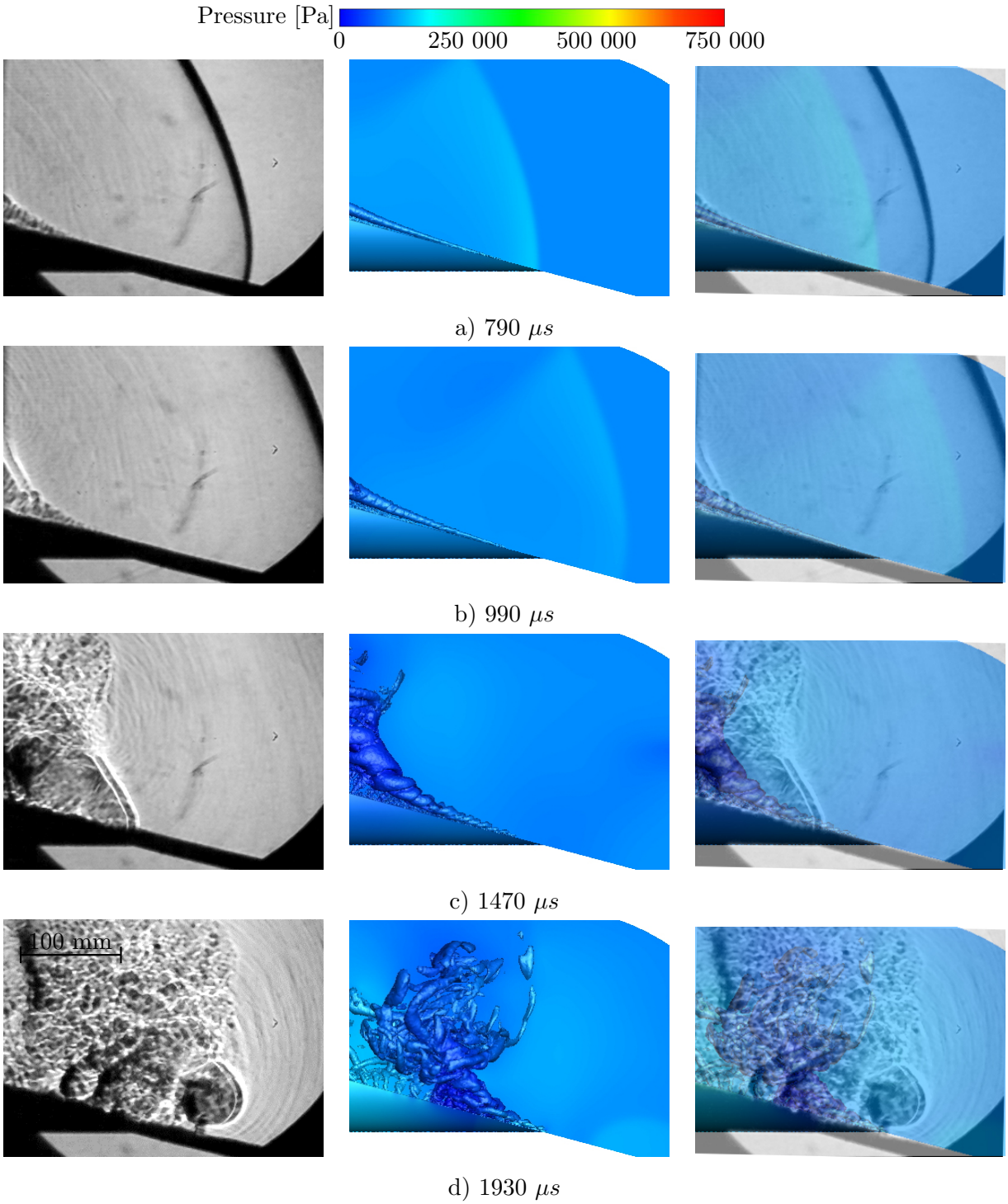


Figure 5.21: Comparison of the experimental and computational images at the upstream position for the Mach 1.67 (experimental) / Mach 1.6 (numerical) case. A direct overlay of the computational and experimental results is given at the far right

5.2.2.3.2 Downstream flow field

Given the limited experimental visual data and computational data for the Mach 1.25 case, the downstream validation considers only the Mach 1.4 and Mach 1.6 cases.



a) 790 μs

b) 990 μs

c) 1470 μs

d) 1930 μs

Figure 5.22: Comparison of the experimental and computational images at the downstream position for the Mach 1.48 (experimental) / Mach 1.4 (numerical) case. A direct overlay of the computational and experimental results is given at the far right

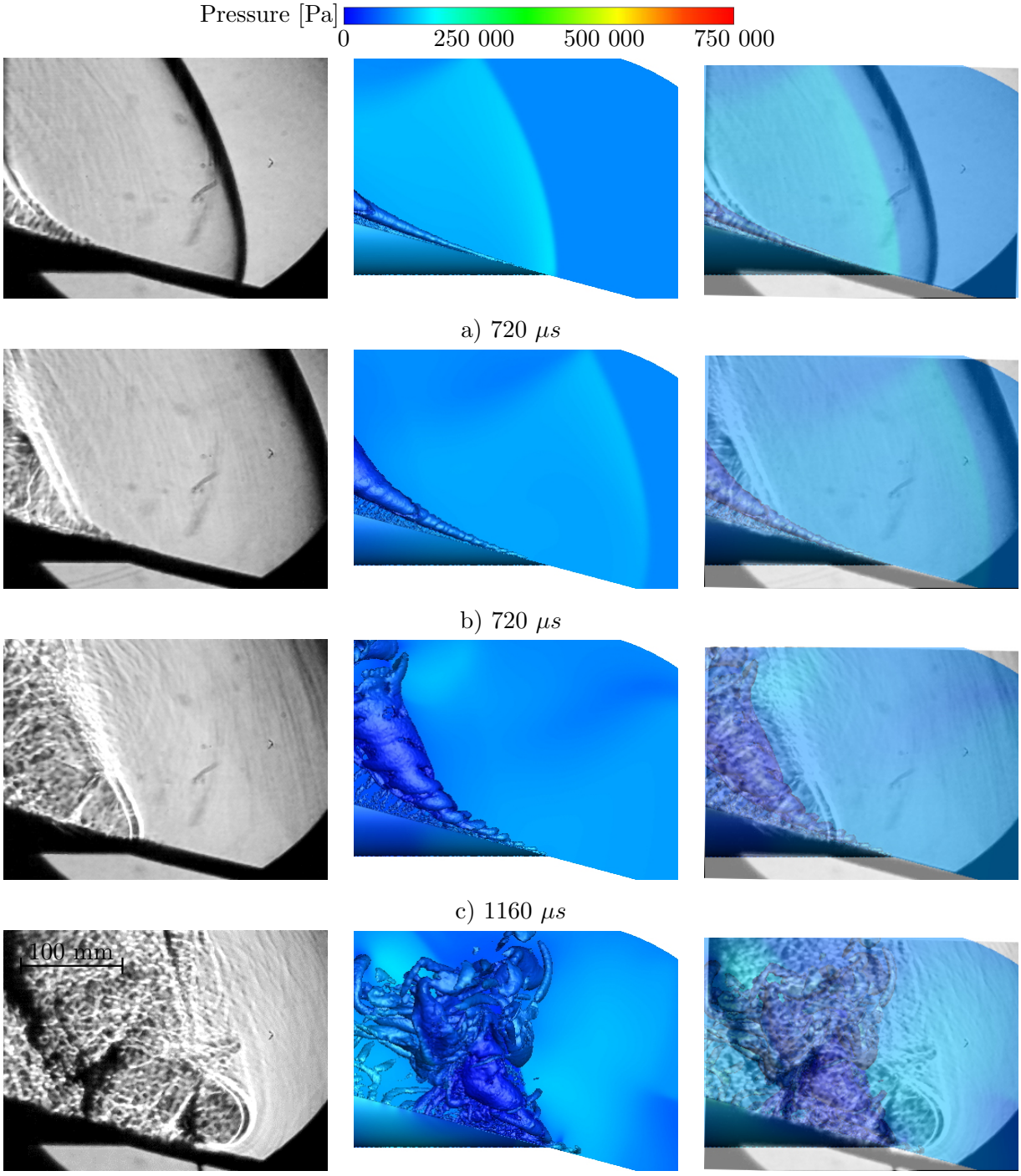


Figure 5.23: Comparison of the experimental and computational images at the downstream position for the Mach 1.67 (experimental) / Mach 1.6 (numerical) case. A direct overlay of the computational and experimental results is given at the far right

Here again the shock wave shape and position were considered as validating criteria but the difference in incident shock wave strength between the experimental and computational results meant that the position appears poorly resolved while the shape is similar. This is

exacerbated by the fact that the exact time of the initial diffraction at the upstream diffracting edge could not be directly determined visually but rather was estimated by extrapolation from the upstream results. Thus, as shown in frames a) and b) of Figures 5.22 and 5.23, the shock waves in the given images do not coincide at all. However, when taking into account the differences in incident shock wave strength and the uncertainty of the initial diffraction time, the actual error in shock wave position is less than 5%. This was considered sufficient since it is the detailed behaviour of the lower portion of the vortex arch at these positions that is of greater interest in understanding the flow development.

In frames c) of these figures the the initial comparison of the vortex shape and position is good though again the computational vortex appears thinner. This is especially true in the Mach 1.4 case where the computational vortex arch appears as a rope-like and quite coherent shape while the experimental image shows a much thicker foot of the vortex arch. This is largely due to the inviscid computational model since, at the earlier time shown in frame b) there is good comparison between the vortex shapes in each case. In frame d) of both Figures the breakdown of the vortex arch is clear and quite well modelled computationally.

One feature that is missing in frame d) of both Figures 5.22 and 5.23 is the rolling flow in front of the vortex identified in § 5.2.1.4. Partly this is expected as such a flow would be unlikely to be strong enough to produce values of λ_2 that would be presented in the selected results. In addition, though, it must be considered that the rolling flow could be as a result of the boundary layer from within the upstream shock tube interacting with the spreading flow along the lower exit surface. Since the computational model used was inviscid and the section of the upstream shock tube modelled short relative to the actual experimental apparatus, this feature would not be captured computationally. Considering this, the validation of the computational model at the downstream position is considered sufficient for further analysis using the results for higher Mach numbers.

5.2.2.4 Further results

Given the difficulty in definitely identifying flow features from the view points available experimentally, the computational model was used to further elucidate the flow field by visualisation of isometric elevations of the vortex development. These were selected at the same times at which the experimental elevations were presented for the purposes of direct comparison.

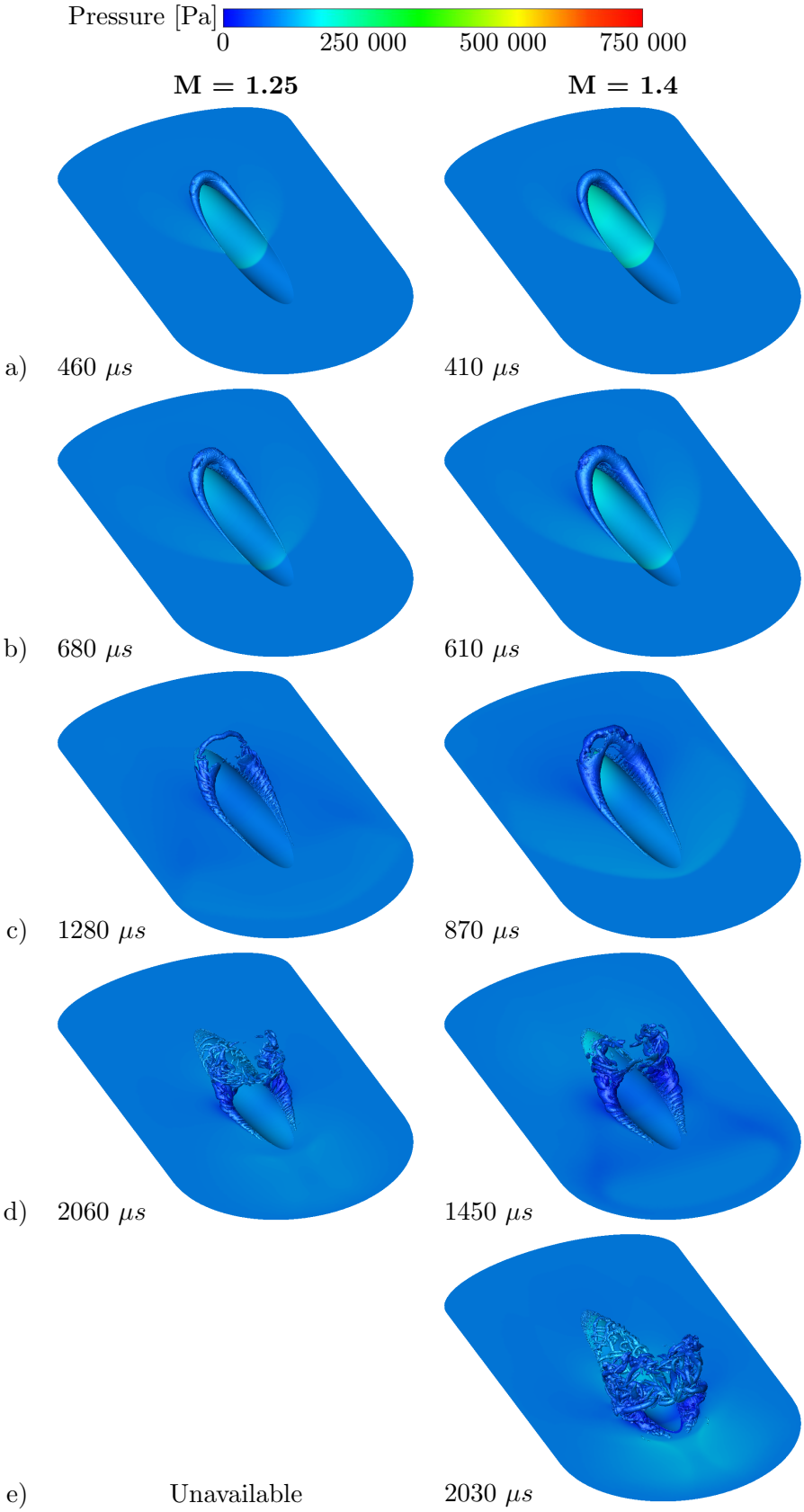


Figure 5.24: The computational vortex development for the exit of a shock tube with an exit surface angle of 75° for Mach numbers of 1.25 and 1.4

Looking first at the vortex development for the Mach 1.25 and Mach 1.4 cases in Figure 5.24, the initial vortex shedding at the upper edge of the diffraction aperture shown in frames a) is very similar though the vortex tube for the stronger incident shock wave appears marginally thicker. This similarity continues in frames b). However, close comparison of the images in frames a) and b) for both Mach numbers shows that the vortex arch terminates at a sharp point in the surface of the shock wave initially but that by the time the incident shock wave front has passed the mid-point of the aperture, those tapered feet of the vortex tube are some distance back from the shock front. The weaker diffraction at these azimuthal positions, some angle less than 90°, means that there has been insufficient momentum of the diffracted flow to induce a vortex. Thus the vortex tube terminates in an infinitesimal point adjacent to the surface.

The effect of this is that the stronger upper portion of the vortex starts to convect downstream, as shown in frames c), while the feet of the vortex arch remain approximately in the same positions. The effect of this is clear in frames d) where there is a strong curvature of the vortex arch near the feet toward the more vertical portion at the top of the vortex arch.Note that in frames d) the seeming incoherence of the top of the vortex arch is due to the truncated domain size but that the vortex remains coherent in those positions. Finally in frame e), available only for the Mach 1.4 incident shock wave, the feet of the vortex arch are breaking down into turbulence and this is spreading to the upper portions of the vortex arch. The spreading of the flow exiting the shock tube along the exit surface can also just be discerned in that frame.

Considering now the development of the vortex arch for the stronger Mach 1.6 and Mach 2.2 incident shock waves in Figure 5.25 the vortex appears initially smooth and terminates in a sharp foot at the diffraction surface. Unlike in the lower incident shock wave strength cases, the stronger diffraction means that the termination of the vortex tube is farther downstream and that the curvature of the vortex in side elevation near the foot is lower because of the greater overall strength. Ignoring the apparent loss of cohesion of the top of the vortex arch in frames d), it is clear that the feet of the vortex arch for the much stronger Mach 2.2 shock wave extend almost to the downstream limit of the diffraction aperture and that the vortex arch is lifting off of the diffraction surface almost as a plane vortex ring.

In the final frame the Mach 1.6 vortex arch shows signs of breaking down into turbulence while the Mach 2.2 vortex arch has almost closed into a vortex loop, albeit one which shows signs of turbulence near the foot. This suggests that even for very steep inclinations of the exit plane, and corresponding shallow minimum diffraction angles, a stronger shock wave will shed a vortex which may still close into a loop rather than terminating in the exit surface.

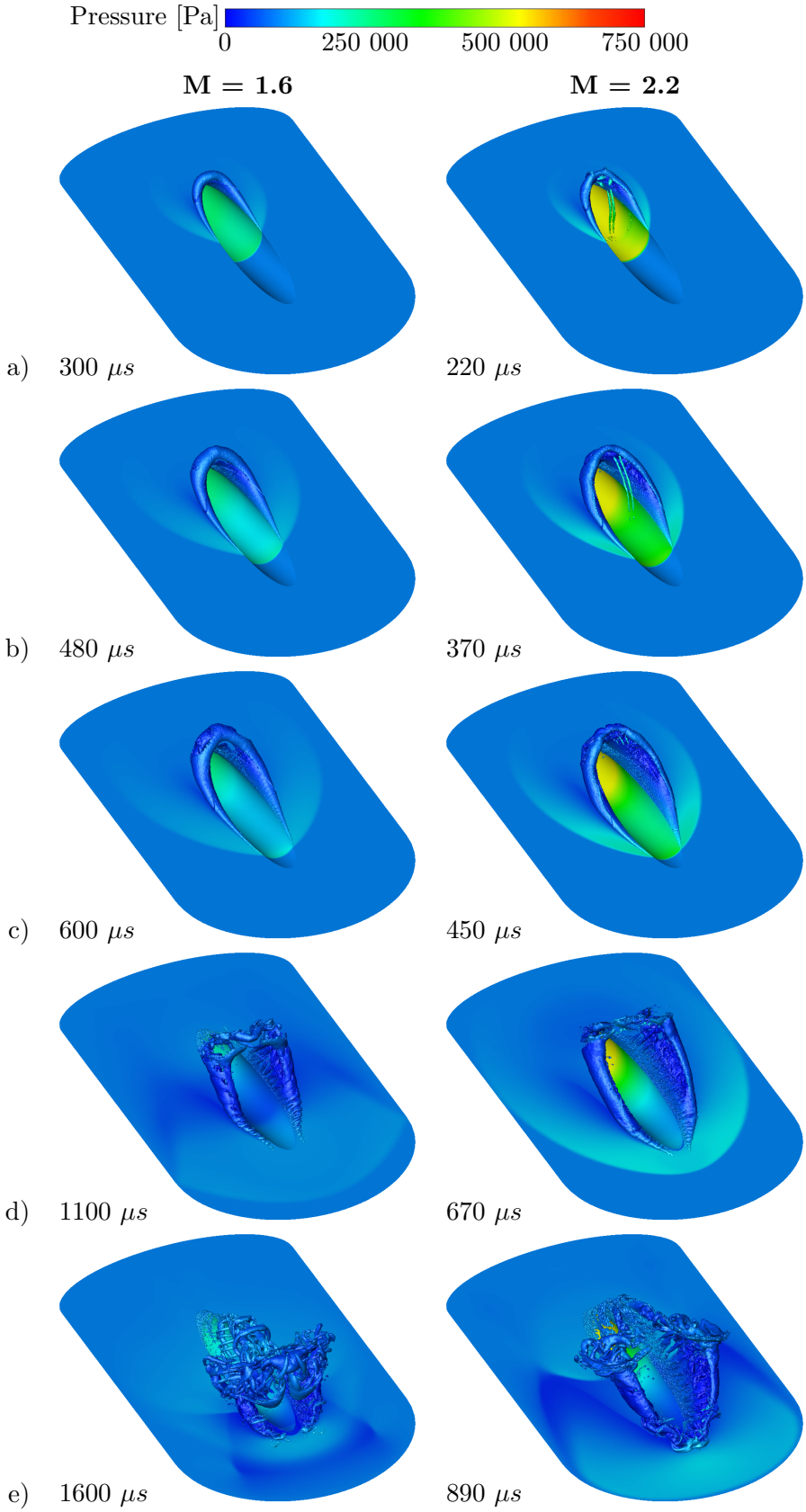


Figure 5.25: The computational vortex development for the exit of a shock tube with an exit surface angle of 75° for Mach numbers of 1.6 and 2.2

Given that the breakdown of the vortex arch by turbulence appears to be the mechanism whereby the transition from a free jet to spreading diffracted flow is achieved, this makes sense since the higher momentum of the post-shock flow for very strong incident shock waves would stabilise a free jet and the induced flow at the jet boundary would promote the closure of the vortex loop at the lower side.

5.2.3 Summary

The diffraction of a plane shock wave from an inclined exit presents several features of the flow field not seen with normal exits. The first is that the jet emanating from the pipe behind the jet will be initially inclined away from the inclined surface and this effect is exaggerated by increasing exit plane inclination and incident shock wave Mach number. This jet inclination decreases as time progresses as a result of the influence of the strong vortex shed at the upstream diffracting edge.

The jet for an inclined exit may also include compressions or even shock waves induced by the reflection of the expansion fan produced at the upstream diffracting edge with the inner surface of the shock tube near the downstream diffracting edge. Given that this expansion fan varies in strength around the periphery of the shock tube exit, this interaction is complex. The effect increases initially with increasing exit plane inclination but then decreases as the increased time for full diffraction with increasing exit plane surface inclination causes weakening of the shock wave and greater three-dimensional effects.

The variation of the diffraction angle around the periphery of the exit means that the strength of the vortex formed varies around the diffracting edge length. For cases of shallow exit surface inclination the effect is to produce a vortex loop which is of greater strength in the section shed at the upstream edges. For a circular cross-section tube this will also mean that the higher curvature of the initial vortex caused by the higher curvature of the diffracting edge at the upstream and downstream limits will produce vortices with higher curvature at these limits. This greater curvature increases the induced velocity of this portion of the vortex and so the vortices shed from these edges start inclined similarly to the exit plane inclination but quickly convect into a position normal to the shock tube axis, and later tilt in the downstream direction at late times for strong incident shock waves.

In cases where the exit plane inclination is high, this behaviour is complicated by the fact that no vortex is shed at the shallowest diffraction angles. The incident wave will no longer be plane at that time because of the effect of the diffraction at edges farther upstream but, regardless, the effect is that the vortex shed at upstream positions cannot close into a vortex loop but rather forms into a vortex arch terminating in the exit plane surface. This weaker

portion of the vortex quickly loses coherence and acts as a destabilising influence on the rest of the vortex causing an early decay of the stronger vortex coherence. It seems that this is the mechanism by which the jet emanating from a shock tube with a steeply inclined exit plane is changed into a diffuse flow along the downstream surface.

5.3 Flow Produced by Diffraction of a Plane Shock Wave at the Curved Exit of a Shock Tube

5.3.1 Experimental results

The results for the curved exit surfaces tested are given in Figures 5.26 to 5.29 below. Unlike the inclined exit plane results already discussed, the diffraction angles around the lip of the shock tube exit will generally vary over a smaller range and, specifically, the very oblique diffraction angles will not occur for tubes where the axes are normal to each other though very shallow angles can be tested. In the cases considered here, the tubes were arranged to test the effect of vertical offset between the axes of the shock tube and exit surface. In the RR5 model, the centreline of the shock tube lies 1 diameter below the centreline of the exit surface. The result here is that the most upstream diffraction angle is 101.5° while the most downstream diffraction angle is 53.1°. By comparison, the RR3 test piece is set up such that the upper edge of the tube lies at the same level as the centreline of the exit surface i.e. with the shock tube centreline 1 radius below the exit surface centreline. This limits the upstream diffraction angle to 90° while the minimum diffraction angle is 48.19°. The third model will be dealt with separately in § 5.3.1.1.

The development of the flow field for each of the Mach numbers tested for the RR5 exit surface is shown in Figure 5.26. This model is considered first since the effects of the exit surface curvature will be lowest and it is most easily compared to the both the canonical normal exit of a shock tube and the inclined exit plane models due to the obtuse upstream and acute downstream diffraction angles. As for the inclined exit plane case, the selected flow field stages shown are: when the diffracted shock wave reaches approximately 1 and 2 tube diameters downstream; and then when the vortex ring formed at the exit of the shock tube has convected approximately 1, 2, and 3 tube diameters away from the exit plane. All measurements are taken along the level of the centreline of the tube and to either the front edge of the visible shock wave or the apparent centre of the thickness of the vortex. Where necessary, linear extrapolation is used to select the appropriate frame. The vortex ring is only partly visible when it has convected 3 tube diameters downstream because of the limits of the flow visualisation field of view. A selection of frames has also been annotated in Figure 5.27 so that the flow features can easily be identified.

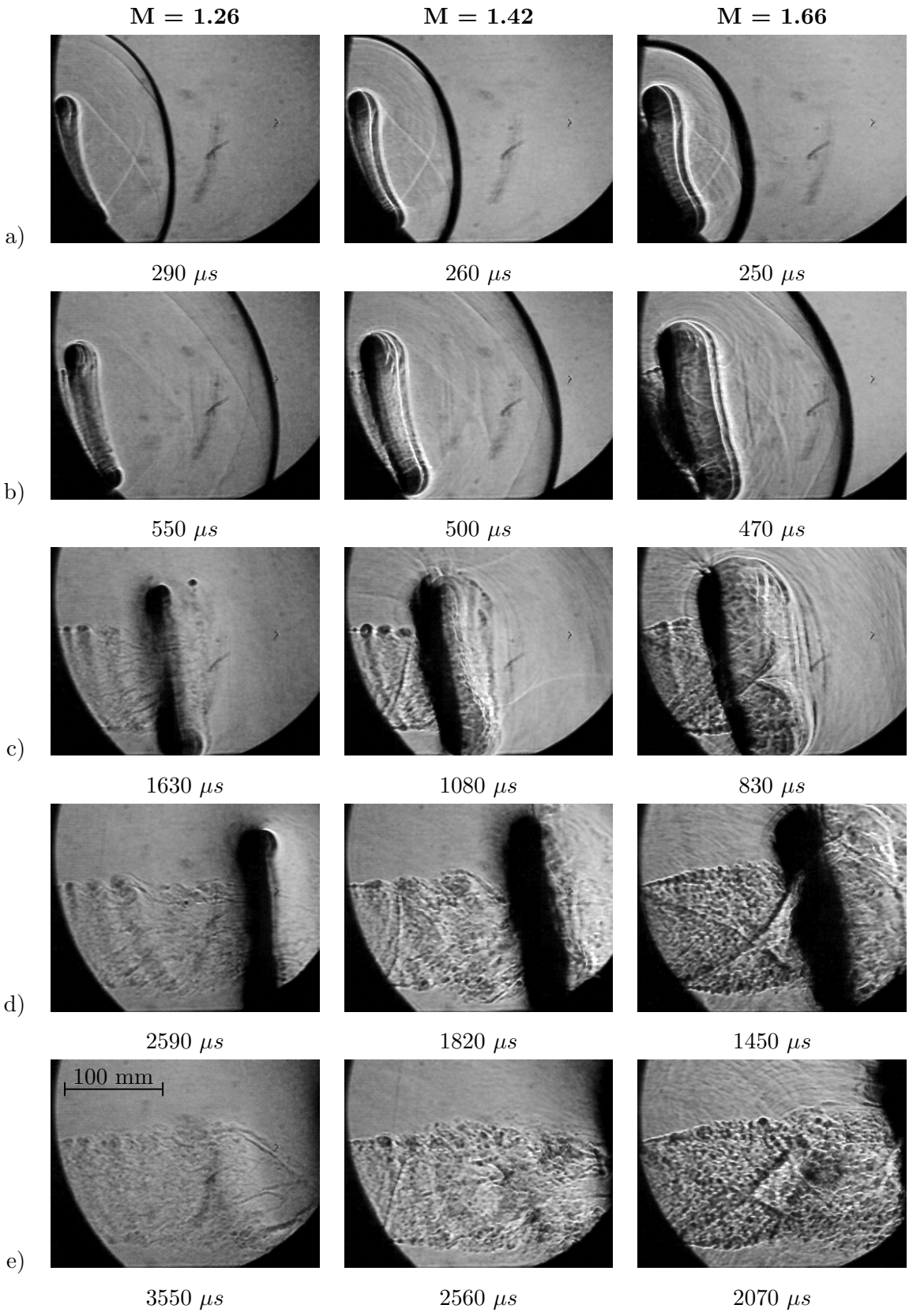


Figure 5.26: The flow field development for the exit of a shock tube with an exit radius ratio of 5 for Mach numbers of 1.26, 1.42, and 1.66

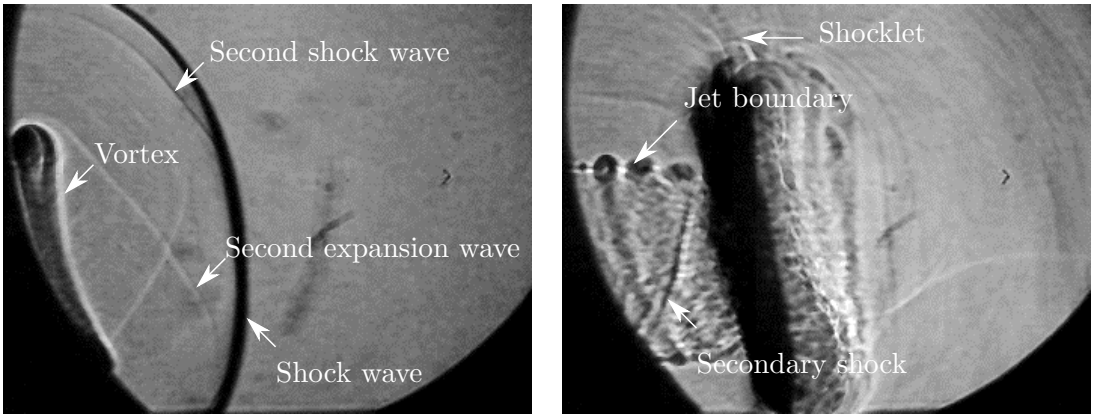


Figure 5.27: Annotated experimental images for the early (Mach 1.26 (*left*)) and later (Mach 1.42 (*right*)) flow field development

In the Mach 1.42 and Mach 1.66 cases, the induced shock wave within the vortex is evident as the bright white line and also shows curvature toward the exit surface centre. Again, it may be a toroidal shock wave, as identified in Kleine et al. (2009), rather than a shock wave covering the entire aperture of the vortex as suggested by Brouillette and Hébert (1997) because of the curved vortex profile and the variation of the induced velocity by different parts of the vortex loop due to varying strength. No matter the shape, this curved shock wave would cause the jet to widen in the upstream direction as it propagates and thus enhance the widening of the jet, especially at the upper edge, at least initially. This is similar to the widening of the jet seen in Zare-Behtash, Kontis and Gongora-Orozco (2008) though much less severe.

A more important feature to note is the apparent second shock wave following the primary front near the top of each frame, which is most clear for the Mach 1.26 case if Figure 5.26. As can be more clearly seen in the videos of this case (in Appendix B), this wave arises soon after the start of diffraction but while the incident shock wave front is still within the aperture of the exit and is stronger near the primary surface than near the top. The second expansion waves fronts seen in these images are also related to these shock waves.

This shock wave is caused by the fact that the exit surface curves toward the wave following diffraction. As the wave diffracts farther along the diffraction edge, the angle presented by the surface curvature increases and thus the second reflection formed at the surface is stronger than at the earlier diffraction points. As the incident shock wave strength increases, the strength of this wave increases and so it merges faster with the primary front than for lower Mach numbers.

Unlike the primary wave, which transitions from a plane surface to an approximately spherical shape and thus covers the entire aperture of the shock tube exit, the secondary shock wave

is actually two waves formed on each side of the aperture which will later merge into a single surface. These present as a single wave as the optical system can only show the tangent edges of these waves.

In Figure 5.26 frames b), it is clear that the profile of the vortex ring is already flattening under the effects of the different dilatation of the vortex line. Since these cortex rings more closely resemble those presented in Zare-Behtash et al. (2009) and especially those in Kambe and Takao (1971), one might expect the vortex to develop a curvature away from the exit surface at later times. This effect would be hindered by the higher convection speed of the upper portion of the vortex loop and thus it is clear that the effect of vortex line curvature is strong in changing the profile of the vortex in time. As evidenced in the plane exit surface cases, the vortex for the higher Mach numbers also convects faster downstream than that for the weaker incident shock waves.

In frames c) the vortex profile for each of the Mach numbers is almost plane and is increasingly upright. However, as the Mach number increases, the inclination to the vertical of the vortex increases. While the expectation is that the stronger vortex loops would turn upright faster, the spread and upward inclination of the under-expanded jet for the higher Mach numbers, and especially the Mach 1.66 case, would contribute to the inclination.

For the higher Mach numbers, the secondary shock waves are now apparent and comparable to that seen for shallower exit plane inclinations in the plane exit surface cases. For the Mach 1.42 case, the shallow interaction with the upper inner surface of the shock tube and the weaker expansion wave from the lower diffraction edge results in no visible secondary shock wave in the upper portion of the jet.

In comparison, strong secondary shock waves are visible in both the upper and lower portions of the jet for the Mach 1.66 case. While the upper shock wave originates only slightly within the shock tube, the lower portion clearly originates some distance upstream of the diffraction lip. Once again, as in the inclined exit case, this conical shock wave meets near the axis of the jet but there is no evidence of Mach reflection here apart from in frame c) where a shear layer can be seen downstream of the reflection point.

At this time there is also a series of induced vortices on the jet boundary which are being entrained around the primary vortex periphery through the vortex aperture, as seen in Kleine et al. (2009) and similar to those suggested by Murugan and Das (2010) for a KHI. However, unlike in the canonical case, this seems to be causing some narrowing of the jet especially near the upper edge in the Mach 1.42 case. The precise mechanism of this is unclear but it may also explain the breakdown of the upper surface of the jet seen particularly for weaker incident shock waves in the inclined exit plane cases.

Also visible at this time for the Mach 1.42 and Mach 1.66 cases is clusters of induced shock waves at the upper vortex boundary. While these were identified in Jiang, Takayama et al. (1997), the shocklets seen here present as a cluster because of the differing points around the vortex periphery at which the shocklet forms due to the induced supersonic flow. This is exacerbated by the turbulence in the vortex periphery entrained from the jet boundary and hence the appearance of clusters of shocklets rather than a single, clear shocklet. In fact, the shocklets appears to move around the vortex periphery in the downstream direction as shown in the videos in Appendix B. Since the vortex ring curves in multiple directions and the optical system only shows the tangent edges of phase objects, identifying the precise location of each shocklet is impossible from the experimental images.

In Figure 5.26 frames d), these counter-rotating vortex rings (CRVRs) have seemingly stopped and the jet boundary now resembles the steady jet boundary seen in the plane exit surface cases. As expected, given the low inclination of the mean exit surface (less than 30°), the jet is not inclined significantly upward though there is still some inclination of the jet for the Mach 1.66 case. The primary vortex is also plane and almost vertical in profile in all cases.

Finally, at late times (frames e)) the jets resemble the late-time jet for the shallow inclined plane exit cases. An interesting difference is that the secondary shock waves weaken as time passes for this configuration though there is no fundamental difference in physical properties that should cause this apart from exit surface curvature. Also, in all cases, the jet seems to break down into turbulence immediately downstream of the intersection of the reflected secondary shock waves with the jet boundary, with a narrowing of the jet as well. This is likely an effect of the vortex, which is still quite close to the exit surface at only 3 tube diameters downstream, and the effect would be absent at very late time.

The results for the RR3 exit surface are presented in Figure 5.28. While the development of the flow field is similar to that of the RR5 surface, a few points of interest stand out. First, the initial vortex as seen in frames a) shows an even greater initial curvature in profile and greater tapering. This is expected given the greater surface curvature and the greater difference in age of the upper and lower limits of the vortex ring because the longitudinal separation of the diffracting edges is double that for the former case.

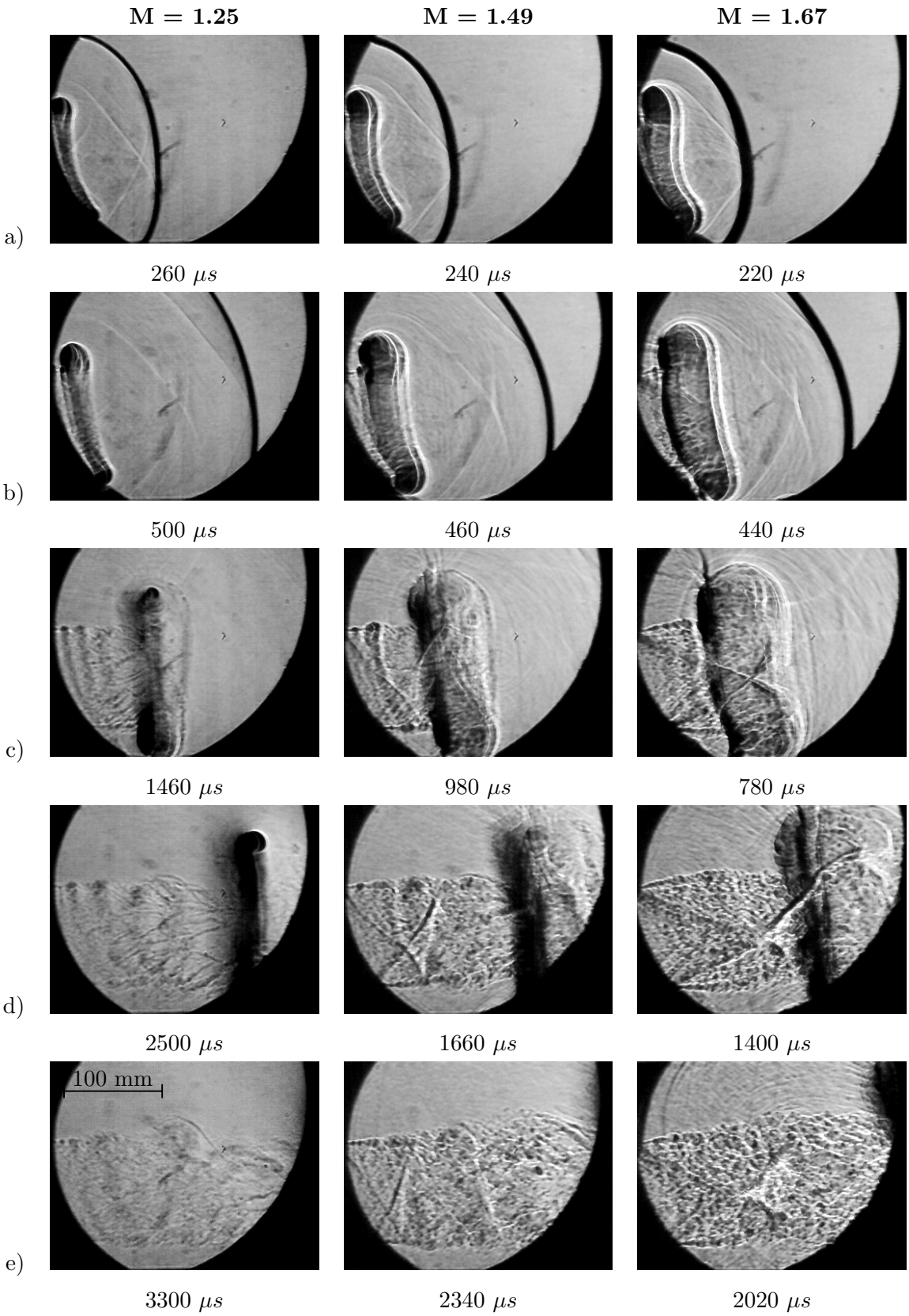


Figure 5.28: The flow field development for the exit of a shock tube with an exit radius ratio of 3 for Mach numbers of 1.25, 1.49, and 1.67

Here again the second shock wave following the primary wave front is present but seems to be weaker than in the RR5 case. This is contrary to expectations given the more rapid steepening of the curved exit surface for due to higher curvature and will require further interrogation. However, as in the previous case, it quickly merges with the primary shock wave and does not seem to affect the vortex to any significant extent.

The flattening of the vortex profile occurs over similar time scales to that for the shallower exit surface curvature for each Mach number though with the distinction that there is a thickening of the vortex cross section near the centreline of each vortex. This is likely an effect similar to that seen in Skews and Reeves (2012) due to the higher curvature of the vortex filament here than at other azimuthal positions.

Despite this, the vortex is almost plane and vertical by frames c) for all Mach numbers. In these frames it is also clear that there are induced shocklets around the upper vortex periphery in at least the Mach 1.67 case, though there is some evidence of these in the Mach 1.49 image. Also noticeable here are the secondary shock waves emanating from within the shock tube, similar to those indicated in Figure 5.27, and the fact that the upper surface of this for both Mach 1.49 and Mach 1.67 is quite clearly visible. While the upper portion of each resembles a steep compression fan, the lower portion of each is clearly a shock wave. Again, as noted for the RR5 case, the secondary shock waves weaken with time and are almost indistinguishable from the turbulence in the jet boundary as time progresses. It is clear in these final frames d) and e) also that the jet shows no significant upward inclination, as would be expected given a mean inclination of only around 20°, though there is some significant spreading due to under-expansion for the Mach 1.67 case in frame c).

5.3.1.1 Tangent exit

As in the consideration of a plane exit surface, the effects identified would be expected to be more extreme as the limits of the diffraction angle become more extreme. Given the combinations of geometries, the maximum mean exit surface inclination that can be encountered would occur when the inner surfaces of the shock tube and the exit surface are tangent. This would specify a minimum diffraction angle of 0° at the downstream edge i.e. no diffraction whatsoever. The diffraction angle at the upstream edge will increase with increasing radius ratio. In the limit of infinite radius ratio this would represent a variation from an upstream diffraction angle of 180° to 0° at the downstream end. However, for more practical radius ratios, such as those considered here, the upstream diffraction angles would be 109.4° and 126.9° for radius ratios of 3 and 5 respectively. While the overall mean inclination would be higher for the RR5 case, the greater curvature of the exit surface in the RR3 case

was deemed more interesting as a limiting test case because the diffracted wave would be reflected back into the test section sooner.

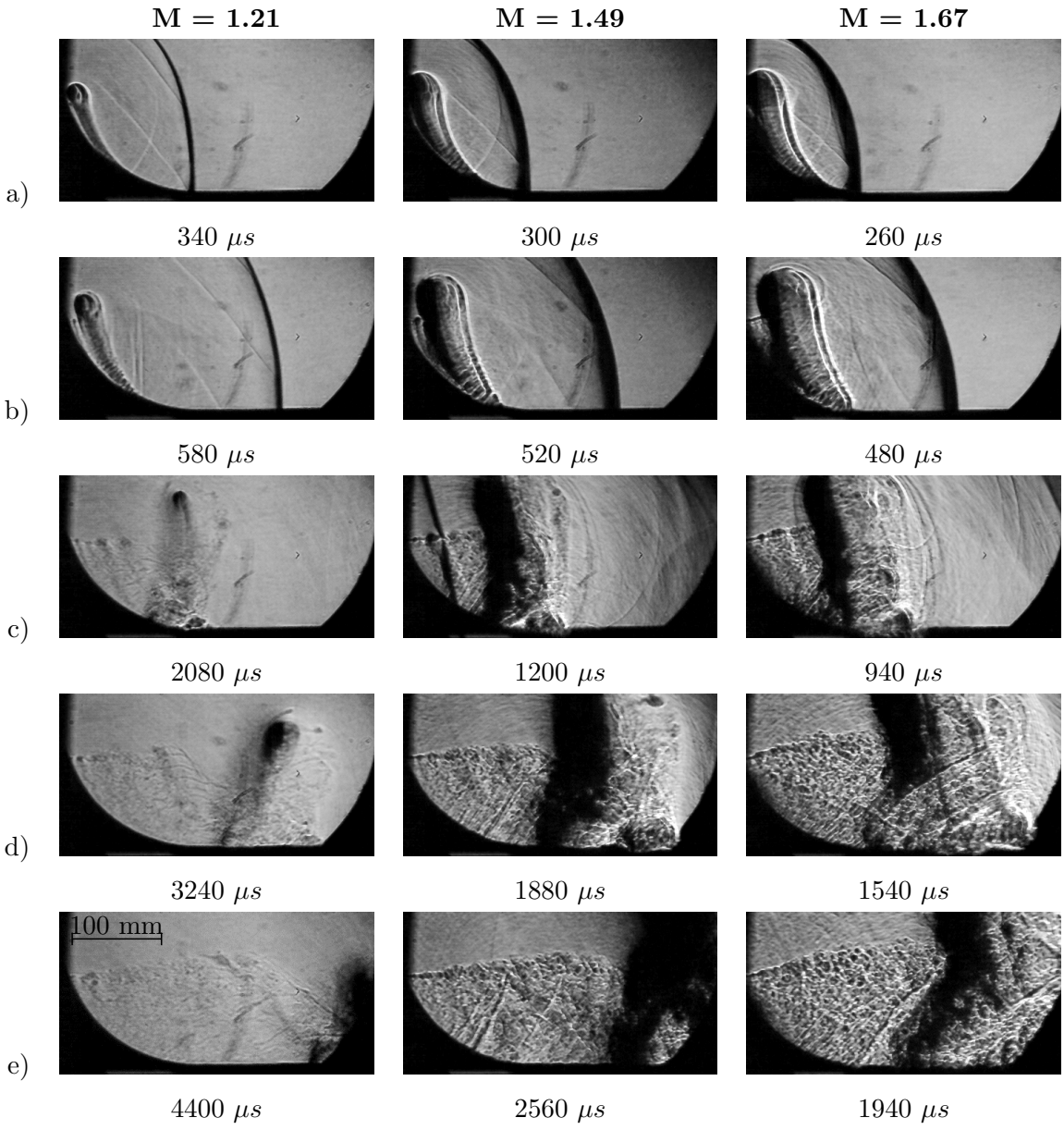


Figure 5.29: The flow field development for the exit of a shock tube with an exit radius ratio of 3 and tangent exit surface for Mach numbers of 1.21, 1.49, and 1.67

While the geometry in the case of two intersecting ducts would have the far edge of the exit surface tube rising up immediately at the downstream edge, it was decided to extend the exit surface of the tangent radius ratio 3 model with a plane surface to examine the propagation of the vortex. This is especially necessary since it is unclear if the vortex would even form a closed loop, failing which it would by physical necessity terminate in the surface. As in the inclined exit case, it is expected that the flow field developed will resemble something

between plane surface diffraction and a free jet. This configuration more closely resembles an exhaust adjacent to a surface, such as may happen with a supersonic propulsion engine.

Initially, the flow field is similar to that expected considering the previous results, in that the vortex, shown in Figure 5.29 frames a), is initially curved similarly to the exit surface. However, unlike in the previous cases and similarly to the results in § 5.2.1.4, the vortex tapers to zero diameter at the downstream edge of the shock tube exit since there can be no vortex shed on the tangent surface.

As the flow field develops the counter-rotating vortices seen in earlier tests are present on the upper surface of the jet, visible especially in the Mach 1.21 case in frame b). The vortex also shows the rapid shift toward a plane profile and vertical orientation seen earlier. However, almost immediately, and as can be seen in frames c) of Figure 5.29, the lower portion of the vortex begins to break down. It appears that the vortex terminates in the exit plane and entrains fluid upward in a helical fashion from a spread foot. As this propagates forward, the top of the vortex arch (since it has not closed to form a loop) easily catches up to the foot and even seems to overtake it somewhat.

The top portion of the vortex then moves toward the plate and the vortex line breaks rapidly down into turbulence, constricting the jet along with it. Once again for the under-expanded flow exiting the shock tube because of the Mach 1.49 and Mach 1.67 incident shock waves, the interaction of the expansion fan formed at the top of the diffracting edges causes a shock wave to form in the lower portion of the jet at the inner surface of the shock tube. This shock wave is indicated in Figure 5.27 and can be more clearly seen in the videos in Appendix B. Additionally in the Mach 1.67 case a compression in the upper portion of the jet is visible, though it is most clearly seen in the videos. Since no expansion wave can form at the downstream limit of the diffraction edge because it is tangent to the exit surface, this confirms that the complex reflection of the expansion wave formed at other azimuthal positions from the upper inner surface of the shock tube gives rise to this secondary shock wave.

5.3.2 Computational Fluid Dynamics

The flow field observed in the RR3 and RR5 cases described above were similar enough to the canonical case, and the low inclination angle exit plane results, that additional computational fluid dynamics (CFD) was not deemed necessary. In contrast, the behaviour especially of the vortex in the tangent exit surface case warranted computational modelling to definitely resolve the development of the vortex line formed by diffraction at that exit. Given the high-level similarity between the flow fields, the computational model for the curved exit surface was

set up using the same general philosophy as the inclined exit plane as described in § 5.2.2. The domain was again divided into three principal regions, as shown in Figure 5.30, though the overall volume was smaller due simply to the more compact exit surface. The domain was meshed using the same sizing functions applied as for the inclined exit case and the resulting initial mesh comprised approximately 12 million tetrahedral cells, with 70% of those of a quality between 0.87 and 0.96.

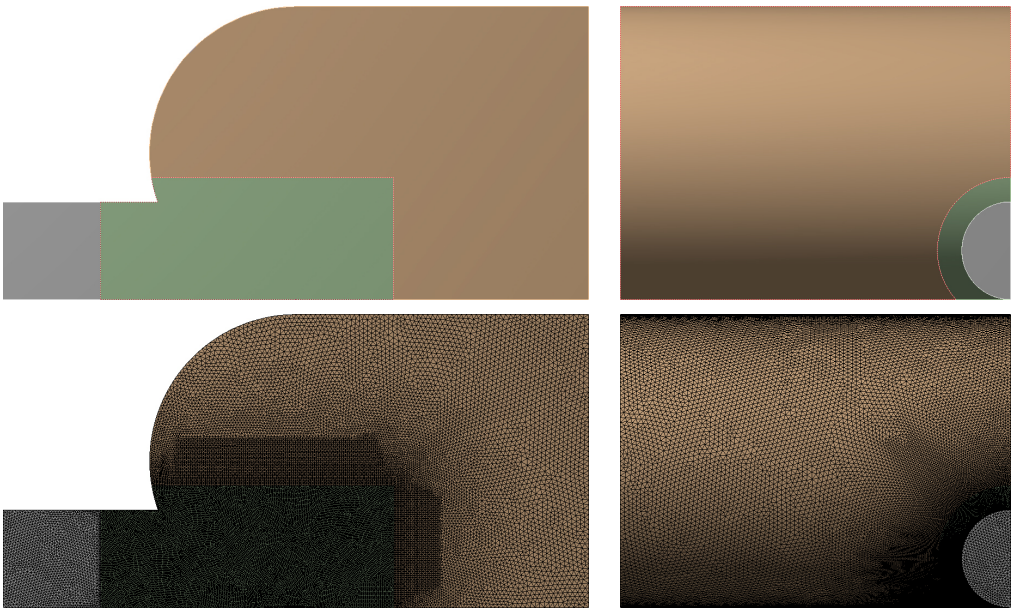


Figure 5.30: Geometry (*top*) and mesh (*bottom*) for shock diffraction at the curved exit of a shock tube tangent to the exit surface. The view of the domain in elevation of the symmetry plane (*left*) and looking in the direction of shock wave travel (*right*) are given

5.3.2.1 Model validation

The results of the computational modelling were validated by direct comparison of features at key time points in the flow. The uncertainty due to the estimation of the initial diffraction time in the experiments was approximately 5 μs and, including this, the final error between the CFD and experimental data was less than 2% for the shock wave position though it was around 15% for the vortex position for the Mach 1.21 case decreasing to less than 5% for the Mach 1.67 case. These comparisons are shown in Figures 5.31 to 5.33.

Looking first at the Mach 1.25 data in Figure 5.31 the agreement for the shock wave position is visually good but there is a stark difference in vortex position although the shape is similar. The primary causes for this are: the uncertainty in the precise moment of first diffraction for the experimental and CFD results, both of which were estimated visually; and the difference in Mach number.

Supposing that the actual zero time for the experimental case was later than that estimated by selecting a nominal zero-time frame and similarly the actual zero time in the CFD images was earlier than that estimated, then the difference in age of the vortex between the two models would be exaggerated and increase the difference between the two images. Considering the difference in actual Mach number for the Mach 1.25 data, the incident shock wave experimentally was only approximately 3% weaker but the vortex strength increases non-linearly with incident Mach number.

Thus, the vortex in the CFD would be significantly stronger and thus farther advanced than in the experimental case. The modelling of the induced CRVRs in the final frame suggests that the geometric differences between the models may appear large but that the fundamental physics for the approximate Mach number range have been accurately captured.

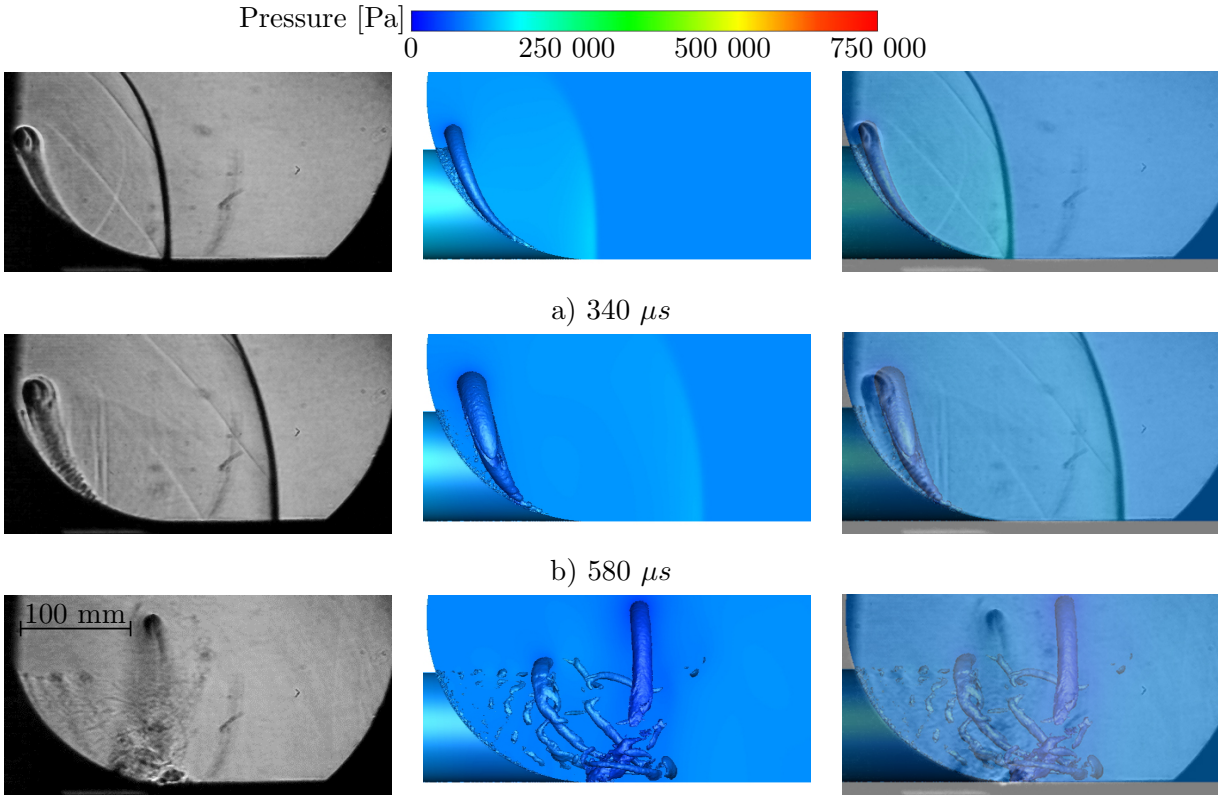


Figure 5.31: Comparison of the experimental and computational images for the Mach 1.21 (experimental) / Mach 1.25 (numerical) case. A direct overlay of the computational and experimental results is given at the far right

Looking at the Mach 1.4 case in Figure 5.32 the accurate correlation of the shock waves is again clearly evident in the first frames. As would be expected since the actual experimental Mach number was higher than the modelled one, the separation between the numerical and experimental shock waves, where the former is initially farther downstream than the latter,

decreases as time advances. Again the initial vortex profile is similar but the position is significantly different. This continues to late time though the error between the centreline position of the vortices decreases as time advances. Here, in frame c), it is also clearest that the vortex visualised using the λ_2 method appears much thinner at late times. The isovalue of λ_2 selected was selected to specifically produce vortex tubes comparable to those seen experimentally for lower Mach numbers. However, since only one value of λ_2 was used for clarity, the vortex tube appears thinner in the CFD results than in the experimental for later times because of the spreading and growth of the vortex ring because it visualises a region near the vortex core and will not encompass the regions with higher λ_2 farther out from the vortex filament which can be seen in the schlieren images.

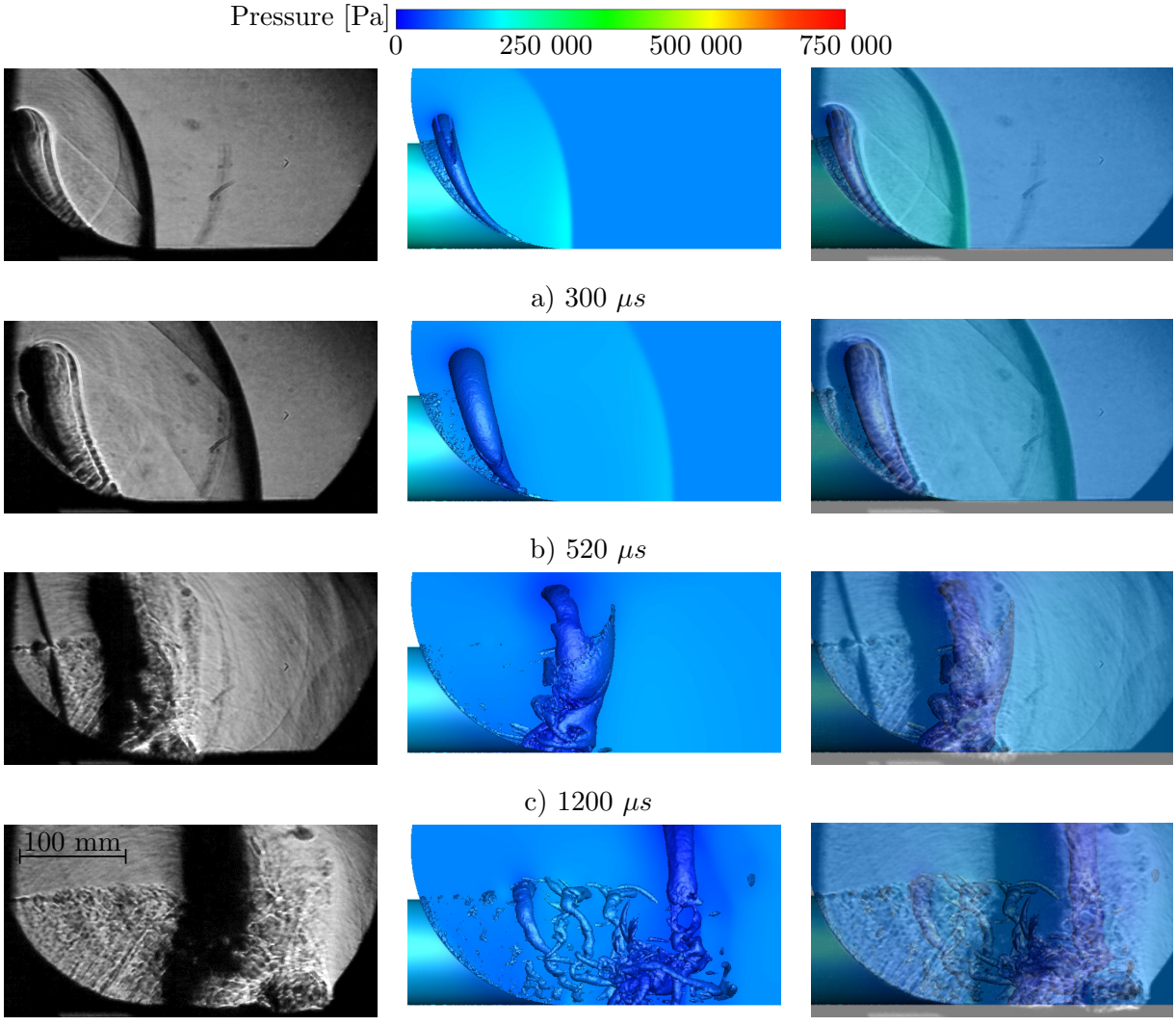


Figure 5.32: Comparison of the experimental and computational images for the Mach 1.49 (experimental) / Mach 1.4 (numerical) case. A direct overlay of the computational and experimental results is given at the far right

The results for the Mach 1.6 case in Figure 5.33 also show good correlation despite the difference between the experimental and modelled Mach numbers. In frames a) and b) it is clear that the faster experimental wave catches up with the slower computational one. The secondary shock wave observed immediately behind the primary shock wave front is not visible and must therefore be a feature outside of the symmetry plane of the shock tube. This confirms the hypothesis that it is as a result of reflection of the deflected wave outboard of the centreline. This would also explain the lack of change of slope of the primary wave at the apparent interaction in the experimental schlieren images since that technique can only visualise the tangent edges of a phase object and the deformation of the primary shock wave front by the secondary wave would be away from the centreline and thus not produce additional tangent edges in the primary wave.

As in the previous cases, there is a difference in the position of the experimental and computational vortices, though the shape is again similar and the error is lower than for the lower Mach numbers. In frame c) the computational vortex shows superficial similarity to the computational one, though it is more upright. Since it has been observed that the vortex for a weaker incident shock wave deforms to an upright position faster, it is understandable that the computational vortex will have become more upright in comparable time. Of greater interest though in frame c) is the expansion wave evident on the centre plane centred on the upper lip of the shock tube, as expected for an under-expanded jet.

This expansion wave also explains the shock wave seen at the lower edge of the jet especially in frame e) of the experimental series. Considered only on the central plane, the expansion wave will induce the flow to upward, away from the tangent plate. However, at the tangent exit surface this would violate the continuity of mass and so a shock wave develops at the plate surface to bend the flow back parallel to the exit tangent surface. Although obscured slightly by the vortex tubes in frames d) and e), the rise in pressure associated with this shock wave can be seen in the computational frames for those times. Given the varying shock wave strength around the shock tube exit lip as a result of the influence of the propagation along the shock wave surface of expansion waves related to earlier diffraction, the exact shape, orientation, and strength of both the expansion and shock waves at the shock tube exit cannot be simply assessed. However, the disruption of the boundary layer on the tangent exit surface by the induced shock wave will be a source of additional turbulence and would explain the breakdown of the jet at late times.

As for lower Mach numbers, the vortex arch shows evidence in the computational results (especially in the videos) of terminating in the exit tangent surface and inducing flow upward toward the apex of the arch. The induced CRVRs in the jet periphery are also being entrained into the vortex as it grows while it is becoming increasingly turbulent.

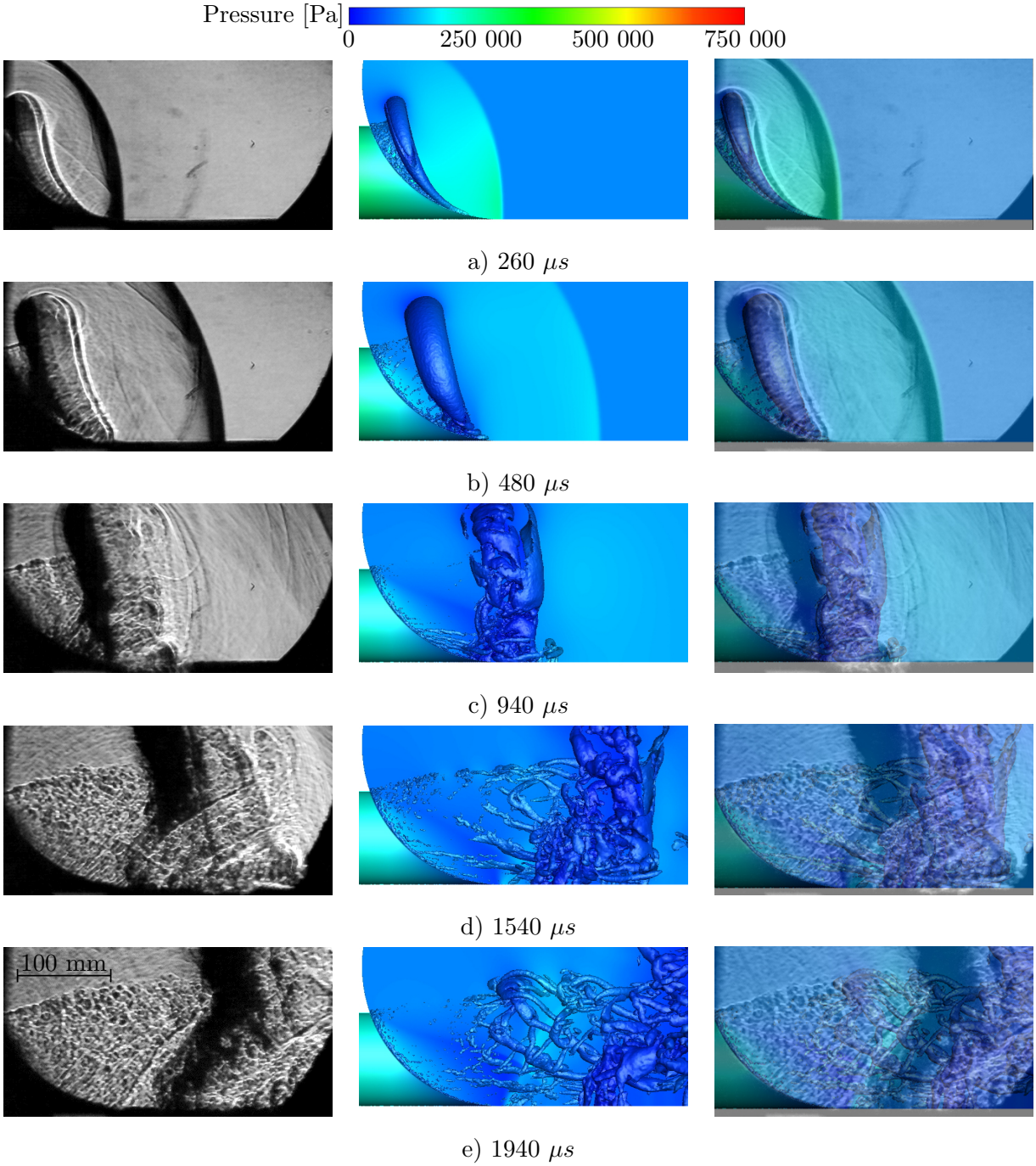


Figure 5.33: Comparison of the experimental and computational images for the Mach 1.67 (experimental) / Mach 1.6 (numerical) case. A direct overlay of the computational and experimental results is given at the far right

5.3.2.2 Further results

In order to better understand the vortex dynamics, isometric elevations of the development thereof have been presented in Figures 5.34 and 5.35 . Considering first the development for the lower Mach numbers of 1.25 and 1.4 shown in Figure 5.34, the vortex development at

early times is exactly as would be expected: a smooth, stable vortex loop which forms at the upstream diffraction edge tapering to a vortex of zero thickness at the tangent surface. From as early as frames b) it is clear that the seeming free ends of the vortex loop are turning to meet the surface normally and acting as sources of turbulence in the rest of the vortex.

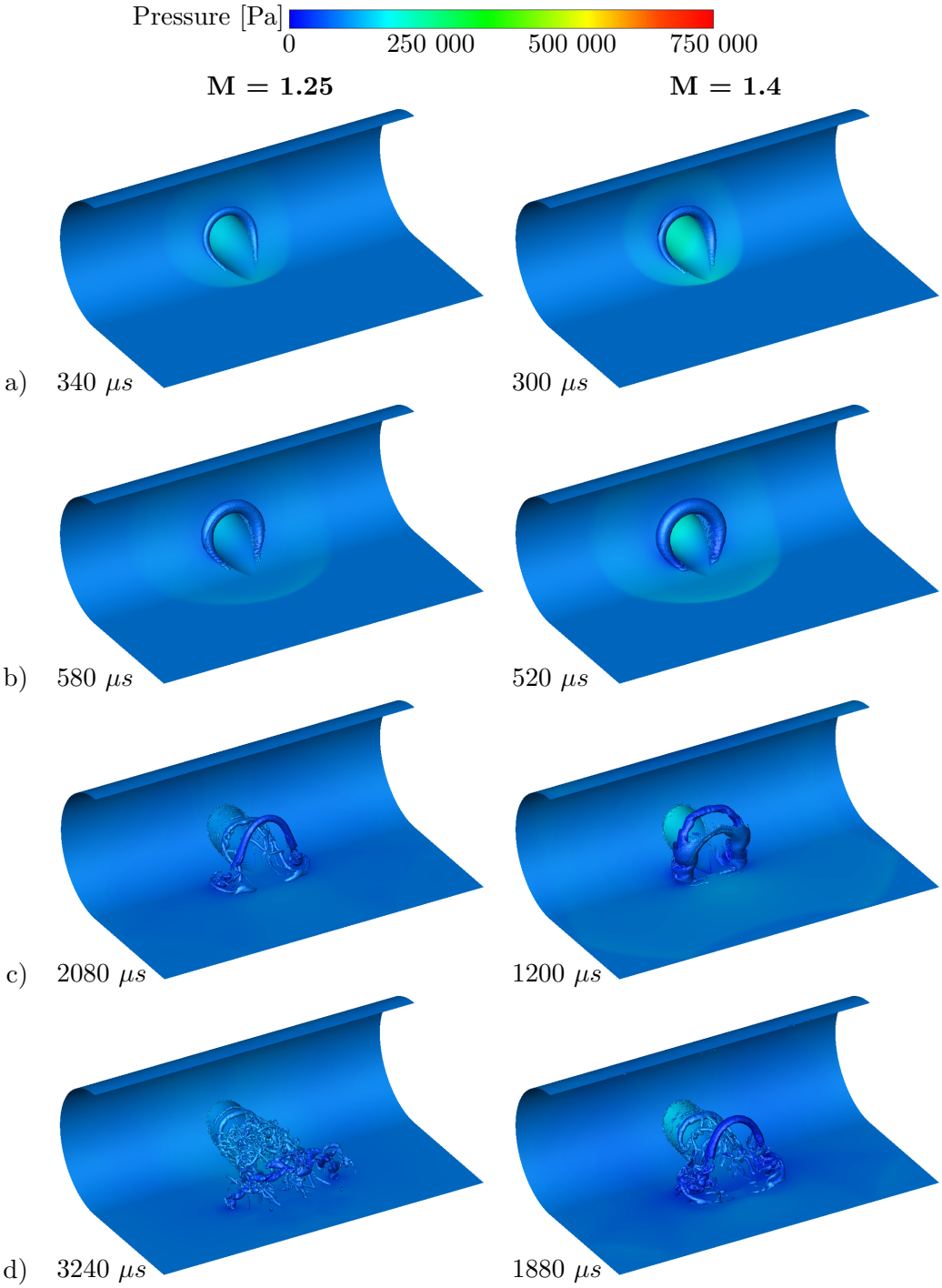


Figure 5.34: The computational vortex development for the exit of a shock tube with an exit radius ratio of 3 and tangent exit surface for Mach numbers of 1.25 and 1.4

In frame c) of the Mach 1.25 case, the vortex loop meets the tangent exit surface normally and there are also filaments of the induced CRVRs entrained near the feet of the vortex. Since these vortices also do not form closed loops, it would be more appropriate to use the term counter-rotating vortex line (CRVL) to refer to these. It is also noticeable that the vortex arch is flattening and spreading laterally with the breakdown near the surface. By comparison, the vortex arch for the Mach 1.4 case is still quite curved and strong enough to entrain induced CRVLs of its own.

In the final frame of the Mach 1.25 series the vortex arch has almost entirely decayed to turbulence and the jet is spreading across the exit tangent surface. This suggests again that these vortices are part of the manner in which the vorticity sheet of the jet boundary layer is spread to form an open flow as time develops. In comparison in the Mach 1.4 case, the decay of the vortex through entrained CRVLs and induced turbulence is comparable to that at earlier times for the Mach 1.25 case, confirming the stabilising effect of the higher momentum of the jet on the upper portion of the primary vortex ring. However, the lower portion of the vortex ring will be destabilised by the lower portion of the flow and the vortex arch is also spreading and becoming more turbulent.

Since the vortex filament has not closed into a loop it must terminate in the surface as seen here. However, the portions of the primary shock wave which diffracted at the lower edges of the shock tube exit will have induced outboard flow from the centreline. This flow is going to push the feet of the vortex arch outward. This stress along the vortex filament will pull the upper portion of the vortex down and result in the lowering of the upper edge (or thinning) of the jet seen in the experimental images. This effect will be more pronounced for lower Mach numbers since the stretching of the weaker vortex line there will cause greater deformation thereof.

Considering now the initial development of the vortex for higher incident Mach numbers of 1.6 and 2.2 as shown in Figure 5.35, the initial development of the vortex loop follows that for the weaker shock waves closely. The primary difference here is the faster transition to a turbulent foot near the exit surface of the vortex arch. This is especially noticeable in the Mach 2.2 case. This disruption would be enhanced by the presence of the strong induced shock wave within the vortex loop, evidenced by the jump in pressure at the surface between the two legs of the arch in frame c) of that series. Interestingly, the induced shock wave seems to form a convex surface (looking from downstream up the shock tube) in frame b) of that series. This would induce strong outboard flow near the surface contributing to the destabilisation of the foot of the vortex arch. This shock wave would have been obscured by the high gradients within the vortex aperture and core in the experiments could they have been run. There is some evidence of a similar shock wave in the series for Mach 1.6 though

it is naturally much weaker than in the Mach 2.2 case since the post-shock flow there is subsonic.

The flattening of the vortex arch for the Mach 1.6 case under the influence of the outboard flow is clear in frame d) and the vortex arch is breaking down into turbulence in frame e). By comparison, the arch for the Mach 2.2 case shows signs of flattening in frames d) and e) of that series but otherwise seems to remain quite coherent despite the stress of the outboard flow on the feet of the arch. The vortex is, in fact, strong enough that a CRVL of similar coherence is induced downstream of the embedded shock wave and is travelling around the periphery of the primary vortex.

The flattening of the vortex is thus also shown to be the mechanism by which a shock-induced jet along a surface transitions from a free jet at the upper surface to a turbulent flow along the plate surface. Unlike in the case of the Mach 2.2 shock wave diffracting from the 75° inclined exit place there is no sign that the vortex arch for the Mach 2.2. case here might close into a loop. This additionally suggests that there exists a limit in exit surface inclination at the downstream edge between 0° and 15° for which there is the possibility of closing a vortex loop regardless of incident shock wave strength.

One final point which should be made about the pressure contours on the exit surface in the Mach 2.2 is the presence of drops in pressure at the lateral and downstream edges of the domain. These would correspond to the expansion waves which would propagate back into the flow field when the diffracted shock wave reaches the edges of the exit surface test piece and is the reason for stopping the simulations at these times (obviously different for each incident Mach number). In the case of a long exit duct surface, these expansion waves would not occur.

Returning to the issue of the embedded shock wave the centreline pressure contours in Figure 5.36 provide interesting insight though detailed visualisation of the complex surface shape proved impossible. In frames a) through c) the early development of the embedded shock wave is shown. Initially there is only the shocklet within the vortex that extends to the boundary of the vortex core that is visible but this grows (frame b)) to extend inside the jet. There is a discontinuity here because of the high speed of the flow within the jet causing the shock wave to curve forward there.

In frame c), the first evidence of the induced shock wave on the tangent surface between the feet of the vortex arch becomes visible. This would explain the sharp v-shape of the embedded shock wave against the tangent exit surface in frame b) of Figure 5.35 since the embedded shock wave grows from the vortex core, as identified in Kleine et al. (2009).

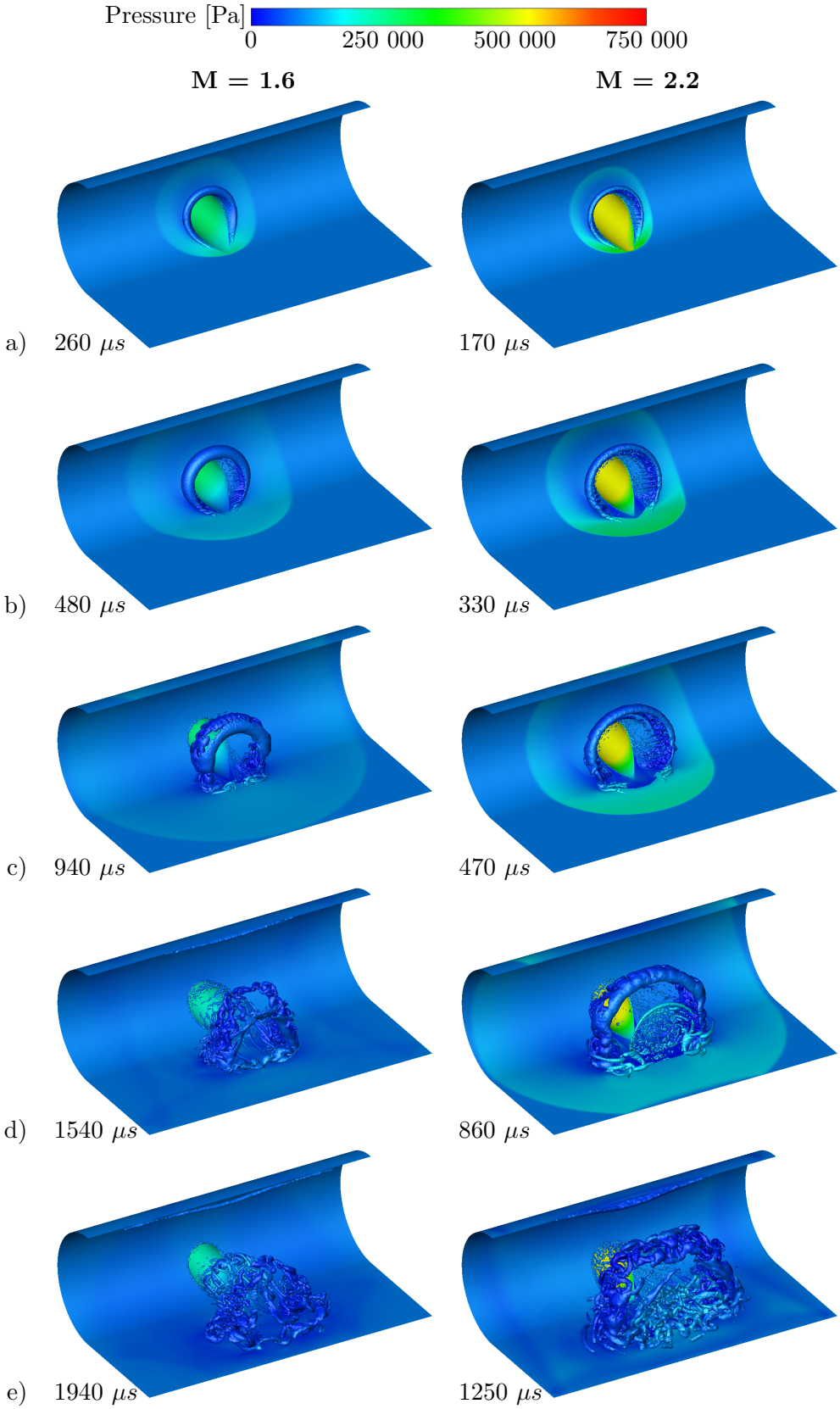


Figure 5.35: The computational vortex development for the exit of a shock tube with an exit radius ratio of 3 and tangent exit surface for Mach numbers of 1.6 and 2.2

By frame d) of Figure 5.36, the toroidal shock wave surface has closed to form a shock wave covering the entire cross-section of the jet. As in the case of the conical shock wave reflection flow discussed in § 5.1, this shock wave is curved toward the downstream direction by the momentum of the jet which gives the shock wave a pronounced 'double-bubble' shape at the centreline (because of similar forward curvature of the outer portion of the shock wave inside the vortex). While the major portion of the shock wave within the jet is bowed outward by the jet flow, the compressions or shock wave formed where the expansion wave from the upper lip of the tube meets the tangent exit surface bend the flow parallel to the surface and so the embedded shock wave remains normal to the exit surface. There is no reflected wave from this interaction or else it is too weak to be discerned here.

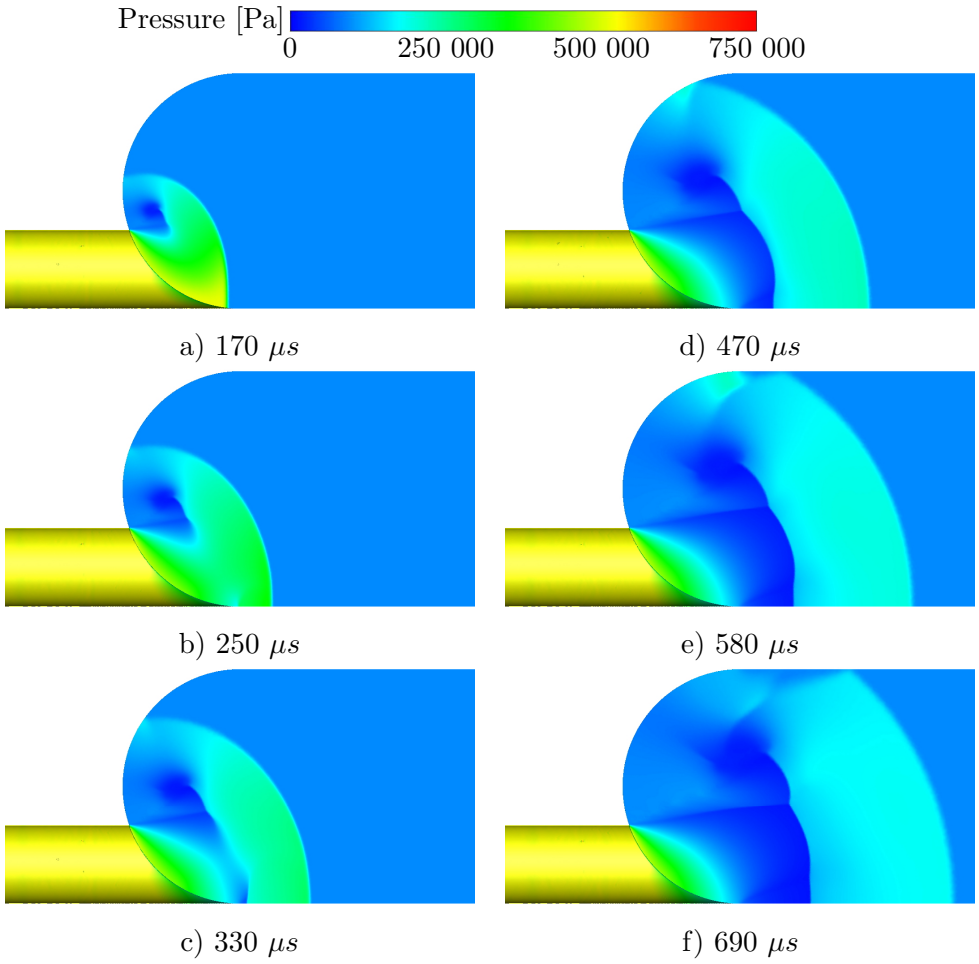


Figure 5.36: The computational symmetry plane pressure development for the exit of a shock tube with an exit radius ratio of 3 and tangent exit surface for Mach 2.2

As the flow field develops further over time, the curvature of the embedded shock wave decreases due to the spreading of the jet and lower velocities on the entire shock surface moves upstream (relative to the position of the vortex) farther into the vortex aperture. It

is immediately downstream of this embedded shock surface at the jet boundary that the secondary vortex arch identified earlier is induced.

Another feature to note in frames d) through f) of Figure 5.36 is the reflection of the diffracted incident shock wave surface from the curved exit surface. At the time shown in frame d), the reflection of this weak wave is regular. Immediately after this it will diffract over the virtual edge of the exit surface (since the boundary of the domain changes from a wall to a press outlet type at the top of the semi-cylindrical surface) and the effect of the expansion wave generated by that expansion propagating back into the flow can be seen in frames d) and e).

5.3.3 Summary

The most significant effect on the diffracted shock wave geometry in the case of a curved exit surface is that the curvature of the surface toward the diffracted shock wave results in a trailing shock surface behind the primary diffracted wave front. This shock wave quickly merges with the primary front but the limited visualisation thereof available suggests that it has a complex overall shape and the precise manner of formation warrants further study.

As with the diffraction of a plane shock wave from an aperture with a plane inclined exit, the jet emanating from the shock tube following the diffraction of a plane shock wave from a shock tube with a curved exit surface is inclined away from the exit surface. This inclination increases with Mach number of the incident shock wave and decreasing radius ratio.

It is helpful to consider the mean inclination of the exit defined between the most upstream and downstream edges of the exit aperture when analysing the dependence of the jet inclination on the radius ratio. Due to the practical limits of radius ratio, the mean inclination will generally be less than for the plane exit case because the radius ratio must be very high (greater than 5) to reach angles approaching the limiting case studied for plane inclined exit surfaces. Also, due to the nature of cylindrical geometry, the range of diffraction angles around the aperture will be smaller. Thus the overall jet inclination would be more limited in the case of curved exit surfaces than for inclined exit case.

As for moderate exit plane inclination, the expansion fan formed at the upstream diffraction edge interacts with either the interior of the shock tube near the downstream limit of the aperture or the exit surface and causes secondary shock waves. Again, the complex shape of the diffraction aperture means that this interaction and formation is complex. The most significant difference for the curved exit case is that the most upstream diffraction edge will typically not be at the top of the tube (as viewed in the images in § 5.2) but rather near the centreline of the tube. Depending on the radius ratio, this means that the vortex is strongest

near the centreline due to the high curvature there and this contributes to the vortex loop convecting into a plane elevation.

The most significant effect here is in the case where part of the diffraction aperture has a very shallow diffraction angle. In the case tested here of a tangent exit the result was the same as that for the inclined exit case, namely the formation of a vortex arch rather than a closed vortex loop. The vortex arch formed for diffraction from a curved exit aperture rapidly convects into an elevation and orientation similar to the canonical diffraction. The weak portion of the vortex arch terminating in the tangent exit surface contributes to the loss of coherence of the rest of the arch though the vortex arch here is more stable than that for the inclined plane exit at similar Mach numbers due to the easy formation of an orthogonal termination of the vortex line.

While the vortex loop for general curved exit diffraction behaves very similarly to the canonical vortex ring, the vortex arch formed for tangent curved exit widens and flattens as the flow develops before breaking down into smaller structures. Thus the effect of the loss of coherence of the vortex arch as a mechanism by which a jet flow is transformed into a diffuse flow over a surface is confirmed.

Chapter 6 Conclusion

The flow fields developed behind shock waves diffracting from non-orthogonal apertures show great similarity to the canonical cases studied to date but also present an array of new features for consideration and verification. The diffraction of a conical shock wave and the reflection of secondary shock waves following the diffraction of plane shock waves from inclined and curved exit apertures has showed that weak reflections of conical shock waves can appear on first observation to violate fundamental physics and form regular reflections. However closer inspection reveals that this is not the case but that careful consideration of scale and development in time are needed when interpreting such flow fields.

The diffraction of the conical shock wave has also provided the first evidence of the conical, compressible Kelvin-Helmholtz instability (KHI) and a novel form of conical shock wave reflection, termed the vn-Type for its similarity to the von Neumann reflection of weak waves, has also been identified. While it is conceptually simple to extend the original definition of the KHI to an axisymmetric form, the details of the stability and growth thereof will be fundamentally different from the two-dimensional case because of the change in transport properties with increasing distance from the axis. This feature in particular warrants further computational and possibly experimental verification.

The study of the diffraction of plane shock waves from oblique exits has highlighted one possible physical mechanism whereby the post-shock flow from a duct will transition from a free jet to a diffuse flow over the surface, namely the vortex arch. This structure forms when a closed vortex loop cannot form because of very shallow, if any, diffraction of the shock wave at the downstream edge of the aperture. This has potential implications for and applications in the design of systems with near-surface jetting and especially for the role that the induced vortex and the breakdown thereof plays in this transition, since the termination of the vortex arch in the exit surface seems to be a source of loss of coherence for the remainder of the vortex line.

All three studies have pointed to mechanisms by which the direction of compressible jets can be either statically or dynamically adjusted. In the case of the diffraction of conical

shock waves, the suggested mechanism is by the means of upstream occlusions of the flow to introduce momentum deficits in some part of the jet. This could be used for dynamic jets or to dynamically actuate steady jets. In the case of diffraction of shock waves from inclined or curved exits, the jet is inclined away from the inclined surface though this inclination decreases with time. However, both of these fundamental mechanisms have the potential for application in the design of industrial jetting systems. Further work especially on dynamic manipulation of steady gas jets or the shaping of steady jet exhausts could yield significant benefits in terms of efficiency and capability for these systems.

Bibliography

Abe, A., M. Watanabe and K. Suzuki (1992). 'Three dimensional flow structure behind a shock wave discharged from a rectangular cross section shock tube'. In: *Shock waves; Proceedings of the 18th International Symposium on Shock Waves*, pp. 209–212. DOI: 10.1007/978-3-642-77648-9_27.

Apazidis, N., M. Kjellander and N. Tillmark (2013). 'High energy concentration by symmetric shock focusing'. In: *Shock Waves* 23.4, pp. 361–368. ISSN: 09381287. DOI: 10.1007/s00193-013-0442-y.

Auerbach, D. (1988). 'Some open questions on the flow of circular vortex rings'. In: *Fluid Dynamics Research* 3, pp. 209–213.

Auerbach, D. (1991). 'Stirring properties of vortex rings'. In: *Physics of Fluids* 3.5, pp. 1351–1355.

Baird, J. (1987). 'Supersonic vortex rings'. In: *Proceedings of the Royal Society of London* 409.1836, pp. 59–65.

Barkhudarov, E. M. et al. (1991). 'Nonregular reflection of a ring shock from the axis of symmetry'. In: *Fluid Dynamics* 25.5, pp. 810–812. ISSN: 0015-4628. DOI: 10.1007/BF01049559.

Betchov, R. (2006). 'On the curvature and torsion of an isolated vortex filament'. In: *Journal of Fluid Mechanics* 22.03, p. 471. ISSN: 0022-1120. DOI: 10.1017/S0022112065000915.

Brouillette, M. and C. Hébert (1997). 'Propagation and interaction of shock-generated vortices'. In: *Fluid Dynamics Research* 21.3, pp. 159–169. ISSN: 0169-5983. DOI: 10.1016/S0169-5983(97)00010-5.

Brown, D. and M. Minion (1995). 'Performance of under-resolved two-dimensional incompressible flow simulations'. In: *Journal of Computational Physics* 122.1, pp. 165–183.

Cooppan, S. and B. W. Skews (2015). 'Vortex Shedding over a Discontinuous Edge'. In: *29th International Symposium on Shock Waves 2*. Madison, WI, USA: Springer International Publishing, pp. 1573–1578. DOI: 10.1007/978-3-319-16838-8_126.

Courant, R. and K. O. Friedrichs (1948). *Supersonic flow and shock waves*. Ed. by H. Bohr. 1st ed. New York, New York, USA: Interscience Publishers Inc., p. 416.

Didden, N. (1979). 'On the formation of vortex rings: Rolling-up and production of circulation'. In: *Zeitschrift für angewandte Mathematik und Physik ZAMP* 30.1, pp. 101–116. ISSN: 0044-2275. DOI: 10.1007/BF01597484.

Elder, F. K. and N. De Haas (1952). 'Experimental Study of the Formation of a Vortex Ring at the Open End of a Cylindrical Shock Tube'. In: *Journal of Applied Physics* 23.10, p. 1065. ISSN: 00218979. DOI: 10.1063/1.1701987.

Eliasson, V., N. Apazidis and N. Tillmark (2007). 'Controlling the form of strong converging shocks by means of disturbances'. In: *Shock Waves* 17.1-2, pp. 29–42. ISSN: 09381287. DOI: 10.1007/s00193-007-0087-9.

Green, S. I. (1995). *Fluid vortices (Google eBook)*. Springer, p. 878. ISBN: 0792333764.

Guderley, G. (1942). 'Starke kugelige und zylindrische Verdichtungsstöße in der Nähe des Kugelmittelpunktes bzw. der Zylinderachse'. In: *Luftfahrtforschung* 19, pp. 302–312.

Hama, F. R. (1962). 'Progressive Deformation of a Curved Vortex Filament by its Own Induction'. In: *Physics of Fluids* 5.10, p. 1156. ISSN: 00319171. DOI: 10.1063/1.1706500.

Hama, F. R. (1963). 'Progressive Deformation of a Perturbed Line Vortex Filament'. In: *Physics of Fluids* 6.4, p. 526. ISSN: 00319171. DOI: 10.1063/1.1706768.

Helmholtz, H. L. F. von (1867). 'On Integrals of the hydrodynamical equations, which express vortex-motion'. In: *Philosophical Magazine* 34, pp. 15–24. DOI: 10.1080/14786446708639824.

Helmholtz, H. L. F. von (1868). 'On the discontinuous movements of fluids'. In: *Monthly Reports of the Royal Prussian Academy of Philosophy in Berlin* 23.

Hicks, W. (1894). 'On the steady motion and small vibrations of a hollow vortex'. In: *Philophical Transactions of the Royal Society of London A* 175, pp. 161–195.

Hill, M. (1894). 'On a Spherical Vortex.' In: *Proceedings of the Royal Society of London* 55.331-335, pp. 219–224.

Hornung, H. (2000). 'Oblique shock reflection from an axis of symmetry'. In: *Journal of Fluid Mechanics* 409, pp. 1–12. ISSN: 00221120. DOI: 10.1017/S0022112099007831.

Hornung, H. and D. Schwendeman (2001). 'Oblique shock reflection from an axis of symmetry: shock dynamics and relation to the Guderley singularity'. In: *Journal of Fluid Mechanics* 438, pp. 1–12. ISSN: 0022-1120. DOI: 10.1017/S0022112001004360.

Jeong, J. and F. Hussain (1995). 'On the identification of a vortex'. In: *Journal of Fluid Mechanics* 285.-1, p. 69. ISSN: 0022-1120. DOI: 10.1017/S0022112095000462.

Jiang, Z., O. Onodera and K. Takayama (1999). 'Evolution of shock waves and the primary vortex loop discharged from a square cross-sectional tube'. In: *Shock Waves* 9.1, pp. 1–10. ISSN: 0938-1287. DOI: 10.1007/s001930050133.

Jiang, Z., K. Takayama et al. (1997). 'Transient shock wave flows in tubes with a sudden change in cross section'. In: *Shock Waves* 7.3, pp. 151–162. ISSN: 0938-1287. DOI: 10.1007/s001930050072.

Jiang, Z., C. Wang et al. (2003). 'Three-dimensional propagation of the transmitted shock wave in a square cross-sectional chamber'. In: *Shock Waves* 13.2, pp. 103–111. ISSN: 0938-1287. DOI: 10.1007/s00193-003-0197-y.

Kambe, T. and T. Takao (1971). 'Motion of Distorted Vortex Rings'. In: *Journal of the Physical Society of Japan* 31.2, pp. 591–599. ISSN: 0031-9015. DOI: 10.1143/JPSJ.31.591.

Kim, H.-D., Y.-H. Kweon and T. Setoguchi (2003). 'A study of the impulsive wave discharged from the inclined exit of a tube'. In: *Proceedings of the Institution of Mechanical Engineers, Part C: Journal of Mechanical Engineering Science* 217.2, pp. 271–279. ISSN: 0954-4062. DOI: 10.1243/095440603762826585.

Kjellander, M., N. Tillmark and N. Apazidis (2011). 'Experimental determination of self-similarity constant for converging cylindrical shocks'. In: *Physics of Fluids* 23.11. ISSN: 10706631. DOI: 10.1063/1.3662002.

Kleine, H. et al. (2009). 'Time-resolved visualization of shock-vortex systems emitted from an open shock tube'. In: *Journal of Visualization* 13.1, pp. 33–40. ISSN: 1343-8875. DOI: 10.1007/s12650-009-0009-2.

Kollmann, W. (2011a). 'Accurate numerical simulations of vortex flows. I: Vortex breakdown'. In: *Computers & Fluids* 41.1, pp. 103–109. ISSN: 00457930. DOI: 10.1016/j.compfluid.2010.09.018.

Kollmann, W. (2011b). 'Accurate numerical simulations of vortex flows II: Interaction of swirling vortex rings'. In: *Computers & Fluids* 41.1, pp. 110–118. ISSN: 00457930. DOI: 10.1016/j.compfluid.2010.09.019.

Krueger, P. (2008). 'Circulation and trajectories of vortex rings formed from tube and orifice openings'. In: *Physica D: Nonlinear Phenomena* 237.14-17, pp. 2218–2222. ISSN: 01672789. DOI: 10.1016/j.physd.2008.01.004.

Lim, T. T. (1997). 'On the role of Kelvin-Helmholtz-like instability in the formation of turbulent vortex rings'. In: *Fluid Dynamics Research* 21.1, pp. 47–56. ISSN: 0169-5983. DOI: 10.1016/S0169-5983(96)00059-7.

Mölder, S. et al. (1997). 'An experimental investigation of the stability of converging cylindrical shock waves in air'. In: *Proceedings of the 21st International Symposium on Shock Waves*. Ed. by A. Houwing. Great Keppel Island, Australia, pp. 875–880.

Moore, D. (1985). 'The effect of compressibility on the speed of propagation of a vortex ring'. In: *Proceedings of the Royal Society of London. A. Mathematical and Physical Sciences* 397.1812, pp. 87–97.

Murugan, T. and D. Das (2010). 'Characteristics of counter-rotating vortex rings formed ahead of a compressible vortex ring'. In: *Experiments in Fluids* 49.6, pp. 1247–1261. ISSN: 0723-4864. DOI: 10.1007/s00348-010-0868-2.

Murugan, T., S. De et al. (2011). 'Numerical simulation and PIV study of compressible vortex ring evolution'. In: *Shock Waves* 22.1, pp. 69–83. ISSN: 0938-1287. DOI: 10.1007/s00193-011-0344-9.

Oshima, Y. (1988). 'Bifurcation of an elliptic vortex ring'. In: *Fluid Dynamics Research* 3, pp. 133–139.

Papamoschou, D. and A. Roshko (1988). 'The compressible turbulent shear layer: an experimental study'. In: *Journal of Fluid Mechanics* 197.1973, p. 453. ISSN: 0022-1120. DOI: 10.1017/S0022112088003325.

Perry, R. W. and A. Kantrowitz (1951). 'The production and stability of converging shock waves'. In: *Journal of Applied Physics* 22.7, pp. 878–886. ISSN: 00218979. DOI: 10.1063/1.1700067.

Phan, K. and J. Stollery (1984). 'The effect of suppressors and muzzle brakes on shock wave strength'. In: *Shock Tubes and Waves*. Vol. 1, pp. 519–526.

Rankine, W. (1872). *A manual of applied mechanics*. Charles Griffin and Co.

Reynolds, O. (1883). 'Vortex Rings'. In: *Nature* 29, pp. 193–195. DOI: 10.1038/029193a0.

Rubidge, S. and B. W. Skews (2014). 'Shear-layer instability in the Mach reflection of shock waves'. In: *Shock Waves* 24.5, pp. 479–488. ISSN: 09381287. DOI: 10.1007/s00193-014-0515-6.

Rubidge, S., B. W. Skews et al. (2015). 'Kelvin-Helmholtz instability on the Mach reflection shear layer'. In: *29th International Symposium on Shock Waves*. Ed. by R. Bonazza and D. Ranjan. Madison, WI, USA, pp. 1579–1584. ISBN: 978-3-319-16834-0.

Settles, G. (2001). *Schlieren and Shadowgraph Techniques*. Springer-Verlag, p. 376. ISBN: 9783540661559. DOI: 10.1007/978-3-642-56640-0.

Skews, B. W. (1967a). 'The perturbed region behind a diffracting shock wave'. In: *Journal of Fluid Mechanics* 29.04, pp. 705–719. ISSN: 0022-1120. DOI: 10.1017/S0022112067001132.

Skews, B. W. (1967b). 'The shape of a diffracting shock wave'. In: *Journal of Fluid Mechanics* 29.02, p. 297. ISSN: 0022-1120. DOI: 10.1017/S0022112067000825.

Skews, B. W., N. Menon et al. (2002). 'An experiment on imploding conical shock waves'. In: *Shock Waves* 11.4, pp. 323–326. ISSN: 09381287. DOI: 10.1007/s001930100115.

Skews, B. W. and J. O. Reeves (2012). 'Unsteady three-dimensional compressible vortex flows generated during shock wave diffraction'. In: *Shock Waves*, pp. 161–172. ISSN: 0938-1287. DOI: 10.1007/s00193-012-0353-3.

Sun, M. and K. Takayama (2003). 'A note on numerical simulation of vortical structures in shock diffraction'. In: *Shock Waves* 13.1, pp. 25–32. ISSN: 0938-1287. DOI: 10.1007/s00193-003-0195-0.

Takayama, K., H. Kleine and H. Grönig (1987). 'An experimental investigation of the stability of converging cylindrical shock waves in air'. In: *Experiments in Fluids* 5.5, pp. 315–322. ISSN: 07234864. DOI: 10.1007/BF00277710.

Thomson, W. (1871). 'XLVI. Hydrokinetic solutions and observations'. In: *The London, Edinburgh, and Dublin Philosophical Magazine and Journal of Science* 42.281, pp. 362–377.

Viets, H. (1972). 'Dynamics of Bilaterally Symmetric Vortex Rings'. In: *Physics of Fluids* 15.2, p. 230. ISSN: 00319171. DOI: 10.1063/1.1693899.

Wedemeyer, E. (1961). 'Ausbildung eines Wirbelpaares an den Kanten einer Platte'. In: *Ingenieur-Archiv* 30.3, pp. 187–200. ISSN: 0020-1154. DOI: 10.1007/BF00534755.

Whitham, G. (1959). 'A new approach to problems of shock dynamics Part 2. Three-dimensional problems'. In: *Journal of Fluid Mechanics* 5.03, p. 369. ISSN: 0022-1120. DOI: 10.1017/S002211205900026X.

Widnall, S. E. and J. P. Sullivan (1973). 'On the stability of vortex rings'. In: *Proceedings of the Royal Society of London* 332.1590, pp. 335–353.

Zare-Behtash, H., N. Gongora-Orozco and K. Kontis (2009). 'Global visualization and quantification of compressible vortex loops'. In: *Journal of Visualization* 12.3, pp. 233–240. ISSN: 1343-8875. DOI: 10.1007/BF03181861.

Zare-Behtash, H., K. Kontis and N. Gongora-Orozco (2008). 'Experimental investigations of compressible vortex loops'. In: *Physics of Fluids* 20.12, p. 126105. ISSN: 10706631. DOI: 10.1063/1.3054151.

Zare-Behtash, H. et al. (2009). 'Compressible vortex loops: Effect of nozzle geometry'. In: *International Journal of Heat and Fluid Flow* 30.3, pp. 561–576. ISSN: 0142727X. DOI: 10.1016/j.ijheatfluidflow.2009.02.022.

Zare-Behtash, H. et al. (2010). 'Shock wave-induced vortex loops emanating from nozzles with singular corners'. In: *Experiments in Fluids* 49.5, pp. 1005–1019. ISSN: 0723-4864. DOI: 10.1007/s00348-010-0839-7.

Glossary

axisymmetric Geometry produced by revolution of a profile around an axis.

baroclinicity The degree to which the vectors of pressure and density gradient are inclined to one another.

enstrophy The quantity directly related to the kinetic energy in a flow model that corresponds to dissipation effects in the fluid.

enthalpy The thermodynamic potential of a system comprised of internal energy and the pressure potential energy.

Appendix A Specification of equipment and instrumentation used in schlieren visualisation system

Table A.1: Specification of apparatus and instrumentation for shock diffraction from the oblique exit of a shock tube

Component	**Manufacturer**	**Model**	**Other specifications**
Ball bearing stage with metric XY centre drive	OptoSigma	123-0235	
Collar	OptoSigma	148-1000	
Cylindrical lens holder	OptoSigma	11-1165	
Digital oscilloscope	Yokogawa instruments	DL708E	Serial number: 12W713778G
High-speed camera	Photron	Fastcam SA5-775K	Serial number: 362429074
Light source	Canon	EOS Speedlite 430EX-II	Pulse duration $\approx$ 1 ms; rise time $\approx$ 120 μs
Magnetic base	OptoSigma	147-0340	
Optical carrier	OptoSigma	146-1335	
Optical rails	OptoSigma	146-0440	
Paraboloid mirror	Meade Instruments	16”	f/4.5 (focal length 72.3” / 72.5”)

Table A.1: Specification of apparatus and instrumentation for shock diffraction from the oblique exit of a shock tube (cont.)

Component	**Manufacturer**	**Model**	**Other specifications**
Plano-concave cylindrical lens	OptoSigma	022-1445-A55	30 mm x 30 mm; f = -300 mm; material: BK7
Plano-convex lens	Edmund optics	47738	80 mm focal length; VIS 0°coated; achromatic; material: BK7
Post	OptoSigma	148-0265	
Post holder	OptoSigma	148-1355	
Pressure transducer	PCB Piezotronics	M113A21	Serial number: 6398
Pressure transducer	PCB Piezotronics	M113A23	Serial number: 4816
Pressure transducer signal conditioner	PCB Piezotronics	482A04	4-channel
Pressure transducer signal conditioner	PCB Piezotronics	F482A	Single channel
Spherical lens holder	OptoSigma	111-1135	
Trigger signal delay box	ElectroDI		Minimum delay: 50 μs; maximum delay: 99 998 μs; resolution: 2 μs

Table A.2: Specification of apparatus and instrumentation for conical shock wave reflection

Component	**Manufacturer**	**Model**	**Other specifications**
Ball bearing stage with metric XY centre drive	OptoSigma	123-0235	
Collar	OptoSigma	148-1000	
Cylindrical lens holder	OptoSigma	11-1165	
Digital oscilloscope	Yokogawa instruments	DL708E	Serial number: 12W713778G
High-speed camera	Photron	Fastcam SA5-775K	Serial number: 362429074
Light source	Canon	EOS Speedlite 430EX-II	Pulse duration $\approx$ 1 ms; rise time $\approx$ 120 μs
Magnetic base	OptoSigma	147-0340	
Optical carrier	OptoSigma	146-1335	
Optical rails	OptoSigma	146-0440	
Paraboloid mirror	Meade Instruments	12.5”	f/6 (focal length: 75”)
Plano-concave cylindrical lens	OptoSigma	022-1445-A55	30 mm x 30 mm; f = -300 mm; material: BK7
Plano-convex lens	Edmund optics	47738	80 mm focal length; VIS 0°coated; achromatic; material: BK7
Post	OptoSigma	148-0265	
Post holder	OptoSigma	148-1355	
Pressure transducer	PCB Piezotronics	M113A21	Serial number: 6391
Pressure transducer	PCB Piezotronics	M113A21	Serial number: 6393
Pressure transducer	PCB Piezotronics	M113A21	Serial number: 7343
Pressure transducer	PCB Piezotronics	M113A21	Serial number: 7345

Table A.2: Specification of apparatus and instrumentation for conical shock wave reflection (cont.)

Component	**Manufacturer**	**Model**	**Other specifications**
Pressure transducer	PCB Piezotronics	M113A21	Serial number: 7937
Pressure transducer	PCB Piezotronics	M113B21	Serial number: 19619
Pressure transducer signal conditioner	PCB Piezotronics	482A04	4-channel
Pressure transducer signal conditioner	PCB Piezotronics	F482A	Single channel
Spherical lens holder	OptoSigma	111-1135	
Trigger signal delay box	ElectroDI		Minimum delay: 50 μs; maximum delay: 99 998 μs; resolution: 2 μs

Appendix B Videos

A number of videos, both experimental and computational, have been generated to improve understanding of the flow field. Since these are too large to embed directly within the PDF version of this document, a digital appendix has been created. This is available within the archives of the University of the Witwatersrand, Johannesburg and at this shared Google Drive (no sign-in required). A categorisation of and hyperlink to each of the videos and their containing folders provided for each of the flow fields presented is given in the relevant tables below.

(Please note that for readers not using the electronic version of this thesis that the shortened URL for the shared drive is https://goo.gl/69cY6X. The names of the files in the relevant folders give a description of the test conditions and the frame rate at which the videos are rendered.)

B.1 Flow Produced by a Conical Shock Wave

Table B.1: Videos of Conical Shock Wave Diffraction Experiments

Type	Configuration		
Axisymmetric	2.2 Bar		
	4.1 Bar		
	6.2 Bar		
Jet Anomaly	Lower Occlusion	2.2 Bar	10 Degree
			20 Degree
			30 Degree
		4.1 Bar	10 Degree
			20 Degree
			30 Degree
		6.2 Bar	10 Degree
			20 Degree
			30 Degree
	Upper Occlusion	2.2 Bar	30 Degree
			45 Degree
			60 Degree
		4.1 Bar	30 Degree
			45 Degree
			60 Degree
		6.2 Bar	30 Degree
			45 Degree
			60 Degree

B.2 Flow Produced by Diffraction of a Plane Shock Wave at the Inclined Exit of a Shock Tube

Table B.2: Videos of Inclined Shock Tube Exit Shock Wave Diffraction Experiments for Exit Plane Angles of 30°, 45°, and 60°

Exit Plane Angle	Experimental
30 Degrees	Mach 1.26
	Mach 1.47
	Mach 1.66
45 Degrees	Mach 1.28
	Mach 1.49
	Mach 1.66
60 Degrees	Mach 1.28
	Mach 1.49
	Mach 1.67

Table B.3: Videos of Inclined Shock Tube Exit Shock Wave Diffraction Experiments and CFD for 45° Exit Plane Angle

CFD	Video File	Experimental	Video File
Mach 1.25	Pressure Elevation	Upstream	Mach 1.27
	Pressure Plot		
	Vortex Loop	Upstream	Mach 1.27
	Vortex Loop Elevation		
Mach 1.4	Pressure Elevation	Upstream	Mach 1.48
	Pressure Plot		
	Vortex Loop	Upstream	Mach 1.48
	Vortex Loop Elevation		
Mach 1.6	Pressure Elevation	Upstream	Mach 1.67
	Pressure Plot		
	Vortex Loop	Upstream	Mach 1.67
	Vortex Loop Elevation		
Mach 2.2	Pressure Elevation		
	Pressure Plot		
	Vortex Loop		
	Vortex Loop Elevation		

B.3 Flow Produced by Diffraction of a Plane Shock Wave at the Curved Exit of a Shock Tube

Table B.4: Videos of Curved Shock Tube Exit Shock Wave Diffraction Experiments for Radius Ratios of 3 and 5

Exit Radius Ratio	Experimental
3	Mach 1.25
	Mach 1.49
	Mach 1.67
5	Mach 1.26
	Mach 1.42
	Mach 1.66

Table B.5: Videos of Curved Shock Tube Exit Shock Wave Diffraction Experiments and CFD for a Radius Ratio of 3 with a Tangent Exit Plane

CFD	Video File	Experimental Video File
Mach 1.25	Pressure Elevation	Mach 1.21
	Pressure Plot	
	Vortex Loop	
	Vortex Loop Elevation	
Mach 1.4	Pressure Elevation	Mach 1.49
	Pressure Plot	
	Vortex Loop	
	Vortex Loop Elevation	
Mach 1.6	Pressure Elevation	Mach 1.67
	Pressure Plot	
	Vortex Loop	
	Vortex Loop Elevation	
Mach 2.2	Pressure Elevation	
	Pressure Plot	
	Vortex Loop	
	Vortex Loop Elevation	